Scanning Tunneling Spectroscopy of Topological Insulators and Cuprate Superconductors

Scanning Tunneling Spectroscopy of Topological Insulators and Cuprate Superconductors

A DISSERTATION PRESENTED

BY

MICHAEL MANCHUN YEE

TO

THE DEPARTMENT OF PHYSICS

IN PARTIAL FULFILLMENT OF THE REQUIREMENTS

FOR THE DEGREE OF

DOCTOR OF PHILOSOPHY

IN THE SUBJECT OF

PHYSICS

HARVARD UNIVERSITY

CAMBRIDGE, MASSACHUSETTS

MAY 2014

Thesis advisor: Professor Jennifer E. Hoffman Michael Manchun Yee

Scanning Tunneling Spectroscopy of Topological Insulators and Cuprate Superconductors

Abstract

Over the past twenty-five years, condensed matter physics has been developing materials with novel electronic characteristics for a wide range of future applications. Two research directions have shown particular promise: topological insulators, and high temperature copper based superconductors (cuprates). Topological insulators are a newly discovered class of materials that can be manipulated for spintronic or quantum computing devices. However there is a poor spectroscopic understanding of the current topological insulators and emerging topological insulator candidates. In cuprate superconductors, the challenge lies in raising the superconducting transition temperature to temperatures accessible in non-laboratory settings. This effort has been hampered by a poor understanding of the superconducting mechanism and its relationship with a mysterious pseudogap phase. In this thesis, I will describe experiments conducted on topological insulators and cuprate superconductors using scanning tunneling microscopy and spectroscopy, which provide nanoscale spectroscopic information in these materials.

First, I will describe experiments on the purported topological Kondo insulator SmB_6, where a topological surface state is expected to emerge from a strongly correlated hybridization gap. I used a spectral decomposition technique and temperature dependent spectroscopy to measure and observe the opening of the hybridization gap, and find evidence for a topological surface state. I will then describe experiments performed on the topological insulator $Bi_{2-x}Fe_xSe_3$, where I observed the scattering of surface states to surprisingly high energies. Models using density functional theory show that the interaction of the trivial and topological surface states could provide a route towards future topological insulator devices.

Thesis advisor: Professor Jennifer E. Hoffman Michael Manchun Yee

I then discuss two experiments performed on the Bi-based cuprates. In the first experiment, I imaged a static charge density wave that, in conjunction with bulk-sensitive probes, reconciles observations of surface and bulk charge ordering in the cuprates over the past twenty years. In the second experiment, I validated previous observations of an electronic nematic order in the pseudogap phase using high spatial-resolution spectroscopy. Together, the work on the cuprates provides insight into the nature of the pseudogap phase, which we find to be characterized by broken symmetries and charge ordering.

Contents

Listing of figures

Acknowledgments

This page is probably the most important part of this thesis, because nothing here would have been possible without the many people who have helped me along the way.

Firstly, I would like to thank my advisor Jenny who has unfailingly supported me throughout the ups and downs in my personal and professional life during graduate school. I have learned immensely from collaborating with her and her insistence on distilling and communicating physics in a way that is both rigorous and clear. Next, I would like to thank the members of STM1, Anjan and Yang who helped perform every experiment in this thesis. To Anjan the biggest thank you for being my partner-in-crime on STM1 for the long nights and endless weekends during the first four years of my Ph.D. Thank you for teaching me most of what I know about physics, and low temperature experiments, and for fixing the STM in my second year. To Yang, thanks for being the best and most understanding teammate I could have had during the last two years. I have gained immensely from his knowledge of physics, his creativity in analyzing and understanding data and his constant focus on finding new physics from our experiments. To the newest member of STM1, Jason, I would like to thank him for forgiving my poor understanding of ARPES and TIs, and helping me interpret the work on Bi_2Se_3. It really would not have been possible to finish this work had it not been for the friendly faces in the lab early in the morning and late at night. So thank you to Jeehoon, Liz, Adam, Tess, Lena, Dennis, Can-Li, and Maoz.

I would also like to thank Profs. Yacoby, Sachdev, Golovchenko and Kaxiras for serving on my committees, and Profs. Amit Kanigel, Zachary Fisk, Yoichi Ando, H. Eisaki and H. Ikuta for the samples prepared in their laboratories.

The last five years in Cambridge would have been less enjoyable and probably not possible had it not been for the friends who became my family in Cambridge. To Ilija and Courtney, who

welcomed me into their lives and supported me throughout the last years - the biggest thank you. I will always remember the Shamu by the pool, the turtles and the mojitos. Thank you to my roommate Gairik, who has been a constant presence and source of support throughout my time here. And finally to my many other friends in Cambridge, you are too numerous to thank, but you helped me immensely along the way.

To my family I owe the most. Thank you to my mother and father, Christina and Jim, who sacrificed so much to raise my brother and me to be who we are today. To my brother Stephen, who has been a constant source of fun and encouragement. And finally to my beloved wife, Joanne, who has been with me and supported me every step of the way. Thank you for putting up with the border and plane ride that separated us, the endless Skype calls, and a long-distance marriage. Without you most of all, none of this would have happened. I can't wait to reduce the distance between us by a few orders of magnitude.

To my mother Christina, and my father Jim, for raising the luckiest son in the world.

1

Introduction

Over the past five years, the field of condensed matter physics has actively studied two families of materials: (1) a new class of materials known as topological insulators, (2) the intriguing and poorly understood copper-based high temperature superconductors. This chapter gives a broad overview of these two families of materials, discusses their unusual characteristics, and potential applications. The final section of this chapter outlines the structure of the remaining chapters in this thesis.

1.1 A New Class of Materials: Topological Insulators

Over the past decade, condensed matter physics has been revolutionized by the understanding that interactions between the electron's spin and orbital motion, "spin-orbit coupling", can lead to new and exciting electronic phases. In particular, since 2009, a new class of "topological materials" has been discovered in compounds with a strong spin-orbit coupling (SOC), and a small bandgap, such as Bi_2Se_3, Bi_2Te_3, and $Bi_{1-x}Sb_x$ [1–4]. The electronic states at the surface of these materials exhibit unique properties, similar to those of graphene, that can be exploited for future applications in spintronics, quantum computation, or in the search for exotic physics [2–5]. These materials, called "topological insulators", were predicted using a newly emergent understanding of electronic topological classes in condensed matter systems. In this section, we briefly describe the concept of topology as applied to condensed matter systems, and discuss the exciting experimental physics that arises from these materials.

1.1.1 Topological Electronic Phases

Topological insulators are materials in which the bulk has an insulating gap in the density of states, while the surface contains unique surface states that have topological properties. The presence of these exotic electronic states at the interface of the topological insulator with the vacuum is characteristic of the topological nature of the material.

How does topology, which is a branch of mathematics concerned with the properties of objects and space under continuous deformations, predict the existence of exotic electronic phases? As an example, topology can classify 2D surfaces dependent on the number of holes in the surface, or the genus g, as shown in Fig. 1.1. Objects within the same genus are equivalent because in principle, they can be stretched and deformed into one another, without poking a hole through them. In this way, a donut is classified as $g = 1$ and is equivalent to a coffee mug with a handle. Meanwhile an iPhone, which can be continuously deformed into an orange, has no holes, and both are classified as $g = 0$. Objects within one genus cannot be continuously deformed without puncturing or closing the hole, and so these two families represent distinct and mutually exclu-

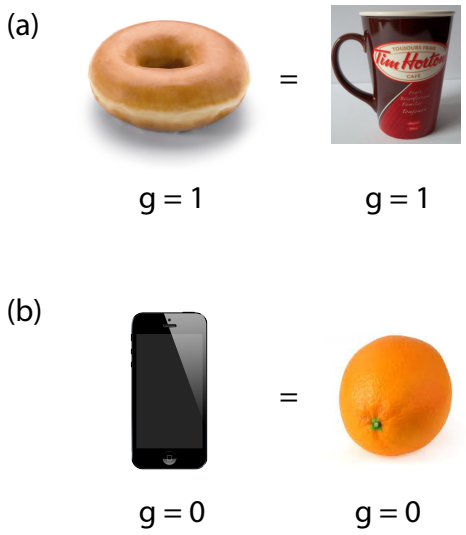

Figure 1.1: Examples of a Topological classification. Objects can be classified by its number of holes g. All objects that can be continuously deformed to one another, while preserving g are within the same topological class. Here we have an example of **(a)** a donut with $g = 1$ being in the same class as a coffee mug with a handle, and **(b)** an iPhone with $g = 0$ being in the same class as an orange.

sive families of shapes and objects.

Topological insulators differ from generic or "trivial" insulators through a similar topological classification, which instead of measuring the number of holes in an object, measures a property called the Berry's phase in the electronic structure of the material [2, 3]. The genus g of Fig. 1.1 is equivalent to the topological invariant of the system, which remains constant so long as the material contains a spectral gap Δ in its band structure or density of states. Because the vacuum is considered a "topologically trivial insulator", the boundary between a topologically "non-trivial" and a topologically trivial insulator will have unique properties, and for our purposes, the novel electronic states of interest.

One of the fundamental consequences of the topological classification of materials, is that at the boundary where the topological classification changes, there will exist gapless conducting states at the edge [2]. Because the topological invariant must change at the interface, the spectral gap $\Delta \rightarrow 0$, leading to the existence of gapless, metallic edge states. The simplest example of edge states existing at the interface of topologically trivial and non-trivial materials is at the interface of an integer quantum hall system and the vacuum, shown schematically in Fig.

1.2. In the bulk of the quantum hall system, electrons that are confined in two dimensions under a perpendicular magnetic field B will undergo cyclotron orbits with a cyclotron frequency, $\omega_c = eB(mc)^{-1}$, where e is the electron charge, m is the electron mass, and c is the speed of light. The quantum hall system can be considered an insulator with a bandgap $\Delta = \hbar\omega_c$, which separates the highest occupied electron level, called a Landau level, from the lowest unoccupied Landau level. However, the interface between the vacuum, which is equivalent to topologically trivial insulators, and the quantum hall system will possess topological surface states. To see this, we simply examine the electron motion at the edge. At the edge of the system, the electrons cannot complete their cyclotron orbits, and the result is a skipping motion that leads to unidirectional flow of electrons at the edge of the 2D quantum hall system [2, 6]. The edge states are chiral, in the sense that their direction of propagation is only in one direction, and therefore the edge states are insensitive to disorder. This observation in the quantum hall system is more general, and leads to the conclusion that gapless, chiral edge states will exist at any interface between two topological phases.

1.1.2 Three Dimensional Topological Insulators

Following theoretical work by a number of research groups [1, 7–10], a topological Z_2 invariant was developed to classify topological materials in the presence of strong spin-orbit coupling and time reversal symmetry (TRS). Like the 2-dimensional integer quantum hall state, the boundary between trivial Z_2 and nontrivial Z_2 classes must have gapless surface states. Because of the combination of time reversal symmetry (TRS), and spin-orbit coupling, the topological surface states (TSS) that exist at the boundary of trivial and non-trivial topological classes have exotic properties [2, 3]. First, the change in topological classes guarantees the existence of these gapless surface states, making the surface states robust to non-magnetic impurities, and impurity induced localization effects. At the high symmetry points, because of the TRS, the spin up and down states are degenerate, but away from the high symmetry points, the degeneracy is split from spin-orbit interactions. This implies that at the time reversal invariant points, the disper-

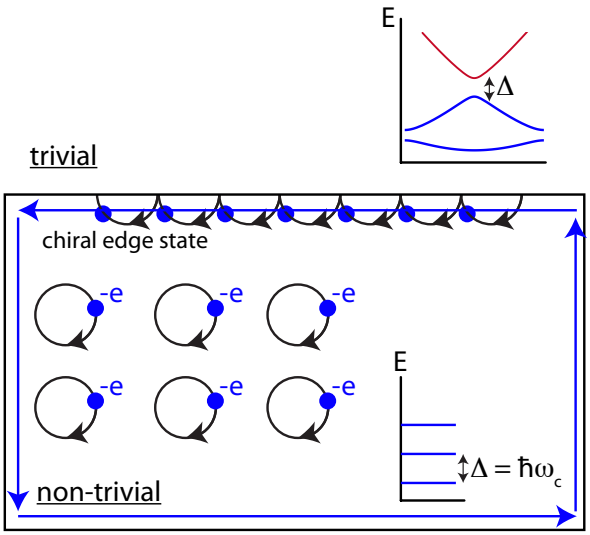

Figure 1.2: Interface of a Quantum Hall System with a Trivial Insulator. In an applied magnetic field, the electrons in a 2D electron gas undergo cyclotron orbits with a frequency $\omega_c = eB(mc)^{-1}$, where m is the mass of the electron, e is the charge of the electron, and B is the magnitude of the magnetic field. The energy states of this system are separated by $\Delta = \hbar\omega_c$, and can be thought of as a band gap, similar to the band gap of a trivial insulator, brought on by band theory. At the interface of the trivial and non-trivial phases, an edge state exists, which, because of the skipping cyclotron orbits, has a single direction that traverses the edge of the quantum hall system.

sion of the states has the form of massless Dirac fermions,

$$E(k) = v_D k + E_{\mathrm{DP}} \tag{1.1}$$

where, k is relative to the high symmetry point, v_D is the velocity at the Dirac point, and E_{DP} is the energy of the degeneracy. Furthermore, the Dirac dispersion around the high symmetry k-point is guaranteed by TRS. TRS also requires that $\vec{k}$ and $-\vec{k}$ must have opposite spin states, resulting in a chirality that locks the $\vec{k}$ states to specific spin states. The dispersion and the existence of the surface states in the gap is shown schematically in Fig. 1.3a,b [11], where we can see that TSS span the bulk band gap Δ. Finally, in the presence of non-magnetic disorder, topological surface states impinging on disorder are forbidden to back-scatter because the $\vec{k} \rightarrow -\vec{k}$ scattering process requires a forbidden spin-flip. This implies that the topological surface states are also robust to non-magnetic disorder because of the locking of spin and momentum. This was

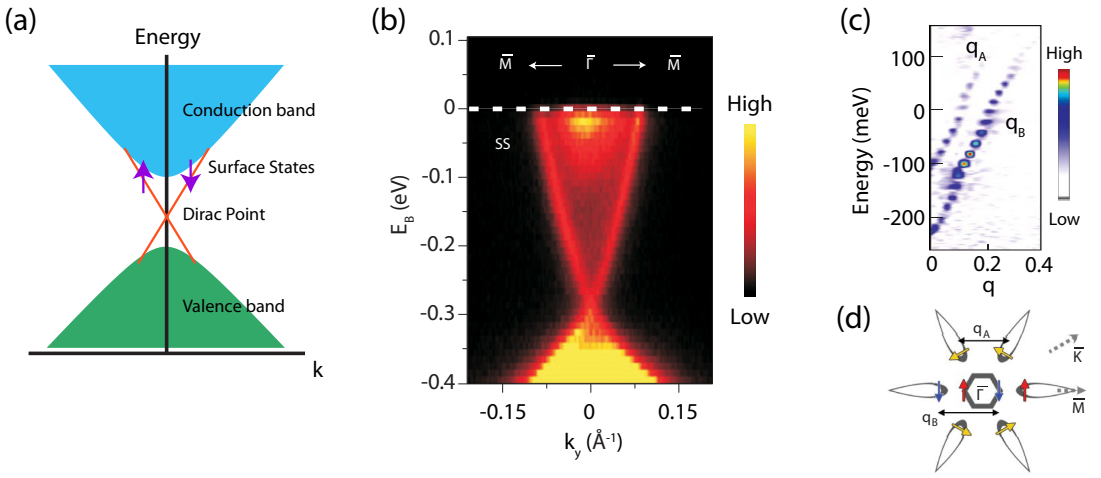

Figure 1.3: Three Dimensional Topological Insulators. (a) Cartoon of the surface states in a three dimensional topological insulator, shown in orange. At the high symmetry point $k = 0$, the surface states are degenerate. Away from $k = 0$, SOC splits the degeneracy of the spin states. **(b)** Angle resolved photoemission spectroscopy of the topological surface states (TSS) in Bi_2Se_3. Figure adapted from Ref. [11]. The Dirac dispersion of the TSS is confirmed in the data. **(c)** Scattering modes from a step edge in topoogical Sb (111). The two scattering modes q_A and q_B correspond to the scattering processes schematically shown in (d). Notice the absence of blue to red scattering, which would require a spin-flip and is forbidden. (c) and (d) were adapted from Ref. [12].

experimentally shown using a scanning tunneling microscope in Fig. 1.3c,d [12].

The introduction of topological classes into the field of condensed matter physics has lead to a surge in research that has yielded exciting new physics. The unique properties of TIs has applications towards a variety of interesting novel devices. The interface of a ferromagnet and a TI could yield a novel spintronic device [13]. Meanwhile, the vortex state at the interface of a topological insulator and a superconductor could yield an exotic particle known as a Majorana particle [14], which has the unique property that it is its own antiparticle [15]. Majorana fermions could be used to devise a novel quantum computer that is well-protected from errors and utilizes non-Abelian statistics [16]. Despite these exciting possibilities, a tremendous amount of unanswered questions remain, including whether there are other types of topological phases in new materials, and whether current materials can be engineered for better device applications. The new understanding brought about by topology has only scratched the surface and many new forms of topological insulators will be discovered, each with different advantages and disadvantages compared to the previous generation.

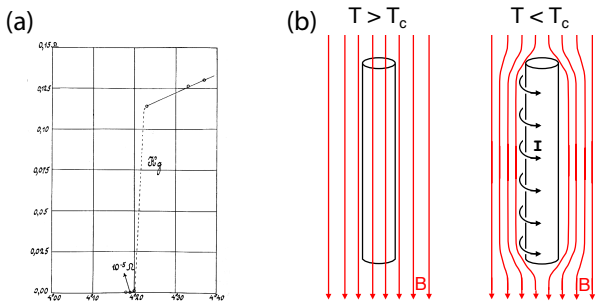

Figure 1.4: Properties of superconductors. (a) At temperatures lower than T_c, the resisitivity vanishes, as shown for Hg from Ref. [18]. **(b)** At temperatures lower than T_c, the superconductor becomes perfectly diamagnetic, expelling all external magnetic fields. Figure adapted from Ref. [19].

1.2 High Temperature Superconductivity

Superconductivity, is a phase of matter that is characterized by zero resistivity, and perfect diamagnetism, as described in Fig. 1.4. At zero field, the material enters the superconducting phase from the normal phase at a transition temperature T_c, which for most superconductors discovered in the early 1900s was $\sim<$ 20 K. A theoretical description of the superconducting mechanism was finally proposed by Bardeen, Cooper and Schrieffer (BCS) in 1957 [17]. BCS theory described the superconducting state as comprised of pairs of electrons, called 'Cooper pairs', that were bound by a weak phonon-mediated attraction. The pairing of electrons opened a spectral gap in the density of states at the Fermi level from the pairing process, leading to a well known gap Δ that is associated with the superconducting state. By the 1980s, the theory of superconductivity was well established, and superconductivity was considered a cryogenic phenomenon, accessible only in laboratory conditions.

1.2.1 Copper-based High T_c Superconductors

The condensed matter community was surprised by the rapid discovery in 1986 of copper-based high temperature superconductors (cuprates). $LaBaCuO_4$ was the first compound discovered, with $T_c = 30$ K [20], which was quickly followed by $YBa_2Cu_3O_{7+x}$ (YBCO) with $T_c = 93$ K [21]. Because the transition temperature of YBCO was above liquid nitrogen temperature ($T_{LN_2} = 77$

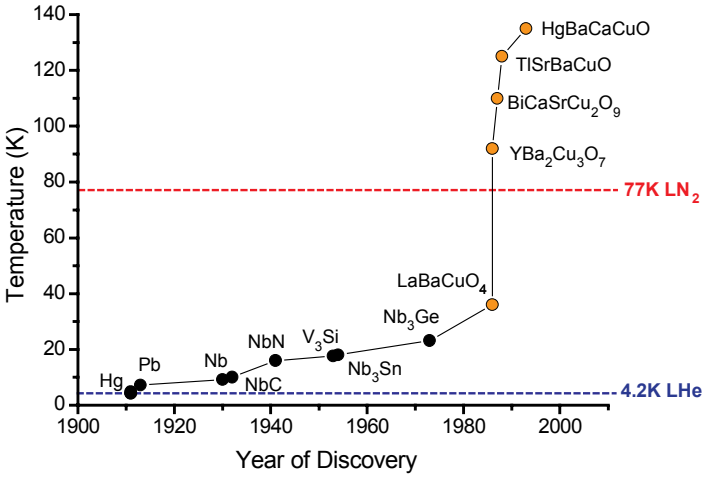

Figure 1.5: Timeline of the discovery of the Cuprate superconductors. Orange circles represent the T_c of the different families of the Cuprate superconductors. Red and blue dashed lines indicate the temperature of cryogenic liquid nitrogen and liquid helium. Figure adapted from Ref. [22].

K), this was the first superconductor that could be cooled using low cost liquid nitrogen, rather than higher cost liquid helium ($T_{\mathrm{LHe}} = 4.2$ K). The discovery of YBCO quickly led to hopes that new cost-effective technological applications in power transmission, electronics, and transportation could be achieved using superconductors with ever higher T_c. Additional discoveries of the Bi-based, Tl-based and Hg-based copper oxide superconductors would soon push the transition temperature up to ~ 140 K. The rapid discovery of different superconducting T_c is shown in Fig. 1.5. Despite the initial promise and hopes that T_c might be pushed above room temperature, allowing room temperature superconductivity, the process of engineering higher T_c superconductors has been hampered by a poor understanding of the superconducting mechanism in the cuprates.

There are multiple families of different Cuprate superconductors, which are typically classified based off of the first element in the chemical formula (i.e. La, Y, Bi, Hg and Tl based families). The Cuprates are layered materials of different XO_n planes, where X is another element in the compound. An illustration of the structure of a Bi-based cuprate is shown in Fig. 1.6. The two-dimensional CuO_2 planes are the key ingredient in the Cuprates, being responsible for the superconductivity. What is surprising about the Cuprates, is that the superconductivity only arises upon doping into the system. The undoped, "parent" compound, is actually an antiferromagnetic

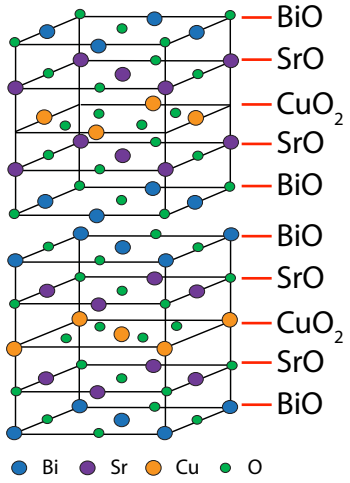

Figure 1.6: Representation of the crystal structure of Bi-2201. Because the top and bottom layers are BiO layers, the bonding between two BiO layers is the weakest, and defines the cleave plane of Bi-2201 crystal.

Mott insulator. The fact that an antiferromagnetic order could give rise to superconductivity is surprising, given that superconductivity is thought to be destroyed by magnetism.

1.2.2 Bi-2201 Structure

The cuprate compound that is studied in this thesis, is the Bi-based cuprate with a single CuO_2 layer, $Bi_{2-y}Sr_{2-x}La_xPb_yCuO_{6+\delta}$. This compound is typically known as "Bi-2201", in reference to the chemical subscripts of the parent compounds of the Bi-based superconductors, which typically have the form: $Bi_2Sr_2Ca_{n-1}Cu_nO_{2n+4+\delta}$. And so the $n = 2$ double CuO_2 layered compound $Bi_2Sr_2Ca_1Cu_2O_8$ is typically called Bi-2212, while the single layered $n = 1$ compound $Bi_2Sr_2Ca_0Cu_1O_6$ is called Bi-2201. The Bi-based cuprates are ideal for studies using scanning tunneling microscopy because of their relatively large crystal sizes, and easily cleaved structure. For reference, we display in Fig. 1.6 the Bi-2201 crystal structure, which is studied in Chapters 5 and 6.

1.2.3 Mysterious Pseudogap Phase

The doping dependence of the cuprates leads to a complicated three dimensional phase diagram that depends on the hole doping x, the temperature T, and the magnetic field H. At zero field, the phase diagram for the cuprates has the form shown in Fig. 1.7. At zero hole doping p, the cuprates are antiferromagnetic insulators, only upon doping does the superconductivity emerge. Optimal doping, is the doping level at which the superconducting T_c is maximum, which in Fig. 1.7, is $p_{\rm op} \sim 0.16$. Primarily on the underdoped ($p < p_{\rm op}$) side of the phase diagram, a mysterious phase called the pseudogap phase, exists in addition to the superconducting phase. The pseudogap phase is characterized by a gap in the density of states that exists at $T > T_c$, but below the pseudogap onset temperature of T^* [23], and can extend further into the superconducting phase and the overdoped part of the phase diagram. There is currently no consensus on whether or how the pseudogap phase interacts with the superconducting phase across the entire cuprate family, although it has been well characterized in Bi-2201 [24]. The nature and origin of this phase have been extensively studied for the past 20 years, and hopefully, a better understanding of the pseudogap phase will allow for a more clear understanding of the superconducting mechanism in the cuprates.

1.3 Dissertation Structure

The field of condensed matter physics is rich with novel electronic systems, such as topological insulators and cuprate superconductors, that are amenable to local spectroscopic studies. In contrast to bulk probes, scanning tunneling spectroscopy (STS) is well suited to understanding electronic interactions on the nanoscale, which makes STS ideal for observing strongly correlated spectral gaps, quasiparticle scattering processes, nanoscale charge order, and sub-angstrom broken symmetries. In this thesis, I will discuss experiments I have conducted using scanning tunneling microscopy and spectroscopy on topological insulators and the Bi-based cuprate superconductors.

In Chapter 2, I describe the technique of scanning tunneling microscopy and spectroscopy,

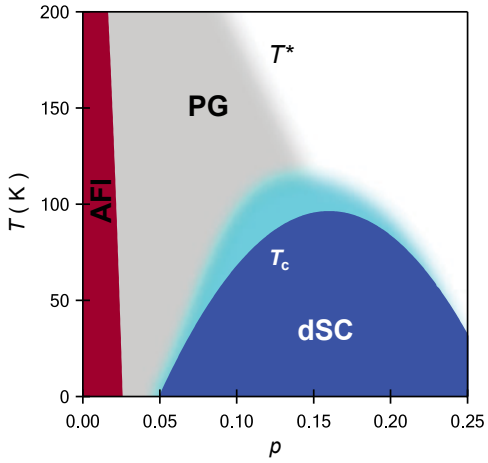

Figure 1.7: Phase diagram of hole-doped cuprates. At low doping p, the cuprates are antiferromagnetic insulators (AFI), upon doping, at low T, the cuprates enter the d-wave superconducting state (d-SC). On the underdoped side of the phase diagram $p \lesssim 0.16$, at temperatures above T_c, the system enters the pseudogap phase, which has an onset temperature of T^*. Figure adapted from Ref. [25].

details on the experimental apparatus and develop the formalism for differential tunneling spectroscopy.

In Chapter 3, I describe experiments performed on the purported topological Kondo insulator, SmB_6, predicted to have topological surface states that span a strongly correlated hybridization gap [26].

In Chapter 4, I describe experiments performed on $Bi_{2-x}Fe_xSe_3$, where I imaged quasiparticle scattering processes of the topological surface states and trivial 2D quantum well states [27].

In Chapter 5, I describe experiments performed on underdoped $Bi_2Sr_{2-x}La_xCuO_{6+\delta}$, where I found a surface charge ordered state that agreed with a bulk charge ordered state, providing the first confirmation of bulk and surface charge order in the cuprates [28].

In Chapter 6, I describe experiments performed on Pb-doped Bi-2201, where we investigated the experimental limitations of purported broken intra-unit cell electronic rotational symmetry in the cuprates.

2

Scanning Tunneling Microscopy

This chapter describes the principal experimental techniques used in this thesis, scanning tunneling microscopy and spectroscopy. We start by discussing the theory of electron tunneling. We follow up with a description of the main experimental apparatus, a home-built scanning tunneling microscope (STM) built in the Hoffman Lab at Harvard University. The final section describes the different STM measurements that are extensively used in this thesis.

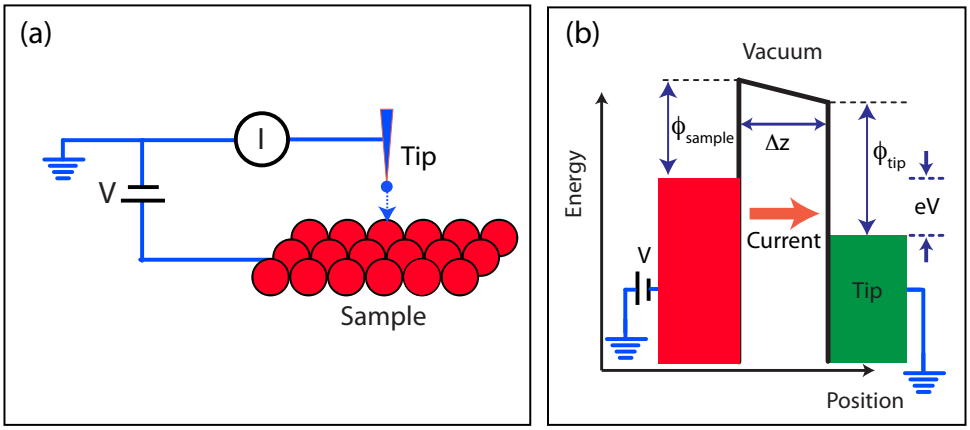

Figure 2.1: Principles of tunneling between a STM tip and a sample. (a) Illustration of the tip-sample tunneling process. A voltage V is applied between an atomically sharp STM tip and the sample, and results in a tunneling current I. **(b)** Illustration of the tunneling process from a spectroscopic point of view. The occupied states of the sample and tip are shown in red and green respectively, offset in energy by eV because of an applied voltage V. ϕ represents the respective work functions of the sample and tip, Δz represents the spatial separation between the tip and sample.

2.1 Theory of Electron Tunneling

Scanning tunneling microscopy relies on the principle of electron tunneling. In our case, we consider an atomically sharp PtIr wire, called our STM tip, which is placed within angstroms of a sample. A schematic of this situation is shown in Fig. 2.1a. If we apply a voltage to the sample, even if the electron does not have sufficient energy to leave the tip and enter the sample, there is a non-zero probability that the electron will spontaneously jump, or "tunnel", between the tip and the surface (or vice versa). This process is forbidden classically, and is a fundamentally quantum phenomenon. A scanning tunneling microscope (STM) measures the resulting electron tunneling current at different locations of the sample, which creates a spatial map of the electronic properties of the sample.

2.1.1 Toy Model in One Dimension

The simplest case of tunneling occurs for a particle in one dimension. Consider an electron with energy E that is incident on a potential barrier:

$$V(z) = \begin{cases} V_0 & \text{if } L > z > 0 \\ 0 & \text{else} \end{cases} \tag{2.1}$$

If $V_0 > E$, the solutions to the Schrodinger equation for the wavefunction in the barrier region $L > z > 0$ have the form:

$$\psi(z) \propto \exp(-\kappa z) \tag{2.2}$$

where $\kappa = \sqrt{2m(V_0 - E)}/\hbar$, m is the mass of the electron, and $1/\kappa$ is the lengthscale of the potential barrier at which tunneling can occur. In typical experiments, the vacuum potential barrier is the energy to remove an electron from the material, known as the work function, and is typically $\sim 3 - 5$ eV. This results in a tunneling length scale of $\kappa^{-1} \sim$ Å. Because the probability that an electron will traverse the potential barrier is $\sim |\psi(z = L)|^2 \propto \exp(-2\kappa L)$, the width of the potential barrier must be approximately $L \sim \kappa^{-1}$ for electrons to tunnel across the barrier. This leads to the constraint that the STM tip must be within angstroms of the surface to measure a tunneling current. Furthermore, the exponential dependence of the tunneling probability means that if $\kappa^{-1} \sim 1$ Å(as is typical), for a 1 Å change in Δz the tunneling probability increases by an order of magnitude. The exponential dependence of the tunneling probability on the separation between the tip and the sample allows the STM to have such fine control over the position of the tip.

2.1.2 Derivation of the Tunneling Current

With the previous intuition, let us move on to formally evaluating the tunneling current from the sample to our tip when we apply a negative bias $-V$ to the sample while holding our tip at virtual ground. This situation is illustrated in Fig. 2.1b. The negative bias on the sample effectively

raises the Fermi level of the sample by $+eV$ relative to the Fermi level of the tip. Because the occupied states of the sample are higher in energy than that of the tip, current will flow from the sample to the tip. The probability that an electron of energy E (relative to the respective Fermi levels) in the sample will tunnel into the tip is, by Fermi's golden rule:

$$P_{s\to t} = \frac{2\pi}{\hbar}|M|^2 \cdot N_s^{\text{filled}}(E)N_t^{\text{empty}}(E+eV) \tag{2.3}$$

where N_s^{filled} and N_t^{empty} are the number of filled states in the sample, and the number of empty states in the tip, respectively, and M is the tunneling matrix element. If we use a WKB approximation to the tunneling matrix element, then:

$$|M|^2 \approx \exp(-2\kappa\Delta z) \tag{2.4}$$

where Δz is the distance between the tip and the sample, $\kappa = (2m\bar{\phi})^{1/2}/\hbar$ is the local barrier height in terms of the mass of the electron m, $\bar{\phi} = (\phi_s + \phi_t)/2$ is the average work function given in terms of ϕ_s and ϕ_t, the sample and tip work functions respectively. This tunneling matrix element is analogous to the exponential dependence of the wave function solutions in one dimension discussed earlier in Eqn. 2.2. $N_s^{\text{filled}}(E)$ and $N_t^{\text{empty}}(E)$ depends on the density of states in the tip or sample, and the Fermi-Dirac distribution, and is given by:

$$N_s^{\text{filled}}(E) = \rho_s(E)f(E), \tag{2.5}$$

$$N_t^{\text{empty}}(E+eV) = \rho_t(E+eV)(1-f(E+eV)) \tag{2.6}$$

where ρ_s and ρ_t are the sample and tip density of states respectively, and $f(E)$ is the Fermi-Dirac distribution at temperature T, given by:

$$f(E) = \frac{1}{1+\exp(E/k_BT)}. \tag{2.7}$$

The total tunneling current from sample to tip ($I_{s\to t}$) is then taken by summing over all energy states (including spin degeneracy), and including the charge of the electron, and noting that under most realistic assumptions, the matrix element is independent of energy [29].

$$I_{s\to t} = -e\frac{2\pi}{\hbar}2e^{-2\kappa\Delta z}\int_{-\infty}^{+\infty}(\rho_s(E)f(E))\cdot(\rho_t(E+eV)(1-f(E+eV))dE \tag{2.8}$$

By a similar analysis the current from the tip to the sample has the form:

$$I_{t\to s} = -e\frac{2\pi}{\hbar}2e^{-2\kappa\Delta z}\int_{-\infty}^{+\infty}(\rho_t(E+eV)f(E+eV))\cdot(\rho_s(E)(1-f(E))dE \tag{2.9}$$

The total tunneling current from the sample to the tip is a sum of Eqn. 2.8 and 2.9, and is simplified to:

$$I = \frac{-4\pi e}{\hbar}e^{-2\kappa\Delta z}\int_{-\infty}^{+\infty}\rho_s(E)\rho_t(E+eV)\cdot\{f(E)[1-f(E+eV]-[1-f(E)]f(E+eV)\}dE \tag{2.10}$$

The tunneling current in the form of Eqn. 2.10 can be further simplified if the sample and tip are at low temperatures. At $T = 4.2$ K, the width of the Fermi function is $\sim k_BT = 0.36$ meV, and therefore on energy scales larger than k_BT, $f(E)$ is effectively a step function centered at E_F. In the experiments described in this thesis, the experimental energy resolution was often ≥ 1 mV. The result is that the integral,

$$\int_{-\infty}^{+\infty}\{f(E)[1-f(E+eV]-[1-f(E)]f(E+eV)\}dE \neq 0 \quad \text{for:} \quad \int_{-eV}^{0}dE$$

This simplifies Eqn. 2.10 to:

$$I \approx \frac{-4\pi e}{\hbar}e^{-2\kappa\Delta z}\int_{-eV}^{0}\rho_s(E)\rho_t(E+eV)dE \tag{2.11}$$

If we choose a tip with a flat density of states near the Fermi energy, and relative to the energy scales to be studied, then $\rho_t(E+eV)$ is constant in the energy range $[E_F - eV : E_F]$, and can be

taken out of the integral and so:

$$I(V) \approx \frac{4\pi e}{\hbar} e^{-2\kappa\Delta z} \rho_t \int_{-V}^{0} \rho_s(eV')dV' \tag{2.12}$$

(where we have also dropped the sign and are measuring the magnitude of the current). Together this approximates the tunneling current as,

$$I(V) = I_0 e^{-2\kappa\Delta z} \int_{-V}^{0} \rho_s(eV')dV' \tag{2.13}$$

where $I_0 = \frac{4\pi e}{\hbar}\rho_t$ is a constant that has units of current. The expression of the tunneling current in Eqn. 2.13 is most commonly used to explain STM tunneling. It relates I exponentially to the tip-sample separation, and to the integrated spectral weight of the sample from E_F to $E_F - eV$. Furthermore, I is only significant when when $\kappa\Delta z \sim 1$, implying that for $\bar{\phi} \sim$ eV, the tip must be within angstroms of the surface.

2.2 The Scanning Tunneling Microscope

Scanning tunneling microscopy, first developed by Binnig and Rohrer in 1982 [30], is the heart of the experimental apparatus used in this thesis. Because of the sensitivity of I to displacements of up to an angstrom, the STM must have spatial positioning on a sub-angstrom length scale. Furthermore, the STM used here was optimized in size and design for operations at low temperature and high magnetic field, which was necessary to probe topological materials and cuprate superconductors.

2.2.1 Principles of STM Operation

An illustration of the basic construction of an STM is shown in Fig. 2.2a. The tip is a mechanically cut PtIr wire that is mounted on top of a piezoelectric tube. The piezoelectric tube has five quadrants ($\pm X$, $\pm Y$, Z), and upon application of a voltage to any of the quadrants, the piezo tube deflects in the given direction. The tunneling current I is measured upon application of a

voltage V_s between the tip and the sample. By ramping the voltage on the ($\pm X$, $\pm Y$) piezos, the tip deflects to a different part of the sample surface, allowing the STM to measure electrical properties at different locations. Because the tunneling current is exponentially dependent on the separation between the tip and the sample, Δz, the voltage on the Z quadrant V_Z, effectively controls I. By increasing the voltage on Z, the tip extends, reducing Δz and exponentially increasing I. Likewise, by decreasing the voltage on Z, Δz increases, exponentially decreasing I. To maintain constant 'contact' with the surface, we employ a computerized feedback loop, called "feedback mode", to maintain a constant tunneling current. In feedback mode at a fixed voltage setpoint V_s, I is compared to a fixed current setpoint I_s, and the feedback loop varies V_Z to minimize $|I - I_s|$. In feedback mode, Δz depends on V_s and I_s, but is often characterized by the parameter V_s/I_s, called the junction resistance R_J. The junction resistance is roughly interpreted to represent Δz because for a given V_s, Δz is larger for high R_J, and Δz is lower for small R_J. R_J is typically $\geq$ 1 GΩ for V_s ranging from 100 mV to 1 V. For sufficiently high R_J when the STM is scanning in feedback mode, if the STM moves over a large impurity the computer will pull the tip away from the surface, preventing the tip from crashing into the surface. Feedback mode is therefore a computerized mechanism to control the STM tip and prevent unwanted tip crashes by always positioning the tip relative to the sample.

The STM head, shown in Fig. 2.2b, is housed at the bottom of a low temperature, low vibration cryostat that is bathed in liquid helium. The walls of the cryostat are in contact with liquid helium at $T = 4.2$ K, ensuring an excellent vacuum inside the cryostat. The cryostat is inserted into the bore of a large superconducting magnet, that is capable of reaching magnetic fields of 9 T perpendicular to the sample surface. The samples that are studied are bulk single crystals, typically $\sim 1 - 2$ mm in length and width, glued to a copper sample holder to which we apply a bias while holding the tip at virtual ground. The samples are cleaved in situ inside the cryostat, at $\sim$ 30 - 50 K, and are immediately inserted into the STM. The cleave exposes a fresh layer of the sample that is uncontaminated, and the cryogenic vacuum ensures the cleanliness of the surface on month-long time scales. The use of liquid helium allows us to have a base temperature of $T \sim 4.4$ K for up to 5 days. Pumping on the liquid helium filled "1K Pot", cools the liquid in

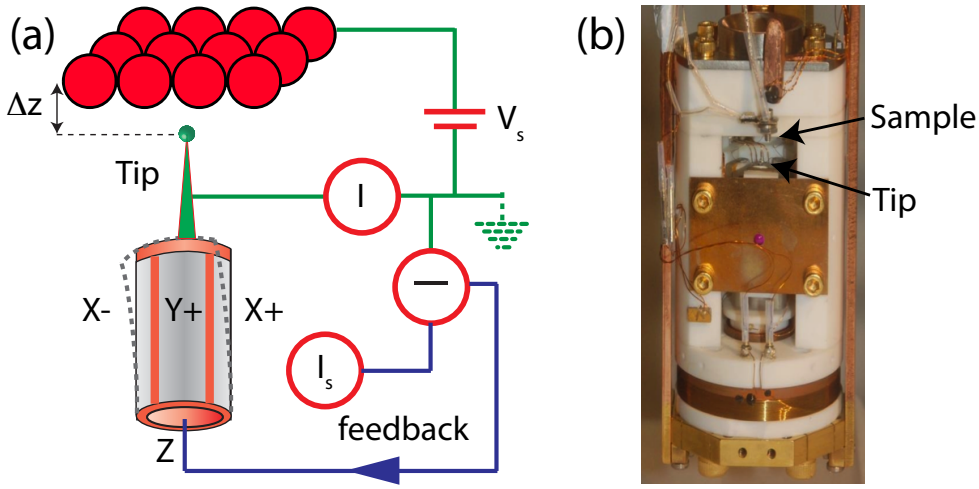

Figure 2.2: The Scanning Tunneling Microscope. (a) Schematic of the operation of a scanning tunneling microscope in feedback operation. The tip is mounted to a piezoelectric tube with quadrants ($\pm X$, $\pm Y$, Z). Voltage V_s is applied to the sample, Δz is the separation between the tip and the sample, the tunneling current I is measured from the tip, and related to the setpoint current I_s in a feedback loop on the Z piezo. **(b)** Picture of the STM head. The tip and sample are indicated with arrows and are in the same orientation as the tip and sample in (a). For scale, the STM head is approximately 2.5 inches in diameter.

the pot and can bring our base temperature down to $T \sim 2.2$ K. Heat can be applied to a length of wound wire around the base of the STM head, which allows the STM temperature to reach 50 K. Therefore the full operating range of our variable temperature STM is 2 - 50 K. Full details about the design of this STM are detailed in Dr. Yi Yin's Ph.D. Thesis [31], and additional upgrades were documented by Dr. Anjan Soumyanarayanan.

2.2.2 1K Capillary Upgrade

In the summer of 2010, fellow graduate students Tess Williams, Anjan Soumyanarayanan and I embarked on a major upgrade of the cryostat that was designed by Dr. Yin. The main purposes of the upgrade were to plug a number of leaky soft-solder joints on the cryostat flange directly in contact with the liquid helium bath, and to rewire the DC wires of the system. Figure 2.3a shows a picture of the middle of the cryostat, with the new DC wires indicated. The wires are sheathed in a braid and inserted through the vacuum line that pumps on the main vacuum space. At each stage they are wound and thermally glued to a gold plated copper bobbin that is pressed against

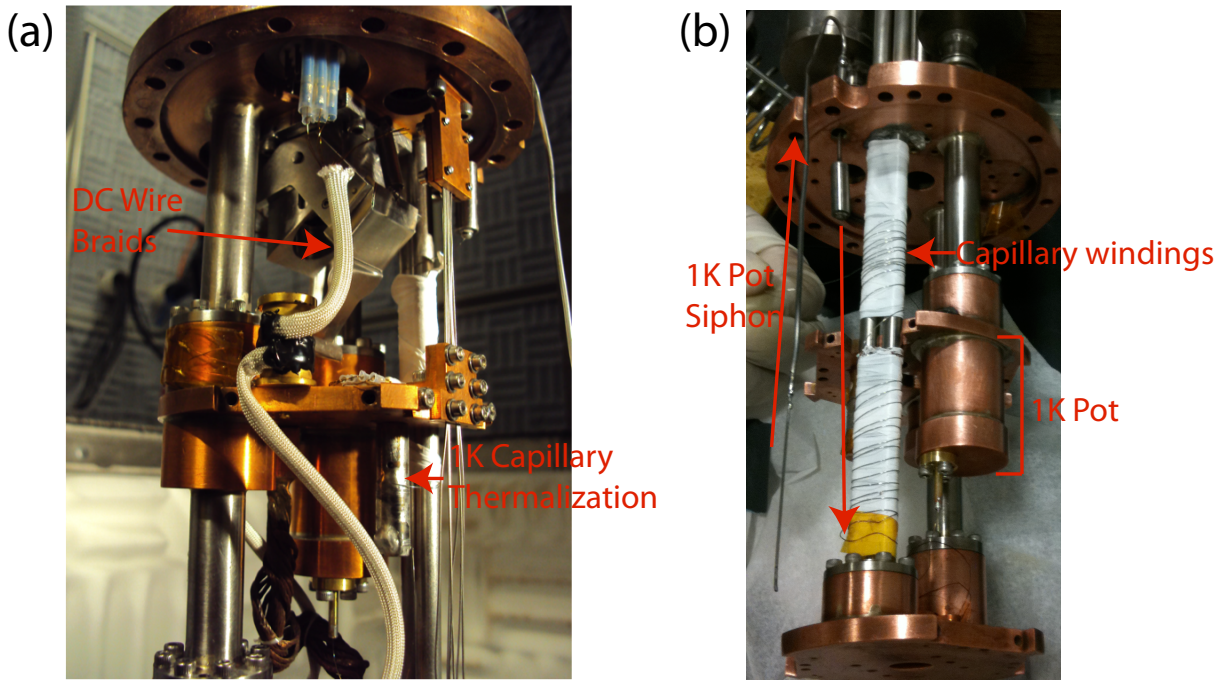

Figure 2.3: Cryostat Upgrades. (a) View of the middle of the cryostat looking up from the STM head. New DC wire braids are shown protruding out of the main vacuum line, and are thermalized at different stages to the cryostat. The 1K Pot capillary is soldered to a thermalization post and pressed against the 1K flange. **(b)** Construction of the 1K Capillary and Pot. The 1K Pot siphon extends into the helium bath and sucks in helium along the arrows shown. The capillary is loosely wound around the heat switch pumping lines before being thermally sunk to the post shown in (a). After thermalization, the capillary is threaded into the 1K Pot.

the thermalization stage.

One major upgrade involved repairing the damage done to the 1K Pot, which had become clogged with oil that had been back-streamed from an oil-pump. As can be seen in Fig. 2.3b, a thin capillary sucks in liquid helium from the bath, and pools the liquid directly in the 1K Pot. By pumping on the Pot, the temperature of the helium is reduced and it cools the STM to 2.2 K. However, to maintain a constant temperature, the liquid helium in the pot must be continuously replenished, and so a careful balance between the input and output of the helium into the pot is required. While some systems use a needle valve to control the flow of helium into the pot, through consultations with Dr. Joan Hoffmann we chose to use a fixed flow impedance between the helium bath and the 1K Pot. The impedance comes mainly from choking the flow of helium

from the bath to the pot through a long narrow capillary. We ended up using 12 feet of 0.1mm ID, 0.3mm OD, CuNi capillary ("german silver", $CuNi_{18}Zn_{20}$, or Cu 62%, Ni 18%, Zn 20%) purchased from GVL Cryoengineering in Germany. It is important to ensure that the liquid helium is superfluid before it enters the 1K Pot to reduce mechanical vibrations that could ruin the operations of our STM [32, 33]. To that end, we wound 5 feet of the CuNi capillary around a gold plated Cu post that was pressed into thermal contact against the the cryostat, as shown in Fig. 2.3a. We soldered the capillary to the thermalization post using rosin flux activated electrical solder ($\sim$ 96.5% Sn, 3% Ag) to achieve a strong thermal connection. Two feet of the capillary are used to connect the outer bath to the thermalization post, and five feet are used between the thermalization post and the 1K Pot. The 1K Pot capillary was successfully installed and tested in the summer of 2010, and allows for continuous operation for 4 days at 2.2 K, with no noticeable mechanical vibrations. The temperature of the 1K Pot immediately reaches $\sim$ 1.2 K when the Pot is initially pumped on, but the temperature saturates at 2.2 K after $\sim$ 15 minutes due to a thermal short from the STM head to the bath. Future improvements will involve removing this thermal short to enable a base temperature of 1.2 K.

2.3 Measurement Modes

In our STM, the tip is held at virtual ground while a bias V is applied to the backside of the sample. By tuning the voltage on the z-piezo so that $\Delta z \sim$ Å, a finite tunneling current will arise between the tip and the sample. By fixing the voltage to the z-piezo, we could in principle raster the tip across the surface and measure $I(\vec{r}, V)$. However this quantity is not particularly useful, as the tip sample separation $\Delta z = \Delta z(\vec{r})$ will vary depending on the corrugation of the surface, and so the exponential prefactor in Eqn. 2.13 will vary locally. Instead, we perform a number of other measurement techniques at each location.

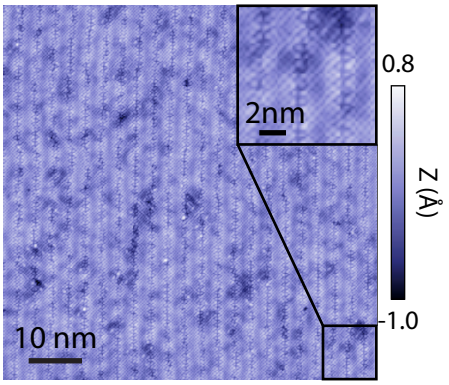

Figure 2.4: Topography using an STM. Topographic image of $Bi_2Sr_2CaCu_2O_{8+\delta}$ (underdoped, $T_c = 68K$) acquired over a 70×70 nm^2 region. Inset is a magnified image of a 10×10 nm^2 region. Topography was conducted at $T = 8$ K, $V_s = -100$ mV, $I_s = 30$ pA.

2.3.1 Topography

We use topography mode to map out the structural surface corrugations. When performing topography, we enable feedback at (V_s, I_s) to fix the tunneling current $I(\vec{r}, V_s) = I_s$, and raster the tip over the surface. The z-position of the tip at each point in a region of the surface, $z(\vec{r})$, defines a z-contour of constant current, which we call the "topographic image". Strictly speaking, the topograph is a contour map of constant current, and does not correspond to the "structure" of the surface. However, we typically take the topograph to be representative of the "surface structure", because if we approximate that,

$$\int_{-V_s}^{0} \rho_s(\vec{r}, eV')dV' \approx \text{constant for all } \vec{r} \tag{2.14}$$

and $I(\vec{r}, V_s) = I_s$, $\Delta z(\vec{r})$ will be constant for all $\vec{r}$. If the surface has structural corrugations, for example from the atomic lattice, then z will have to extend or retract to maintain constant Δz. In this case the contour of z, defined as the extension and retraction of z, directly maps out the "surface structure" of the sample. An example of an image acquired in topography mode is shown in Fig. 2.4.

In principle the condition in Eqn. 2.14 is not strictly true (because if it were, there likely would not be interesting physics!). In reality, topography measures variations in the tip sample separa-

tion $z \approx \delta(\Delta z)$ at a fixed current. By inverting Eqn. 2.13 we obtain, the relation that:

$$\Delta z(\vec{r}) = \frac{-1}{2\kappa} \cdot \ln \left[\frac{I_s/I_0}{\int_{-V_s}^{0} \rho_s(\vec{r}, eV')dV'} \right] \tag{2.15}$$

The tip sample separation will vary, in addition to the surface corrugations, by the variation in the integrated density of states: $\int_{-V_s}^{0} \rho_s(\vec{r}, eV')dV'$. And so strictly speaking, the current contains information pertaining to the integrated spectral weight at each location. Therefore topographic images will often obtain integrated spectroscopic information, and choosing V_s is key to obtaining an image that is representative of the structure alone.

2.3.2 Tunneling Conductance Spectroscopy

The topography is not very useful for obtaining spectroscopic information about the sample density of states because it integrates in energy. Instead, we perform differential tunneling conductance spectroscopy to measure the density of states of the sample.

At a fixed position $\vec{r}$, the derivative with respect to V of $I(V)$ is (from Eqn. 2.13):

$$\frac{dI}{dV}(V) = [I_0 \exp(-2\kappa\Delta z)] \cdot \rho_s(eV) \tag{2.16}$$

$$\frac{dI}{dV}(V) \propto \rho_s(E_F + eV) \tag{2.17}$$

which directly measures the density of states at energy eV relative to the Fermi level (to an overall prefactor that we discuss later). To measure dI/dV, instead of performing a numerical derivative of I vs V, which requires high energy resolution to avoid errors, we instead use a standard lockin technique. We apply an oscillation excitation to the sample of the form $V_{\text{ac}}(t) = dV\cos(ft)$, and use a lockin to measure the current response dI at frequency f. Therefore by varying the voltage V, and measuring the current response at each voltage $dI(V)$, we are in principle measuring $\rho(eV)$ (we then scale $dI(V)$ by $dV_{\text{rms}} = dV/\sqrt{2}$ to obtain units of conductance, typically on the order of $\sim$ nS). An example of a typical dI/dV spectrum is shown in Fig. 2.5.

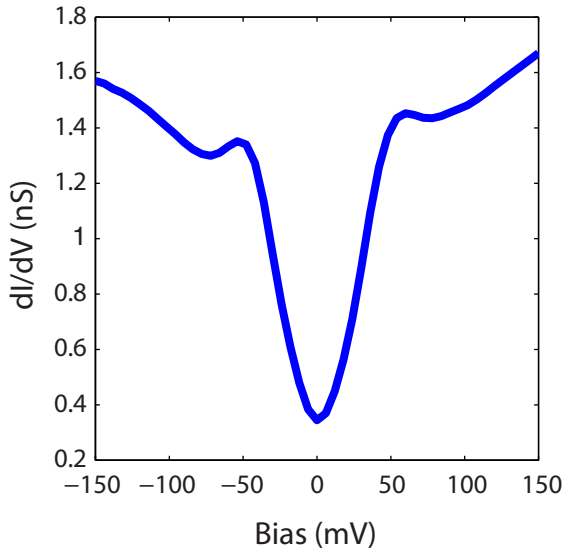

Figure 2.5: Tunneling conductance spectroscopy using an STM. dI/dV spectrum acquired on the $Bi_2Sr_2CaCu_2O_{8+\delta}$ surface shown in Fig. 2.4. Spectrum acquired at $T = 6$ K, $V_s = -150$ mV, $I_s = 150$ pA, $V_{\text{rms}} = 3.5$ mV, integration time $\tau = 12$ ms, $dV_{\text{pix}} = 6$ mV.

The typical experimental sequence of dI/dV spectroscopy consists of the following. At any given position, we first fix the z-position of the tip by varying z in feedback at the setpoint conditions (V_s, I_s). The computer feedback control is then disabled to allow us to vary V without changing Δz. We then vary V through a series of discrete values and measure dI/dV at each V over a specified integration period τ. At the end, feedback mode is re-enabled to fix (V_s, I_s).

The controllable parameters to maximize the signal to noise ratio are the bias oscillation amplitude dV, the setpoints (V_s, I_s), and the integration period τ. Typically, R_J is chosen more aggressively than in topography mode to reduce Δz and increase the signal. This however pushes the tip closer to the sample and risks the stability of the tip or a tip crash. Alternatively, we could increase the bias oscillation amplitude dV, which instead sacrifices energy resolution by smearing features over an energy scale of $\sim \sqrt{2}dV$. Lastly, we could increase the integration period τ at each bias . However, this last option leaves the tip out of computer feedback for longer and risks crashing the tip. A combination of the experimenter's sense of adventure, and scientific requirements typically determines what combination of variables will be used. The frequency used in our STM is chosen to be off-resonance from any other known excitations and is chosen to

be 1.115 kHz. Typically we choose $\sim$ 10 oscillation amplitudes as our period $\tau \approx 10 - 20$ ms. R_J is typically chosen to be < 1 GΩ, for a V_s that is outside of the range of interest. The energy pixel resolution is usually determined by the available experimental time, and the thermal energy resolution: $dV_{\text{pixel}} = (V_f - Vi)/N_E \approx dV_{\text{rms}} \approx dV_{\text{thermal}}$, where V_f and V_i are the final and initial voltages of the spectroscopy voltage range, N_E is the number of energy pixels, and $dV_{\text{thermal}} \sim 3.5k_BT - 4k_BT$ [34]. The magnitude of the thermal broadening at 4.2 K is $\sim 1.2 - 1.4$ meV, and so the energy resolution of the dI/dV measurements, $dE = \sqrt{dV_{\text{pixel}}^2 + dV_{\text{rms}}^2 + dV_{\text{thermal}}^2}$ is typically $dE \sim 2 - 3$ meV.

2.3.3 Scanning Tunneling Spectroscopic Maps

Combining the ability to map surface structure in topography, with the ability to probe the density of states allows us to perform scanning tunneling spectroscopy (STS). In this mode of operation we perform dI/dV spectroscopy at every point within a pixel grid over a large field of view. The result is a three dimensional dataset: (x, y, eV), which allows us to spatially visualize the density of states oscillations at a given E, or measure the density of states at a given location (x, y) in energy. This operation mode is schematically represented in Fig. 2.6.

Functionally, STS maps are experimentally challenging to acquire. A pixel grid is typically defined over a region of space with a resolution that ranges from 1 pixel per atom to upwards of 50 pixels per atom. The computer controls the tip and starts by moving to one pixel in feedback, it then engages feedback to fix Δz, acquires a dI/dV spectrum, re-engages feedback to fix Δz, moves the tip to the next pixel, and then repeats the procedure. The challenge of acquiring these datasets lies in ensuring that the experimental conditions of the system remain constant over the time required to complete a dataset. A typical dataset can involve up to 256×256 spatial pixels, spectra with 101 energy pixels, with a 10 ms integration period at each energy. In this case the required time is at least, $256 \times 256 \times 101 \times 10$ ms $= 18$ hours. To ensure that the data taken at the end of the map can be compared to the data acquired at the beginning, all experimental parameters must remain constant over this time frame. This essentially demands that the temperature,

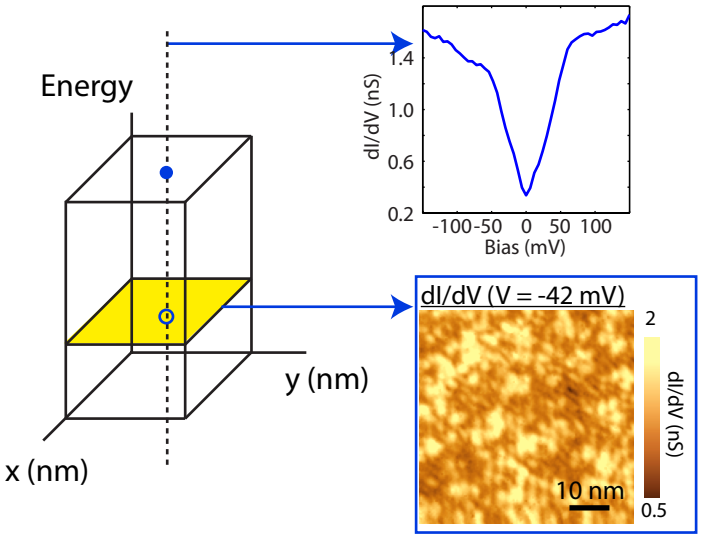

Figure 2.6: Scanning tunneling spectroscopy maps. Schematic representation of the three dimensional dataset acquired in dI/dV spectroscopy maps. Data is acquired in a spatial pixel grid (x, y), and an energy pixel axis (V). At fixed (x, y), $dI/dV(V)$ is a point spectrum that is proportional to the local density of states. At fixed V, $dI/dV(x, y)$ is an image where the color scale represents the dI/dV intensity locally. STS map was acquired using a 256×256 pixel grid over a 52×52 nm^2 region of $Bi_2Sr_2CaCu_2O_{8+\delta}$ (UD, $T_c = 68$ K), at $T = 6$ K, $V_s = -150$ mV, $I_s = 150pA$, $V_{\text{rms}} = 3.5$ mV.

magnetic field, scan piezos, and tip be experimentally stable for up to 18 hours. Furthermore because the tip is constantly taking spectra out of feedback, the tip is being exposed to potentially experiment ruining events triggered by mechanical vibrations, or tip-sample interactions. All of these conditions make acquiring high quality STS datasets extremely challenging!

Fourier Transform Scanning Tunneling Spectroscopy Maps

As discussed in the previous section $dI/dV(\vec{r}, V)$ images can be interpreted as mapping the local density of states $\rho(\vec{r}, E)$. In a 2D electron gas system, $\rho(\vec{r}, E)$ is a k-space average of all of the Bloch wavefunctions ψ_k, at a single spatial location $\vec{r}$.

$$\rho(\vec{r}, E) = \int \psi_{\vec{k}}(\vec{r})\delta(\epsilon - E(\vec{k})d\vec{k} \tag{2.18}$$

As a result, STS experiments contain no direct $\vec{k}$-space information of the quasiparticle eigenstates. However, what then do we make of periodic modulations in dI/dV images, such as those

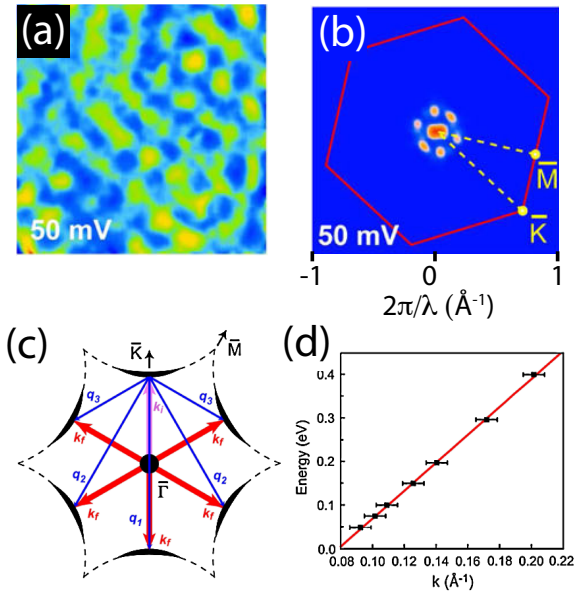

Figure 2.7: Quasiparticle Interference. Figures adapted from quasiparticle interference seen on Bi_2Te_3 in Ref. [35] **(a)** dI/dV map of Bi_2Te_3 over a 28×28 nm^2 region at $V = 50$ mV. **(b)** FT-dI/dV map of the map shown in (a), with high intensity peaks corresponding to the periodicity seen in (a). **(c)** Illustration of the constant energy contours and allowable scattering wavevectors **(d)** Dispersion of the wavevector shown in (b).

seen in Fig. 2.7a? To better visualize and quantify the periodicity of the modulations, we typically perform Fourier transforms of the $dI/dV(\vec{r}, V)$ maps at each energy. The result is another three dimensional dataset in (q_x, q_y, V) space, and a series of Fourier transform (FT)-dI/dV images at constant energy. One of those maps is seen in Fig. 2.7b.

Peaks in FT-dI/dV maps at wavevectors $q = 2\pi/\lambda$ correspond to spatial modulations with a periodicity λ. The origin of these modulations depends on whether the q-space peaks disperse with energy. Non-dispersive q-peaks correspond to static charge modulations, and can be caused by periodicities such as the atomic lattice, or charge density waves, such as in $NbSe_2$. Dispersive q-peaks on the other hand have a different interpretation, and correspond to standing interference patterns of quasiparticle states. In the presence of disorder, induced for instance by impurities or step edges, the translational invariance of the Bloch states is broken, giving rise to a standing wave interference pattern, which is imaged in dI/dV and FT-dI/dV maps. In the simplest case, for an inbound state $\psi_{\vec{k}_i}$ on an impurity, and an outbound state $\psi_{\vec{k}_f}$, the scatter-

ing vector between the two states: $|\vec{q}| = |\vec{k}_f - \vec{k}_i| = 2\pi\lambda^{-1}$ will determine the wavelength λ in dI/dV. If we consider only elastic scattering processes, at a given energy all of the occupied $\vec{k}$ states form a constant energy contour (CEC) in k-space. For each occupied $\vec{k}$ state, the allowed final scattering states are all other states on the CEC: $\{\vec{k}_f(E)\} = \{\vec{k}(E) \neq \vec{k}_i(E)\}$. And so the q-space FT-dI/dV map at energy E can be interpretted as the autocorrelation of the CECs at energy E. If we include weighting to the CEC from the single particle spectral function $A(\vec{k},\omega)$, the FT-dI/dV map is formally:

$$\text{FT}-\frac{dI}{dV}(\vec{q},\omega) \sim \text{ JDOS}(\vec{q},\omega) = \int_{\text{CEC}} d^2k A(\vec{k},\omega)A(\vec{k}+\vec{q},\omega) \tag{2.19}$$

where JDOS represents the joint density of states and is formally the autocorrelation of the single particle spectral function throughout the Brillouin zone. Dispersive peaks or shapes in FT-dI/dV maps can then be interpreted as the dispersion of the joint density of states, which arises from the dispersion of scattering wavevectors that connect high DOS points in k-space, or the dispersion of a common $\vec{q}$ that connects nested portions of the CEC. Because the CEC evolve with energy, with some knowledge of the underlying CECs, dispersion of $\vec{q}$ in FT-dI/dV can give information on the dispersion of the original $\vec{k}$ states. Therefore by using this technique, STS can map the evolution of the k-states to energies above the Fermi level and with higher energy resolution than other spectroscopic probes.

3

Imaging the Kondo Insulating Gap on SmB_6

Recent work has predicted non-trivial topology within a subset of Kondo insulators. These predicted topological Kondo insulators, in particular SmB_6, would represent the emergence of topological order from a strongly correlated gap. In this chapter, we detail experiments mapping the local inhomogeneity of SmB_6 as a function of temperature. We measure the hybridization gap on a non-polar reconstruction, and find temperature dependent spectroscopic evidence consistent with Kondo hybridization and in-gap surface states. Some of the results from this chapter can be found in Ref. [26]: Yee, Soumyanarayanan, He, Kim, Fisk & Hoffman, **arXiv**: 1308:1085 (2013).

3.1 Introduction to Kondo insulators

SmB_6 belongs to a class of materials known as heavy fermion (HF) materials. HF compounds typically contain rare earth or acitinide elements (e.g. Ce, Sm, Yb, etc.), which impart a localized magnetic moment [36] into the crystal lattice. The unique physics of HF materials involves the interaction of these magnetic ions with the itinerant electrons via the Kondo effect [36, 37]. The Kondo effect is well understood for a single localized electron with a magnetic moment immersed in a sea of itinerant electrons. At high temperatures the itinerant and localized electrons do not interact. However at temperatures below the Kondo temperature T_K, the spins of the itinerant electrons screen the magnetic moment of the localized electron, creating a localized spinless site [38]. This localized spinless site serves as a strong scattering site increasing the resistivity of the material leading to the characteristic upturn in the resistivity seen in Kondo systems. Extending this phenomenon from the single ion case to a Kondo lattice, a similar magnetic screening interaction occurs between the conduction electrons and each magnetic moment in the lattice. The dispersionless band of the magnetic moments and the itinerant electrons hybridize, forming a hybridized band with a high effective mass. The cartoon in Fig. 3.1 illustrates the Kondo hybridization in a lattice. If the Fermi level of the material sits close to the f state energy, then the Kondo hybridization of the f and conduction states causes a gap to open at the Fermi level, creating a temperature dependent metal insulator transition at T^* [36].

Recently, it was suggested that the classification of solids based on topological invariants could apply to these strongly correlated Kondo insulators [39, 40]. Like in the traditional band insulator case, symmetries would protect chiral surface states that would span the band gap, or in this case, the Kondo induced hybridization gap. In contrast to the first generation of TIs, where the band gap arises from band-theory, in HF materials the band gap is intrinsically a strongly correlated temperature dependent effect caused by the hybridization of localized and itinerant electrons. These topological Kondo insulators (TKIs) therefore could exist with protected chiral surface states within the Kondo hybridization gap, and would represent a rich new physical class of materials combining topology with strongly correlated physics. SmB_6, one of the oldest

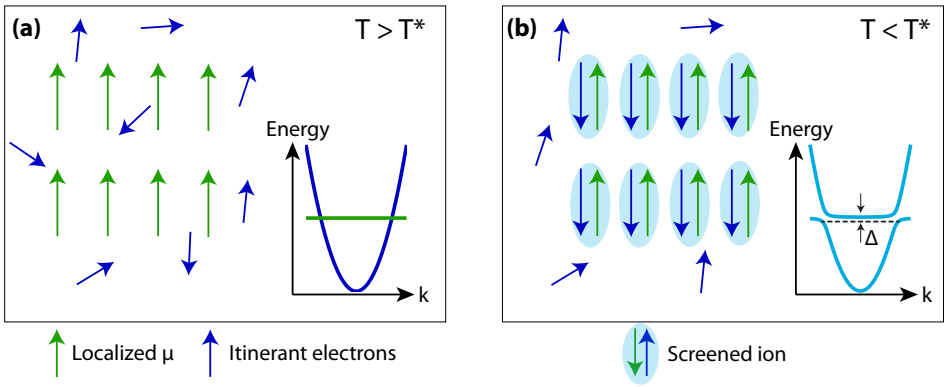

Figure 3.1: llustration of the Kondo effect in a lattice. **(a)** At $T > T^*$ the magnetic moments (green arrows) are arranged in a lattice surrounded by the itinerant electrons (blue arrows). The inset shows the respectively coloured bands of the magnetic moments and the conduction electrons. **(b)** At $T < T^*$ the spins of the itinerant electrons screen the magnetic moments creating localized spinless scattering centers, and the two bands hybridize opening a band gap.

studied Kondo insulators, has repeatedly been proposed as an ideal TKI candidate [39–42].

3.2 SmB_6 as a potential Topological Kondo Insulator

SmB_6 was one of the first discovered Kondo insulators and has subsequently been studied as a HF material since the 1970s. SmB_6 has a CsCl-type cubic crystal structure with alternating Sm^{2+} ions and ${B_6}^{2-}$ octahedra, shown in Fig. 3.2a. It undergoes a metal to insulator transition around 50 K [43–45], as shown in Fig. 3.2b, which was attributed to hybridization between the Sm $4f$ localized moments and the B $5d$ conduction band. Surprisingly however, the resistivity saturates below ∼3 K [43, 45], in contrast to the expectation that resistivity increases, and conductivity $\to 0$ as $T \to 0$. While this residual conductivity at $T = 0$ was originally thought of as an impurity band, recent proposals have attributed it to the existence of topologically protected surface states which would leave a residual conducting channel [39, 40]. Recent transport papers have shown evidence for the surface origin of this residual resistivity channel, while lacking concrete evidence proving the topological nature of the surface states [46–49]. However, numerous other experiments using point contact spectroscopy [50], quantum oscillation [51], and angle-resolved photoemission spectroscopy (ARPES) [52–57] have seen evidence supporting the

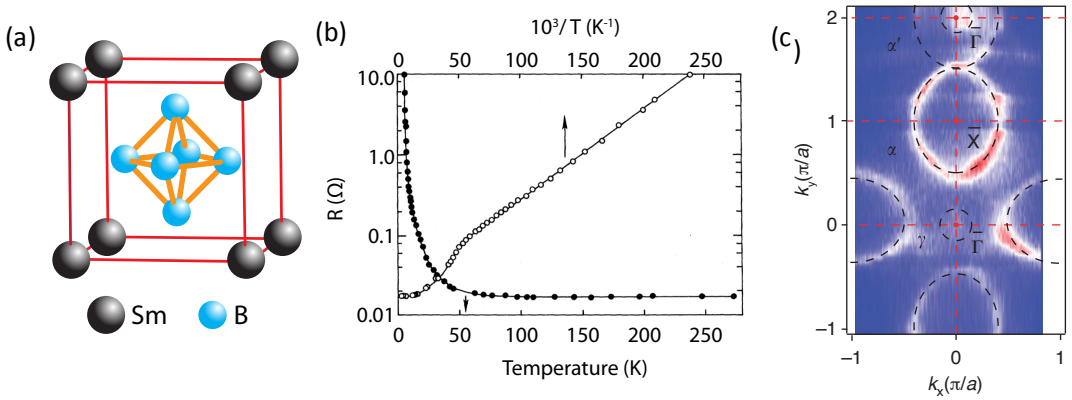

Figure 3.2: SmB_6 crystal structure, band structure and resistivity. **(a)** Schematic of the SmB_6 crystal structure. **(b)** Resistivity vs temperature of SmB_6. Data adapted from Ref. [43]. Filled circles denote R vs T; open circles denote R vs $10^3/T$. Metal insulator transition temperature T^* marked with downward pointing arrow at $\sim$ 50 K. **(c)** ARPES determined low energy band structure. Data adapted from Ref. [54]. Red color shows low energy occupied states below the Fermi energy.

existence of TSS. In particular, the dispersion and orbital chirality of some surface states [54], the half integer Berry phase from Landau levels [51], and the transport response to magnetic impurities [48] are strongly suggestive of nontrivial topology in SmB_6.

Although evidence is accumulating for topological surface states on SmB_6, a precise understanding of their properties is presently limited by poor spectroscopic information. ARPES experiments are in broad agreement on the band structure for energies below the Fermi level. SmB_6 is characterized by a parabolic band centered at the X point in the 3D Brillouin zone, as shown in the low energy band structure from Jiang et al. [54] in Figure 3.2c. However, knowing the band structure of the occupied states does not help to resolve the discrepancy over the magnitude of the hybridization gap in SmB_6. ARPES loosely identifies the magnitude of the hybridization gap as the binding energy of the sharp f band just below E_F, typically E_B $\sim$14-20 meV [52–57], without accounting for the band edge in the unoccupied states. Meanwhile, DC transport [43, 45, 58] and optical reflectivity [59] studies typically report a gap of $\Delta \sim$ 5-10 meV, but both the activation energy fits and the Kramers-Kronig transformations necessary to extract these gap energies may be affected by residual states in the gap [45, 58, 60]. Larger gaps of 19 meV and 36 meV have also been observed by optical transmissivity [60] and Raman spec-

Reference	Measured Δ (meV)	Technique
Menth, *et al.* [43]	4.6	Transport
Flachbart, *et al.* [58]	11.2	Transport
Travaglini, *et al.* [59]	4.7	Optical spectroscopy
Gorshunov, *et al.* [60]	19	Optical spectroscopy
Nyhus, *et al.* [61]	36	Raman spectroscopy
Guntherodt, *et al.* [62]	2.7	Point tunneling spectroscopy
Amsler, *et al.* [63]	14	Planar tunneling spectroscopy
Flachbart, *et al.* [58]	22	Point contact spectroscopy
Zhang, *et al.* [50]	18	Point contact spectroscopy
Miyazaki, *et al.* [52]	15	ARPES
Xu, *et al.* [53]	20	ARPES
Jiang, *et al.* [54]	18	ARPES
Neupane, *et al.* [56]	14	ARPES
Frantzeskakis, *et al.* [57]	5	ARPES
Zhu, *et al.* [55]	~15 - 20	ARPES
Denlinger, *et al.* [64]	~20	ARPES

Table 3.1: Reported hybridization gap values of SmB_6 from different experimental techniques

troscopy [61], respectively. However, transport and optical techniques cannot determine the gap center with respect to E_F. The inconsistencies in the gap are summarized in Table 3.1

Like STS, planar tunneling and point contact spectroscopy (PTS/PCS) are able to spectroscopically measure the unoccupied states. These measurements show the T-dependent opening of a gap ranging from ~3 to 22 meV [50, 58, 63]. However, PCS lineshapes in SmB_6-SmB_6 junctions vary dramatically with junction size [58], while PTS and PCS heterojunction experiments have shown an asymmetric peak on the positive energy side of the gap [50, 63], in contrast to the preponderance of theoretical and experimental evidence for an electron-like conduction band [42, 52–57, 65, 66]. It therefore is essential for an alternative probe to provide unambiguous spectroscopic information of the bare DOS and the full hybridization gap.

3.3 Surface studies of SmB_6 via STM

The aforementioned studies on SmB_6 averaged over at least several microns of surface area and provided no spatial information. Spatial averaging over large regions of SmB_6 is problematic be-

cause, unlike the first generation of Bi-based topological insulators, which are layered materials with natural cleavage planes, SmB_6 is a fully three dimensional material whose cleavage properties are unknown. As seen in Fig. 3.2a, SmB_6 has a CsCl-type cubic crystal structure with alternating Sm^{2+} ions and ${B_6}^{2-}$ octahedra. It is therefore expected that complete $Sm^{2+}(001)$ or ${B_6}^{2-}(001)$ terminations would be polar, resulting in surface band bending. On the other hand, a partial Sm surface may suffer from structural reconstructions as seen by low energy electron diffraction (LEED) [52, 67]. Although the topologically protected surface states are expected to exist on all surface morphologies, their manifestation may be influenced by the differing electronic environments in which they live. Furthermore, the possible shifts of the hybridization gap and/or coexistence of topologically trivial states on some surfaces may short out the fundamental chiral states of interest for transport devices. It remains crucial to quantify the hybridization gap itself, and to understand its variation with surface morphology. Therefore STM/STS is an ideal tool to probe variations in differential tunneling conductance dI/dV across multiple SmB_6 surface morphologies and provide crucial local spectroscopic information.

In our experiments, SmB_6 crystals were cleaved in cryogenic UHV at $T \sim 30$ K and immediately inserted into the STM. Because SmB_6 lacks a natural cleavage plane, the crystal cleaves in a jagged fashion, as shown in the SEM image of one of our cleaved surfaces in Fig. 3.3a. However, a number of flat terraces are visible and we chose to conduct our STM experiments on those specific terraces. After our STM experiments, we performed electron back scatter diffraction (EBSD) and x-ray photoelectron spectroscopy (XPS) measurements to verify that the cleave was in the (001) orientation, and that the surface was B rich. The surface chemical composition was determined by comparing the chemical peak intensities of the XPS spectrum, shown in the table in Fig. 3.3b, and are consistent with previous measurements [67].

STM acquired topographies allowed us to characterize the surface structure on the nanoscale. The topographic image in Fig. 3.3c shows atomically flat terraces of typical ∼10 nm extent on the cleaved surface of SmB_6. These terraces are separated by steps of height equal to the cubic lattice constant $a_0 = 4.13$ Å, which identifies the cleaved surface as the (001) plane, in agreement with EBSD experiments. Figures 3.4a-d show higher resolution topographies of the four distinct

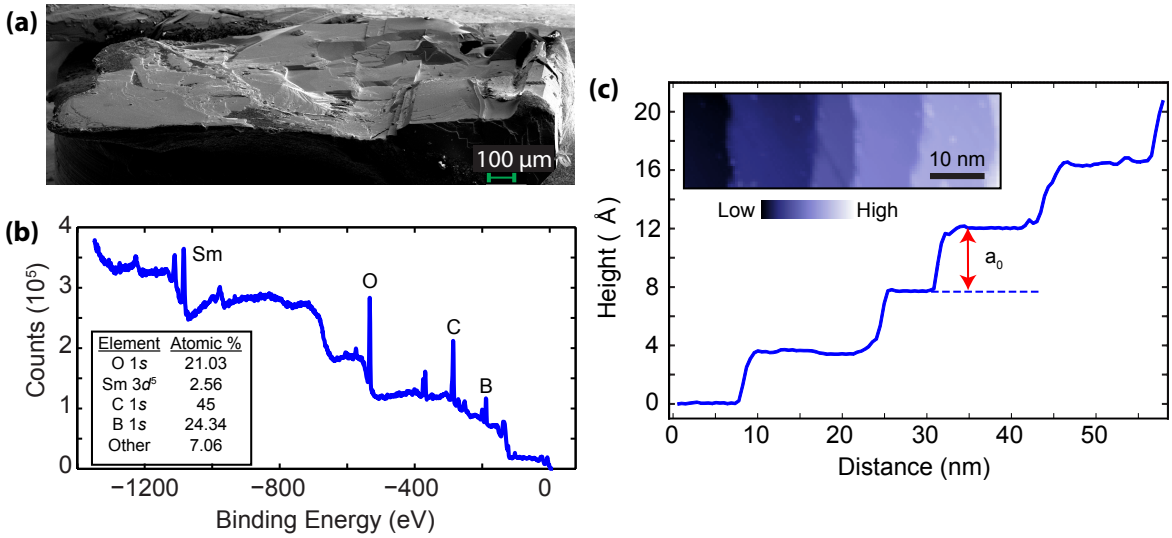

Figure 3.3: Surface characterization of SmB_6. **(a)** Scanning electron microscope (SEM) image of one of the SmB_6 crystals studied. All four nanoscale morphologies were observed on this cleaved surface. **(b)** X-ray photoemission spectroscopy (XPS) spectrum of the surface shown in (a). Annotated peaks correspond to the binding energies of the respective atoms. Inset: Atomic composition extracted from the XPS spectrum. The surface ratio of Sm:B is 1:9.5. **(c)** Topographic linecut across five atomically flat terraces. The difference in the vertical height between adjacent terraces is a_0. Inset shows a 50 nm $\times$ 15 nm topography of these terraces. ($T = 7$ K; setpoint voltage $V_s = -100$ mV; junction resistance $R_J = 10$ GΩ.) (a) and (b) were acquired after STM experiments were completed and the crystal was removed from the cryostat.

surface morphologies we observed. Figure 3.4a shows a rarely observed 1×1 square lattice, which we identify as a complete Sm layer, similar to the complete La layer of (001) cleaved LaB_6 previously imaged by STM [68]. Because the Sm atoms have a valence of $\sim$2+, this polar surface may be energetically unfavorable [69], explaining its typical limitation to small regions approximately 10 nm $\times$ 10 nm on the cleaved surface. The polar instability of the 1×1 surface could be resolved by removing half of the Sm atoms from the topmost layer, consistent with the 2×1 striped surface in Fig. 3.4b (also shown on the terraces of Fig. 3.3b). This surface is consistent with LEED observations of a 2×1 reconstruction [52] and ARPES observations of band-folding [53, 54] on the cleaved SmB_6 surface. However, the majority of our observed surfaces are disordered and can be classified as filamentary or amorphous, shown in Figs. 3.4c-d, respectively. Both of these disordered surfaces show corrugations $\sim 10\times$ larger than the suspected Sm terminations in Figs. 3.4a-b. Furthermore, the terrace step heights between these disordered morphologies are non-rational multiples of a_0. We speculate that the commonly observed filament morphology could be a reconstruction of the B_6 octahedra, consistent with our XPS measurements showing a B-rich surface [67].

Having assigned chemical identities to these surface morphologies, we image their differential tunneling conductance dI/dV. The tunneling dI/dV is typically proportional to the local DOS [29] (although we will discuss later an additional interference contribution that can manifest in Kondo systems). Figs. 3.4e-h show spatially averaged spectra representative of each of the four surfaces, emphasizing some ubiquitous features, as well as dramatic differences between the morphologies. The dominant features common to all surfaces are the spectral minimum located near the Fermi energy, and the relative prominence of the peak on the filled state side, compared to the empty state side. Both observations are consistent with the bare DOS for a hybridized electron-like conduction band [70]. Furthermore, we conducted dI/dV spectroscopic maps, as shown in Fig. 3.5. The dI/dV maps of Figs. 3.5e-h and spectra in Fig. 3.5i-l show that the two disordered filamentary and web surfaces are extremely inhomogeneous, as opposed to the homogeneity on the ordered Sm surfaces. The spectroscopic maps therefore provide further evidence supporting our chemical identification of the surface morphologies.

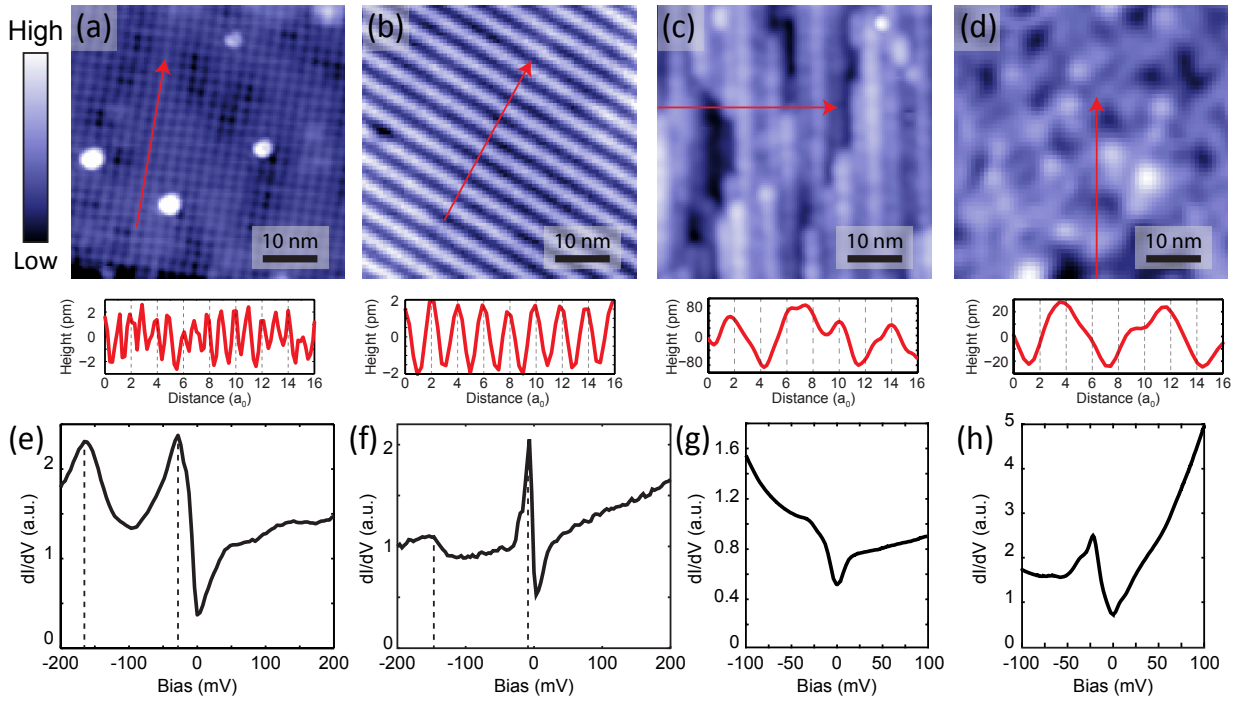

Figure 3.4: Surface morphology of SmB_6 and representative dI/dV. (**a-d**) Representative 10 nm $\times$ 10 nm topographic images of the four different surface morphologies, with linecuts along the red arrows showing the surface corrugation beneath each image. (**a**) 1×1 Sm termination. ($T = 9.5$ K, $V_s = -200$ mV, $R_J = 10$ GΩ.) (**b**) 2×1 half-Sm termination. ($T = 8.5$ K, $V_s = -100$ mV, $R_J = 5$ GΩ.) (**c**) Disordered filamentary B termination. ($T = 5.5$ K, $V_s = +200$ mV, $R_J = 20$ GΩ.) (**d**) Disordered web termination. ($T = 9$ K, $V_s = -100$ mV, $R_J = 2$ GΩ.) (**e-h**) Spatially averaged dI/dV representative of each of the four surface morphologies shown in **a-d**. (**e**) dI/dV on the 1×1 surface. Dashed lines indicate peaks at -165 mV and -28 mV. ($T = 9$ K, $V_s = -250$ mV, $R_J = 2$ GΩ, bias excitation amplitude $V_{\text{rms}} = 2.8$ mV.) (**f**) dI/dV on the 2×1 surface. Dashed lines indicate peaks at -155 mV and -8 mV. ($T = 8$ K, $V_s = 200$ mV, $R_J = 1$ GΩ, $V_{\text{rms}} = 1.4$ mV.) (**g**) Average dI/dV on the disordered filamentary surface. Spectra are very inhomogeneous (see Fig. 3.5). ($T = 7$ K, $V_s = -150$ mV, $R_J = 3$ GΩ, $V_{\text{rms}} = 3.5$ mV.) (**h**) Average dI/dV on the disordered web surface. Spectra are very inhomogeneous (see Fig. 3.5), with an average peak at -22 mV. ($T = 9$ K, $V_s = -100$ mV, $R_J = 2$ GΩ, $V_{\text{rms}} = 2.8$ mV.)

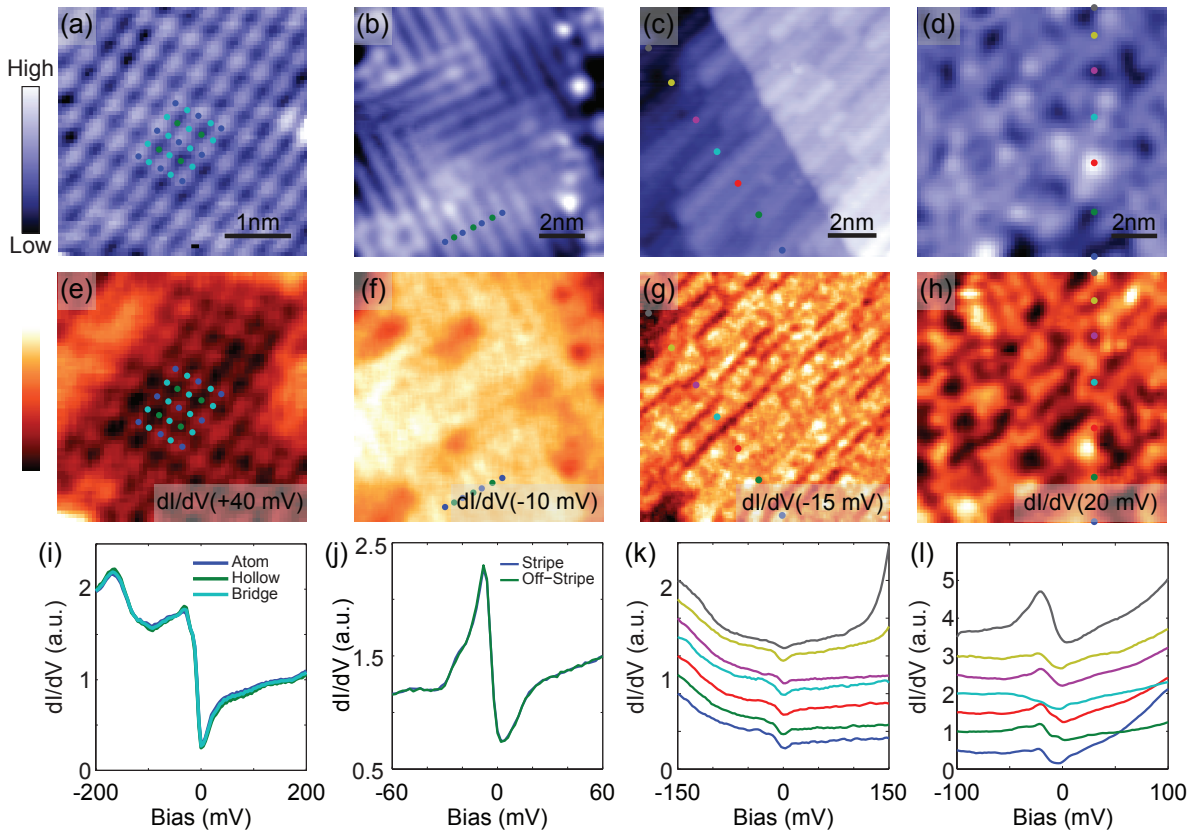

Figure 3.5: Spatial dependence of differential tunneling conductance. (**a**-**d**) Topographies on four different surface morphologies. (**e**-**h**) dI/dV maps at constant bias (indicated in figure), each acquired simultaneously with the respective topography shown in (a-d). (**i**-**l**) Representative dI/dV spectral variation within each of the four morphologies. (**a**, **e**, **i**) The 1×1 Sm-terminated region shows weak spectral inhomogeneity. ($T = 9.5$ K, $V_s = -200$ mV, $R_J = 2$ GΩ, $V_{\text{rms}} = 2.8$ mV.) Spectra on the atoms (blue), on the hollow sites (green) and on the bridge sites (teal) the atoms are identical. (**b**, **f**, **j**) The 2×1 Sm-terminated region shows spectral homogeneity on (blue) and off (green) the stripes. ($T = 4.4$ K, $V_s = -100$ mV, $R_J = 2$ GΩ, $V_{\text{rms}} = 2.1$ mV.) (**c**, **g**, **k**) The filamentary B-terminated region is spectrally inhomogeneous. ($T = 7$ K, $V_s = -150$ mV, $R_J = 3$ GΩ, $V_{\text{rms}} = 3.5$ mV.) (**d**, **h**, **l**) The disordered web region shows extreme spectral inhomogeneity. ($T = 9$ K, $V_s = -100$ mV, $R_J = 2$ GΩ, $V_{\text{rms}} = 2.8$ mV.)

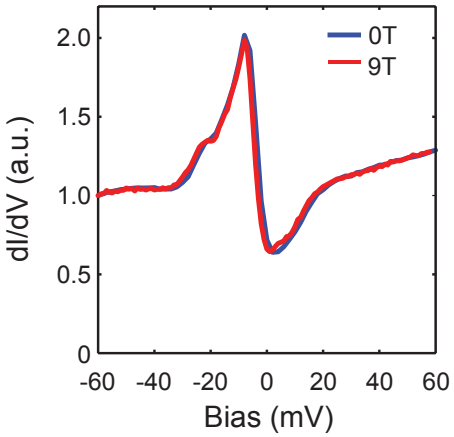

Figure 3.6: Magnetic field dependence of dI/dV spectra. Spectra acquired in zero field (blue) and 9 T (red) are plotted. The data have been scaled by a multiplicative constant but not offset. Magnetic field was applied along the c-axis. ($B = 0$ T: $T = 4.4$ K, $V_s = -100$ mV, $R_J = 2$ GΩ, $V_{\rm rms} = 2.1$ mV; $B = 9$ T: $T = 2.2$ K, $V_s = -60$ mV, $R_J = 1.2$ GΩ, $V_{\rm rms} = 1.4$ mV)

To better understand the f band hybridization, we focus in more depth on the two Sm-terminated surfaces. Spectra on the 1×1 surface show a peak at -165 mV (Fig. 3.4e), which we identify as the hybridized Sm^{2+} $^6H_{7/2}$ multiplet typically seen by ARPES at E_B ∼150-160 mV [54–56, 66], and a peak at -28 mV, which we identify as the hybridized $^6H_{5/2}$ multiplet typically seen by ARPES at E_B ∼14-20 meV [52–56, 66]. The downward energy shift of both these STM-observed $^6H_{7/2}$ and $^6H_{5/2}$ multiplets compared to the average ARPES observations could arise from the polar catastrophe at the 1×1 surface [71]. The polar catastrophe would cause the movement of electrons towards the surface to decrease the charge of the surface Sm layer, and would shift the Fermi level up, causing the hybridized f bands to appear lower in comparison. Indeed, one ARPES experiment [57] that boasted no evidence of surface reconstruction from LEED [52] or band-folding [53, 54], showed similarly higher binding energies of -170 mV and -40 mV, consistent with a chemical potential shift at a polar 1×1 surface.

We expect that the 2×1 surface is nonpolar, and may provide a better view of the bulk f bands and hybridization process. Spectra on the 2×1 surface at low T show a broad peak at around -155 mV, and a remarkably sharp feature centered at -8 mV (Fig. 3.4f), both more consistent with $^6H_{7/2}$ and $^6H_{5/2}$ multiplet energies observed by ARPES [52–56, 66]. The -8 mV peak is

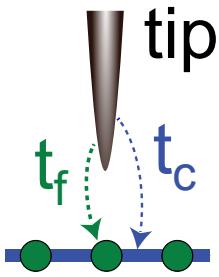

Figure 3.7: Illustration of cotunneling process in Kondo systems. In a Kondo system, electrons can tunnel into the conduction band (blue) or the f band (green). The tunneling amplitude into the conduction or f band is t_c, and t_f, respectively.

extremely homogeneous on clean terraces of varying sizes (Fig. 3.5b,f,j), and shows no change in a c-axis magnetic field up to 9 T (see Fig. 3.6), unlike the 'in-gap' state whose field-suppression was observed by NMR [72]. Some ARPES experiments have also observed a weakly dispersing state around -8 mV to -4 mV, which has been claimed as the 'in-gap' signature of a TKI [52, 56]. However, a topological 'in-gap' state should continuously span the full hybridization gap, so we argue that the sharp -8 mV state is the manifestation of the $4f$-$5d$ hybridization itself, observed specifically on the 2×1 surface.

3.4 Tunneling into a Kondo Lattice

In typical STM/STS experiments, the measured differential conductance dI/dV is representative of the sample density of states (DOS) [29]. However, in Kondo systems there are two independent tunneling paths: one into the conduction band and another into the heavy band. Therefore the tunneling dI/dV depends on the DOS of the conduction band, the DOS of the heavy band, *and the interference of these two tunneling paths.* This cotunneling process is illustrated in Fig. 3.7. It is necessary to account for the cotunneling process in order to extract the quantity of interest, the intrinsic DOS of the hybridized bands, from the dI/dV spectra.

In this section we will discuss three models that we used to simulate our experimental spectra: a Fano model [73, 74] as well as two clean Kondo lattice models by Figgins *et al* [70] and Maltseva *et al* [75]. While the Fano model fails to fit the SmB_6 spectra on our clean 2×1 surfaces,

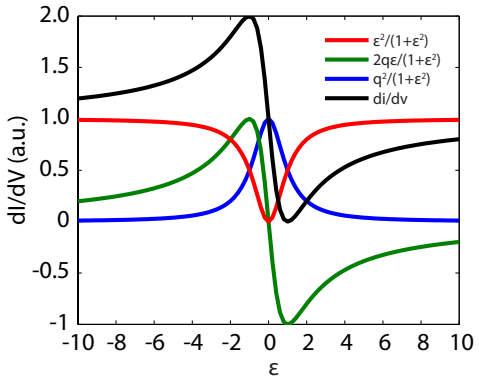

Figure 3.8: Decomposition of the Fano lineshape according to Eqn. 3.2. The three components and the resultant summed dI/dV are indicated in the legend. Spectrum was plotted for $q = -1$, $A = 1$ and ϵ is plotted in units of w for $E_0^f = 0$.

both Kondo lattice models capture the main qualitative features of our spectra: the peak location, width, and sharpness, as well as the width and positive energy kink of the gap. By using the clean Kondo lattice model of Figgins *et al.* [70] to separate the three components of the STM-measured dI/dV on SmB_6, we show that dI/dV is dominated by the bare DOS, in contrast to earlier PTS/PCS measurements [50, 63].

3.4.1 Kondo impurity Fano model

It is well known that tunneling into a Kondo impurity – a single magnetic atom in a non-magnetic host – reflects the intrinsic impurity level and conduction band, *as well as* the quantum mechanical interference between those two tunneling channels. The interference manifests as a Fano resonance – an asymmetric dip-peak feature that dominates the tunneling signal [34, 76]. The Fano lineshape has the form,

$$\frac{dI}{dV}(V) = A \cdot \frac{(q+\epsilon)^2}{1+\epsilon^2} \tag{3.1}$$

where A is a multiplicative prefactor, q is the Fano parameter, $\epsilon = (eV - E_0^f)/w$, E_0^f is the energy of the discrete f state, and w is the width of the resonance, roughly equal to the single ion Kondo temperature [75]. It is instructive to decompose the Fano lineshape by expanding Eqn.

3.1,

$$\frac{dI}{dV}(V) = A\left[q^2\frac{1}{1+\epsilon^2} + 2q\frac{\epsilon}{1+\epsilon^2} + \frac{\epsilon^2}{1+\epsilon^2}\right] \tag{3.2}$$

The three terms in Eqn. 3.2 are plotted separately in Fig. 3.8. The first term in Eqn. 3.2, shown using the blue curve in Fig. 3.8, has the form of a Lorentzian scaled by the square of the Fano parameter and can be attributed to the DOS from the f band. The third term in Eqn. 3.2, shown using the red curve in Fig. 3.8, asymptotes to 1 for $\epsilon >> 1$, vanishes when $\epsilon \to 0$, and can be thought of as the gapped DOS of the itinerant electrons. Meanwhile, the second term in Eqn. 3.2, shown using green in Fig. 3.8, bears particular consideration. The term $\epsilon/(1+\epsilon^2)$ switches sign when $\epsilon = 0$, implying that the contribution from this term will be *negative* on one side of $\epsilon = 0$. This clearly cannot be thought of as a DOS contribution, as negative DOS is unphysical. This term is therefore the manifestation of the interference of the cotunneling process, and represents destructive and constructive interference of the conduction and f tunneling paths. Having assigned each term to different tunneling processes, we can rewrite Eqn. 3.2 as:

$$\frac{dI}{dV}(V) = A\left[q^2\tilde{N}_f + 2q\tilde{N}_{cf} + \tilde{N}_c\right] \tag{3.3}$$

where $\tilde{N}_f = 1/(1+\epsilon^2)$ represents tunneling into the f band, $\tilde{N}_{cf} = \epsilon/(1+\epsilon^2)$ represents the interference, and $\tilde{N}_c = \epsilon^2/(1+\epsilon^2)$ represents tunneling into the conduction band. The Fano parameter q in Equation 3.3 can now be interpreted as being proportional to the probability of tunneling into the f band. This interpretation has a direct analog to the more precise model for tunneling into a Kondo lattice, which we discuss in following section.

While the Fano lineshape has successfully described the dI/dV conductance of dilute magnetic atoms on a metal substrate [34, 76], multiple experimental papers have reported that tunneling into a Kondo lattice requires a more complicated model to incorporate the effect of the heavy bands [50, 77, 78]. Recent theoretical work suggested that the Fano lineshape is just a limiting case in Kondo lattice systems with spatial inhomogeneity or large self-energy [74]. We found that for our dI/dV spectra, the Fano lineshape did not match the key features our spectra. Fig. 3.9

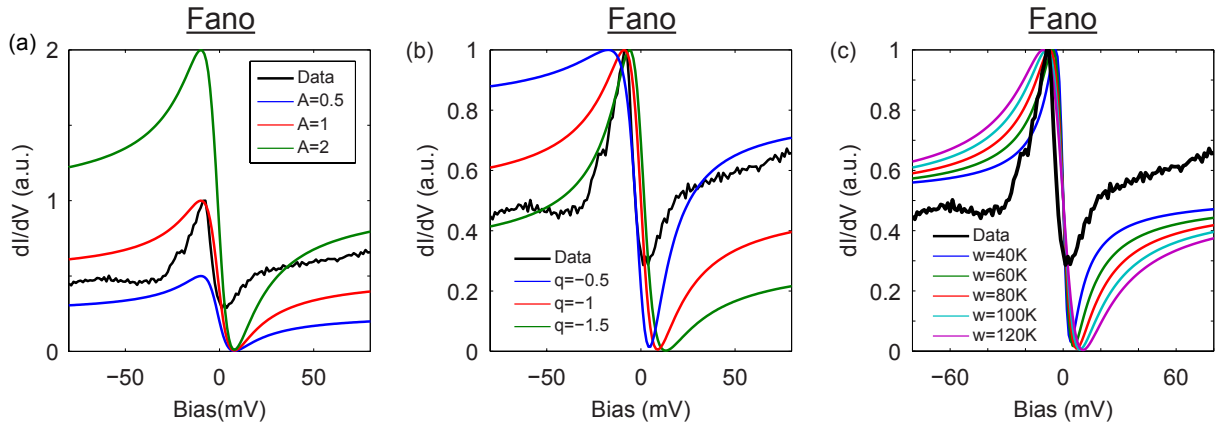

Figure 3.9: Attempt to fit the 2×1 surface dI/dV spectrum to the Fano model. (**a**) We fixed $q = -1$, $E_0^f = 0$, and $w = 100$ K (the single ion Kondo temperature [50, 75, 79]), while varying the amplitude A. (**b**) We fixed $A = 1$, $E_0^f = 0$, and $w = 100$ K, while varying the Fano parameter q. (**c**) We fixed $A = 1$, $E_0^f = 0$, and $q = -1$, while varying w. In each case, we thermally broadened all Fano model spectra to the measurement temperature of 8 K. Black trace shows measured dI/dV on the 2×1 surface, acquired at $T = 8$ K, $V_s = -100$ mV, $I_s = 100$ pA, $V_{\text{rms}} = 1.4$ mV. The measured dI/dV was scaled by a single multiplicative constant, but not offset.

shows the experimental data superposed on top of the Fano spectrum at different parameters. We note that no combination of A, q and w in the Fano model could simultaneously reproduce the positive bias kink and the width of the -8 mV peak in the measured dI/dV. This necessitates the use of Kondo lattice models which we discuss in the following section.

3.4.2 Kondo lattice models

Figgins model

We used two different Kondo lattice models [70, 75] to better understand our dI/dV spectra. We first discuss the cotunneling model of Figgins and Morr [70], in which dI/dV can be decomposed as the sum of three terms from the conduction band, the f band, and the interference of the two channels. The differential tunneling conductance is modelled as:

$$\frac{dI}{dV}(V) = \left(\frac{t_f}{t_c}\right)^2 N_f(V) + 2\left(\frac{t_f}{t_c}\right) N_{cf}(V) + N_c(V) \tag{3.4}$$

where $N_c(V)$ and $N_f(V)$ represent the bare DOS, t_c and t_f are the respective tunneling amplitudes into the two respective bands, and $N_{cf}(V)$ represents the quantum mechanical interference between the two tunneling channels [70, 74, 80, 81]. t_f and t_c are extrinsic parameters that are influenced by the tunnel junction and other experimental parameters. However, N_c, N_f, N_{cf} are all intrinsic to the Kondo lattice system being studied and take the form [70]:

$$N_c = \mathrm{Im}[G_c(k,\omega)] \tag{3.5}$$

$$N_f = \mathrm{Im}[G_f(k,\omega)] \tag{3.6}$$

$$N_{cf} = \mathrm{Im}[G_{cf}(k,\omega)] \tag{3.7}$$

and the hybridized Green's functions are given by

$$G_c(k,\omega) = \left[G_c^0(k,\omega)^{-1} - v^2 G_f^0(k,\omega)\right]^{-1} \tag{3.8}$$

$$G_f(k,\omega) = \left[G_f^0(k,\omega)^{-1} - v^2 G_c^0(k,\omega)\right]^{-1} \tag{3.9}$$

$$G_{cf}(k,\omega) = G_c^0(k,\omega) v G_f(k,\omega) \tag{3.10}$$

The hybridized Green's functions are expressed in terms of the hybridization amplitude v and the bare Green's functions: $G_c^0(k,\omega) = [\omega + i\gamma - E_k^c]^{-1}$ and $G_f^0(k,\omega) = [\omega + i\gamma - E_k^f]^{-1}$ where γ is the self energy and E_k^c and E_k^f are the unhybridized band structures of the conduction and f band, respectively. The hybridized bands take the form

$$E_k^{\pm} = \frac{1}{2}\left(E_k^c + E_k^f\right) \pm \sqrt{\frac{1}{4}\left(E_k^c - E_k^f\right)^2 + v^2}. \tag{3.11}$$

The hybridized bands with realistic parameters are plotted in Figure 3.10.

It is instructive to compare the form of dI/dV from the Figgins model (Eqn. 3.4) with the decomposed dI/dV from the Fano model (Eqn. 3.3). In Eqn. 3.3, q is a prefactor for the f-band term and the interference term, and has the same form and meaning as the prefactor t_f/t_c in Eqn. 3.4, which scales the tunneling into the f-band. Therefore if we associate the tunneling ra-

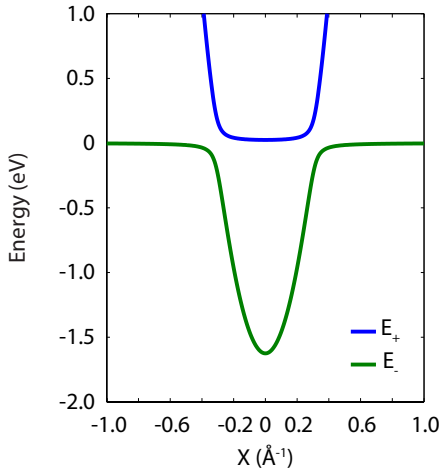

Figure 3.10: Hybridized band structure according to Eqn. 3.11. Blue and green are the positive and negative branches of the band structure respectively. Parameters were chosen to realistically reflect the model used and described in the text. E_k^c was modeled as a parabolic band centered at the X point ($k = 0$ in this figure) with crossings at $k = 0.401$ (π/a_0), $E_k^f = 0$ with no dispersion, and $v = 0.2$ eV.

tio with the Fano parameter: $t_f/t_c \Leftrightarrow q$, then we can similarly associate the respective terms for the different tunneling processes from Eqn. 3.3 with Eqn. 3.4: $\tilde{N}_{c,f,cf} \Leftrightarrow N_{c,f,cf}$. The Fano model can therefore be considered as a coarse Kondo lattice model, which retains the overall structure of the Kondo lattice model but without some finer details. As one example, by using a Kondo lattice model we can incorporate the known band structure into the Greens functions and DOS of the c and f bands through Eqns. 3.8 to 3.10, which is not possible using the Fano model. In fact, recent theoretical papers have shown that the dI/dV of a Kondo lattice has a Fano lineshape in the high disorder limit [74] or the high γ limit [75], further supporting the interpretation of the Fano model as a limiting case of general Kondo lattice models.

In our model, the bare bands of the conduction and f band were constrained by experiment and theory. We modelled the Sm $5d$ conduction band as an ellipsoid centered at the X point of the three-dimensional Brillouin zone, with semi-major k_F axes $0.401(\pi/a_0) \times 0.401(\pi/a_0) \times 0.600(\pi/a_0)$ and $E_{\min} = -1.6$ eV in agreement with ARPES measurements [54]. We modeled the Sm $4f$ band as a non-dispersive flat band spanning the Brillouin zone at energy E_0^f, and used a self-energy $\gamma = k_B T$ for the measurement temperature $T = 8$ K. The bands were sim-

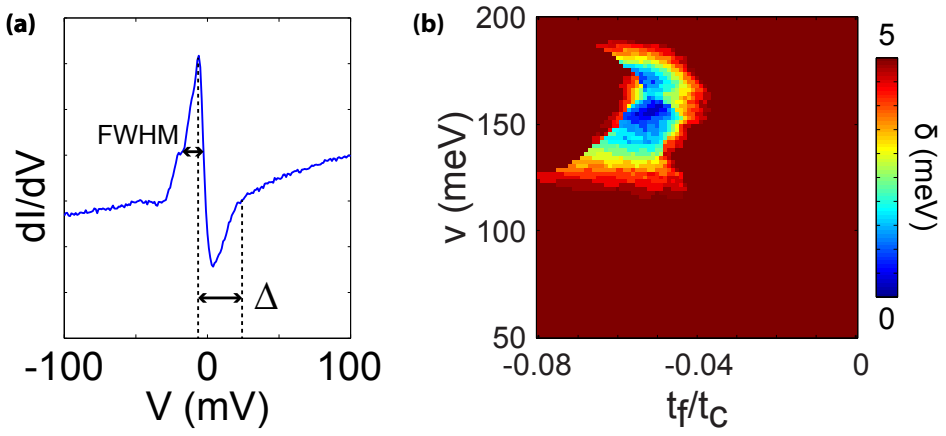

Figure 3.11: Fitting metric for the Figgins model. **(a)** Experimental 8K spectrum with annotations indicating the FWHM and the $\Delta = |V_p - V_k|$ used for calculating the error metric. **(b)** Error metric δ in units of meV in $(v, t_f/t_c)$ phase space for $T = 8$ K spectrum on the 2×1 surface. Bands were calculated as described in the text for $\gamma = 8$ K.

ulated numerically in IDL using a typical k mesh of 201 points across 1/8 of the Brillouin zone, with an energy mesh ~ 10 mV. To obtain the best match to our experimental spectra, we varied E_0^f, t_f/t_c, and v to match the data. The best match was obtained by finding the simulated curve that minimized the error metric δ (in units of meV) in $(v, t_f/t_c)$ phase space for $T = 8$ K spectrum on the 2×1 surface. The error metric is $\delta(v, t_f/t_c) = \sqrt{\delta\text{FWHM}^2 + \delta\Delta^2}$, where δFWHM is the difference between the experimental and theoretical FWHM of the negative bias peak, and $\delta\Delta$ is the difference between the experimental and theoretical values of $|V_{\text{peak}} - V_{\text{kink}}|$. Figure 3.11a denotes the FWHM and the Δ of the experimental $T = 8$ K spectrum and in Fig. 3.11b we show the result of calculating δ across all of phase space. The two fitting metrics, FWHM and Δ, were chosen because they represent the most relevant spectroscopic quantities in the dI/dV curves. The best match was chosen by calculating the error metric δ numerically in Matlab across all of phase space. Fig. 3.12 shows a modeled spectra that agrees well with our experimental spectra acquired on the 2×1 surface, and represents the minimized error in phase space (Fig. 3.11b). We found a good match using $E_0^f = -3.5$ meV, $v = 155$ meV, and $t_f/t_c = -0.055$. In particular, we note that there exists a large negative bias peak, a dip at the Fermi level, and a positive bias kink, all in agreement with the 2×1 spectra shown in Fig. 3.4f, 3.11a.

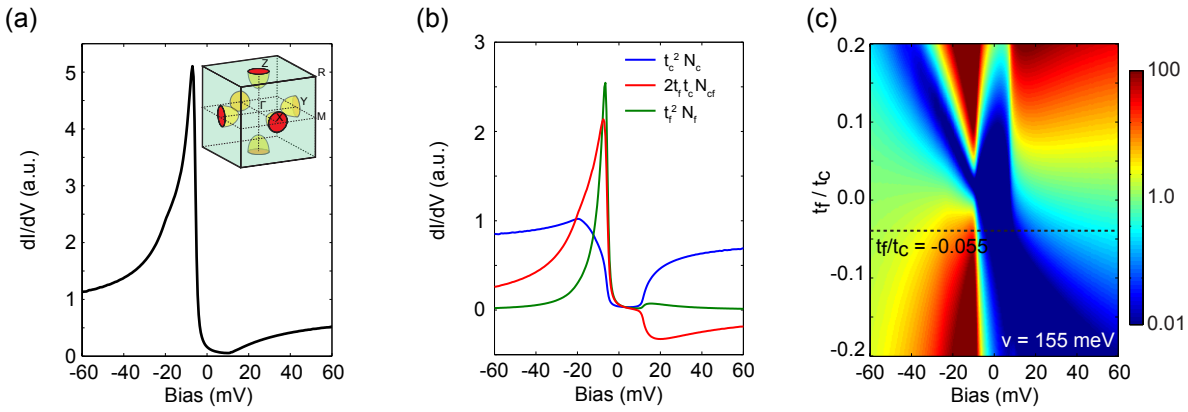

Figure 3.12: Decomposition of the measured tunneling conductance into DOS and interference channels. (**a**) Simulation of dI/dV on the 2×1 surface using a two-channel tunneling model [70]. The conduction band was modeled as an ellipsoid centered at the X point in the three-dimensional Brillouin zone shown in the inset, and the hybridized f band was approximated as dispersionless. The main features of the 2×1 spectra are well-matched for self energies $\gamma_c = \gamma_f = 0.7$ meV (equivalent to $k_B T$ at the measurement temperature $T = 8$ K), hybridized f band energy $E_0^f = -3.5$ meV, hybridization amplitude $v = 155$ meV, and tunneling ratio $t_f/t_c = -0.055$. (**b**) Scaled contributions to dI/dV from the conduction band (blue), f band (green), and interference (red). (**c**) Simulated dI/dV as a function of t_f/t_c with the other parameters identical to **a**. The dominant peak position and shape evolve dramatically with t_f/t_c; the dashed horizontal line indicates the best match to our data.

Maltseva Model

In addition to the model of Figgins and Morr [70], the model of Maltseva, Dzero and Coleman [75] has been used extensively in other HF systems [50, 77] as an analytical formula for modelling the dI/dV spectra of Kondo lattices. Previous experimental work has attempted to fit experimental dI/dV spectra to the formalism of Maltseva to extract parameters such as the bandwidth, hybridization amplitude and even the temperature dependence of these parameters [50, 77]. However, we point out a crucial error in the analysis in Refs. [50, 77] which we have corrected, and use our results to qualitatively show the equivalence between the model of Figgins and Morr [70], and Maltseva *et al.* [75].

The Maltseva model is an analytical mean-field approximation to the dI/dV of a Kondo lattice. Rather than expressing dI/dV in terms of the Greens functions of the bare bands as in Ref. [70] (see Eqns. 3.8 - 3.10), the Maltseva model presumes that the system has a parabolic conduction band and a non-dispersive heavy band that overlap in energy and k. dI/dV then

takes the form:

$$\frac{dI}{dV}(V) \propto \mathrm{Im}\left[G^{KL}(eV - i\gamma)\right] \tag{3.12}$$

$$G^{KL}(eV) = \left(1 + \frac{v}{eV - E_0^f}\frac{t_f}{t_c}\right)^2 \ln\left[\frac{eV + D_1 - \frac{v^2}{eV - E_0^f}}{eV - D_2 - \frac{v^2}{eV - E_0^f}}\right] + \frac{D_1 + D_2}{eV - E_0^f}\left(\frac{t_f}{t_c}\right)^2 \tag{3.13}$$

where $-D_1$ and D_2 are the lower and upper conduction band edges, v is the hybridization amplitude, t_f/t_c is the ratio of the tunneling amplitudes, E_0^f is the energy of the non-dispersive f band, and γ is the self-energy. In Eqn. 3.13 we have corrected a typo in the original Ref. [75], which propagated into Ref. [50, 77]. The t_f^2 factor in the second term of the Green's function was originally omitted in Ref. [75], but is necessary to correctly dimensionalize the equation; its absence leads to an unphysical negative dI/dV in a subset of parameter space. Correspondingly the absence of the t_f^2 factor leads to unphysically small values of the conduction bandwidth $D = 30$ meV for SmB_6 reported in Ref. [50]. Instead, we used $D_1 = 1.6$ eV in agreement with ARPES [54], and approximated $D_2 = 3$ eV in agreement with LDA calculations [82], giving a total conduction bandwidth of $2D = D_1 + D_2 = 4.6$ eV in better agreement with ARPES measurements [54, 55, 64]. We used $\gamma = k_B T$ for the measurement temperature $T = 8$ K and varied E_0^f, t_f/t_c, and v to match the 2×1 data.

Figure 3.13a plots simulated dI/dV curves at different values of v using the Maltseva model. We note the prominence again of three features: (1) a negative bias peak, (2) a positive bias kink, and (3) a broad Fermi level gap in the simulated curves. This is in agreement with the dI/dV from our data, and the simulated dI/dV using the Figgins model (plotted in Fig. 3.13b). In Fig. 3.13 we have plotted both Maltseva (a) and Figgins (b) at identical values of v, t_f/t_c, γ, E_0^f for comparison. We find that for the best-fit parameters of the Figgins model in Fig. 3.11, the Maltseva model agrees well with Figgins, and with the data. Furthermore, the value of v that we use here is consistent with the Maltseva predicted magnitude of the hybridization gap $\Delta \sim 2v^2/D$ [75].

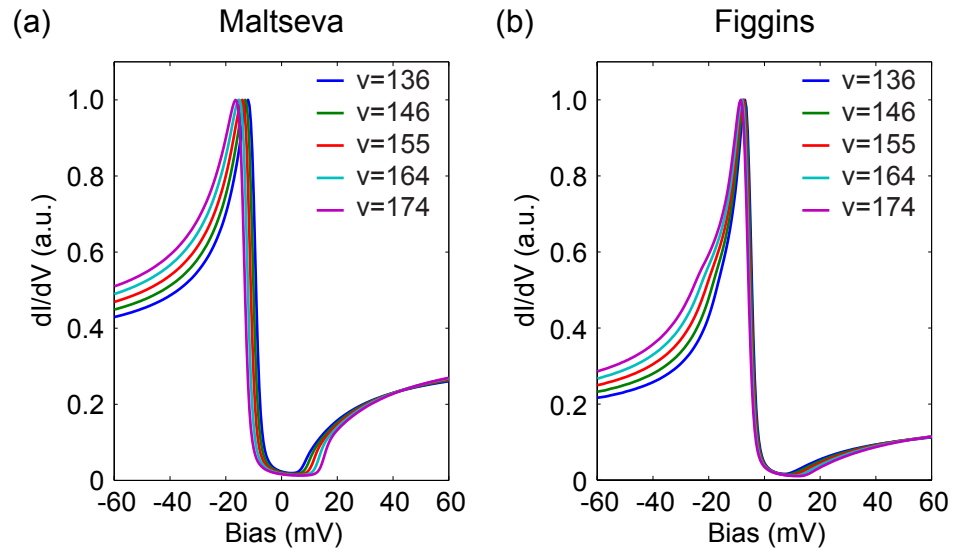

Figure 3.13: Computed spectra using the Maltseva model (a) and the Figgins model (b). For both models, we varied the hybridization amplitude v (legend in units of meV), with fixed $t_f/t_c = -0.055$, $E_0^f = -3.5$ meV, and self-energy $\gamma = k_BT$ for the measurement temperature $T = 8$ K. For (a), as described in the text, we used $D_1 = 1.6$ eV and $D_2 = 3$ eV. For (b), as described in the text, we modeled the Sm $5d$ conduction band as an ellipsoid centered at the X point of the three-dimensional Brillouin zone, with semi-major k_F axes $0.401(\pi/a_0) \times 0.401(\pi/a_0) \times 0.600(\pi/a_0)$ and $E_{\min} = -1.6$ eV.

Discussion

We summarize the simulation of the 2×1 surface dI/dV spectra using the Fano, Figgins and Maltseva models in Fig. 3.14, in which the calculated dI/dV is plotted as a function of bias and tunneling ratio (Fano parameter). All models agree on the following three main features: (1) the relative prominence of a negative energy peak for $t_f/t_c < 0$; (2) the emergence of a positive energy peak for $t_f/t_c > 0$; (3) the persistence of a deep gap ($< 10\%$ of the background dI/dV) near the Fermi level across a wide range of t_f/t_c. However, the Fano model fails to capture some subtleties of the full Kondo lattice models [50] which are seen in the data, such as the abrupt kink on the positive edge of the gap, and the shoulder on the negative side of the peak.

By decomposing the spectra into the three tunneling channels, we can isolate the interference term which is an extrinsic contribution to our dI/dV measurement, and is undesirable because it masks the desired bare DOS signal. Furthermore, using the Morr model of Eqn. 3.4 allows us to

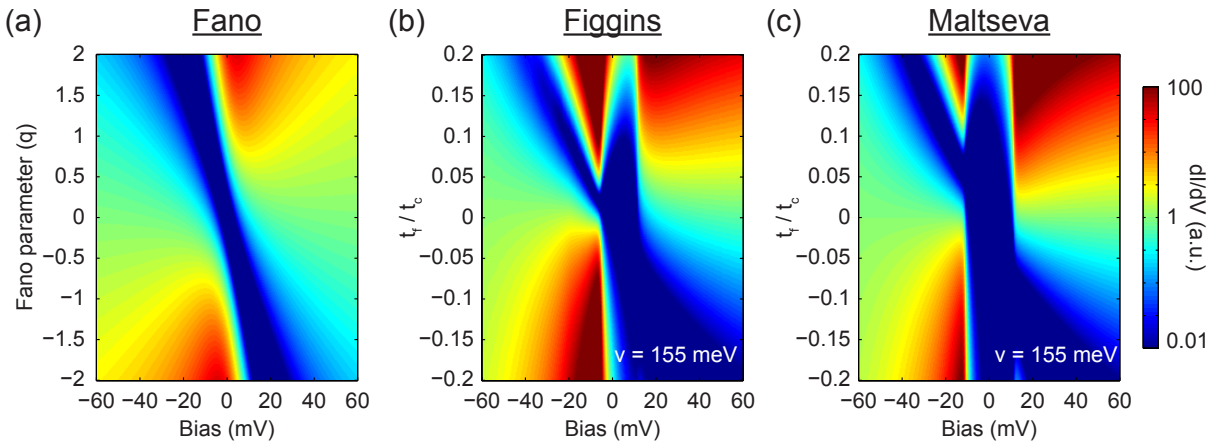

Figure 3.14: Comparison of Fano, Figgins and Maltseva dI/dV models. (**a**) dI/dV calculated using the Fano lineshape with $w = 100$ K and $E_0^f = -3.5$ meV as a function of bias and Fano parameter q. (**b**) dI/dV calculated using the Figgins and Morr model with $v = 155$ meV, $E_0^f = -3.5$ meV, and $\gamma = k_B T$ corresponding to the measurement temperature of 8 K. (**c**) dI/dV calculated using the model of Maltseva, Dzero and Coleman with $v = 155$ meV, $E_0^f = -3.5$ meV, and $\gamma = k_B T$ corresponding to the measurement temperature of 8 K.

take a step beyond recent PCS results [50] by separately plotting the scaled components $N_c(V)$, $2(t_f/t_c)N_{cf}(V)$, and $(t_f/t_c)^2 N_f(V)$ in Fig. 3.12b. This allows us to examine the bare DOS in the N_c and N_f channels. From the decomposition of the 2×1 spectra, we find that there always exists a negative energy peak (V_p) and positive energy kink (V_k) in the N_f channel due to hybridization, and that the energy separation between these features, $\Delta(N_f) = |V_p - V_k|$, is the hybridization gap (Δ_{hyb}). Figure 3.15 illustrates these energy scales. Furthermore, for $t_f/t_c < 0$, the energies V_p and V_k for N_f occur at the same energies as V_p and V_k in the summed dI/dV channel. Therefore measuring the energy separation, $\Delta(dI/dV) = |V_p - V_k|$, in dI/dV is equivalent to measuring the gap in the f-band DOS: $\Delta(dI/dV) = \Delta(N_f) = \Delta_{\text{hyb}}$.

Using this information, we quantify the hybridization gap directly from our dI/dV spectrum: $\Delta = 26 \pm 2$ meV at $T = 8$ K. This measurement is in the middle of the range of hybridization gap measurements reported in the literature, and summarized in Tab. 3.1. In particular, this is consistent with a recent high resolution ARPES measurement which used thermal population of positive energy states to measure the hybridization gap at higher T [64]. We elaborate more on this extraction of the hybridization gap in Section 3.5.

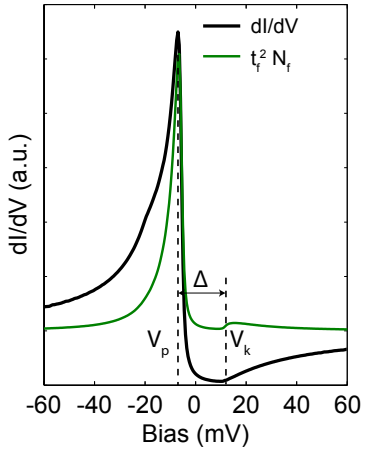

Figure 3.15: Measurement of Δ from dI/dV. Superposed and offset N_f and dI/dV curves from Fig. 3.12. Curves have been offset for visual clarity. The dashed lines indicate the peak V_p and kink V_k energies of the N_f and dI/dV curves. The energy separation between these two features is the gap measurement Δ.

3.4.3 Kondo lattice model on the 1×1 surface

On the 1×1 terminated surface (spectrum shown in Fig. 3.4e) using the the model of Figgins and Morr we found good agreement to the dI/dV peak at -28 mV by using $v = 273$ meV, $\gamma = 8$ K, $t_f/t_c = -0.05$, and $E_0^f = -16$ meV. The results of this analysis are shown in Fig. 3.16. We note that the extracted value for $E_0^f = -16$ mV on the 1×1 surface is lower than the $E_0^f = -3.5$ mV on the 2×1 surface, in good agreement with our observation of polarity driven surface band bending. Furthermore, the fact that the hybridization amplitude on the 1×1 is larger than on the 2×1 surface ($v_{1\times1} = 273$ mV $> v_{2\times1} = 155$ mV) is consistent with our chemical identification of the surfaces. We would expect that the hybridization is stronger on the 1×1 surface owing to the higher concentration of Sm atoms, compared to the half terminated 2×1 surface.

3.5 Spectroscopy of the temperature dependent Kondo transition

Because the hybridization manifests as a metal insulator transition at $T^* \sim 50$ K as shown in Fig. 3.2b, we performed temperature dependent dI/dV spectroscopy on the 2×1 surface to investigate the hybridization process. One of the sequences of T-dependent dI/dV spectra is shown

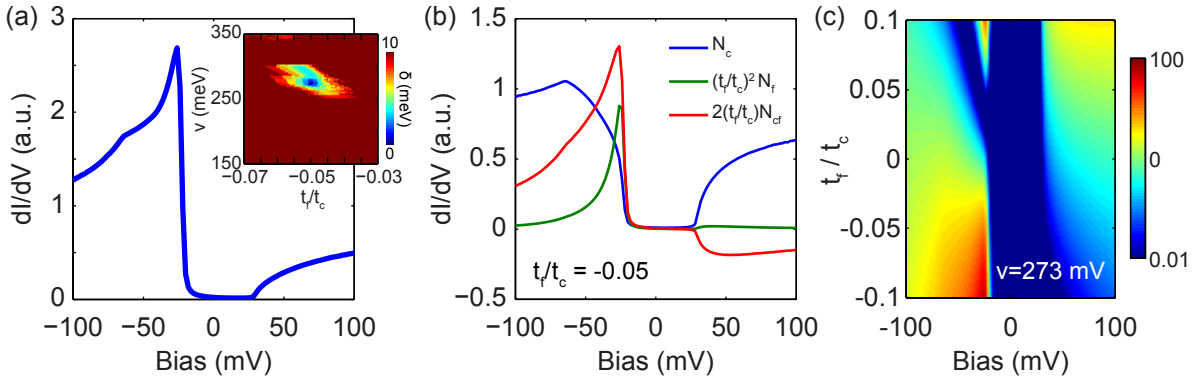

Figure 3.16: Components of dI/dV spectroscopy on the 1×1 surface. (**a**) dI/dV calculated using the the formalism of Figgins and Morr [70]. Model parameters are listed in the text: $v = 273$ meV, $t_f/t_c = -0.05$, $E_0^f = -16$ meV and γ corresponding to the measurement temperature of 8 K. We calculated spectra throughout $(v, t_f/t_c)$ phase space and chose the spectrum that matched best to the experimental 1×1 spectrum (Fig. 3.4e). The inset shows the minimization procedure in phase space. (**b**) dI/dV contributions from the conduction band (N_c, blue), f band (N_f, green), and interference (N_{cf}, red). (**c**) dI/dV calculated by varying t_f/t_c with fixed $v = 273$ meV, $E_0^f = -16$ and γ corresponding to the measurement temperature of 8 K.

in Fig. 3.17a. With the exception of T, all of the spectra shown in Fig. 3.17a were taken with the exact same experimental conditions over clean 2×1 regions. Between $T = 8$ K to $T = 50$ K, the T-dependent spectra show a substantial reduction in spectral weight of the peak-dip features from 8 K to 50 K, suggesting that these features reflect the Kondo hybridization of the itinerant and Sm $4f$ electrons. To better visualize the T-dependent effect on dI/dV, we normalize the spectra to remove any artifact variations from z piezo drift. The data is normalized by dividing the spectra by a third order polynomial background shown using a dashed overlay in Fig. 3.17b. The normalized spectra shown in Fig. 3.17c show two effects with increasing T: (1) The suppression of the Fermi level dip, and (2) the suppression of the negative bias peak. In fact we note that the Fermi level dip is nearly completely filled-in by $T = 50$ K.

3.5.1 The effect of thermal broadening

In addition to experimental artifacts, thermal broadening of dI/dV spectra will smear features in dI/dV and could cause the peak/dip suppression we observe in Fig. 3.17a-c. Therefore, to study

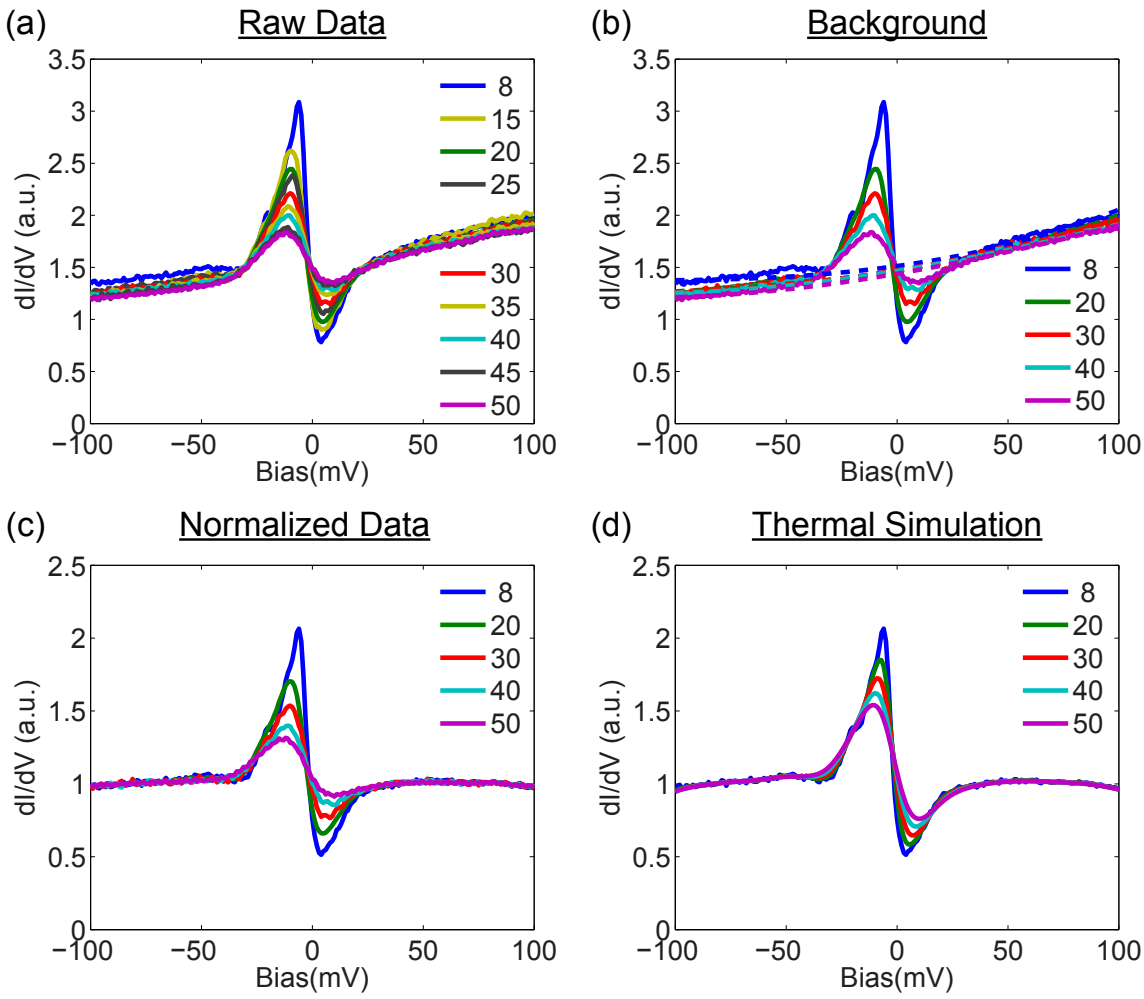

Figure 3.17: Temperature dependent dI/dV on 2×1 surface. (**a**) Raw STM dI/dV spectra, corresponding to the square markers in Fig. 3d of the main text. Temperature dependence (in Kelvin) is shown in the legend. ($V_s = 100$ mV, $R_J = 1$ GΩ, $V_{\text{rms}} = 1.4$ mV.) (**b**) Third order polynomial backgrounds (dashed lines) superimposed on some of the raw spectra shown in (a). (A representative subset was selected to avoid over-cluttering the image.) Each polynomial background was fit to the corresponding raw spectrum excluding the energy range -60 mV $< V <$ +20 mV. (**c**) Normalized spectra obtained by dividing each raw spectrum by its corresponding fitted polynomial background from (b). The maxima and minima of these normalized spectra are plotted as blue and green points, respectively, in Fig. 3.18. (**d**) Thermally broadened normalized spectra. The $T = 8$ K normalized spectrum from (c) was deconvolved to $T = 0$ K then thermally broadened to the simulated temperature indicated in the legend. Maxima and minima of this sequence of spectra are plotted as grey lines in Fig. 3.18. Comparing the corresponding spectra in (c) and (d) shows that the rate of temperature evolution of the data exceeds that expected from thermal broadening alone.

the intrinsic temperature dependence of the dI/dV spectra we need to account for the thermal broadening of data acquired at different T. The effect of thermal broadening on the dI/dV spectra can be expressed as the convolution of the sample density of states and the derivative of the Fermi-Dirac distribution [34],

$$\frac{dI}{dV}(V,T) = \int \rho_t(T)\rho_s(E,T)\frac{d}{dV}F(E-eV,T)dE \propto \rho_s(V,T) * \frac{d}{dV}F(V,T) \tag{3.14}$$

Here ρ_t and ρ_s are the density of states of the tip and sample respectively, * represents a convolution, and the derivative of the Fermi-Dirac distribution is

$$\frac{d}{dE}F(E,T) = \frac{-1}{4k_BT\cosh^2(E/2k_BT)} \tag{3.15}$$

which has a FWHM of $\sim 3.5k_BT$. Using this formalism we can change the temperature of a spectrum from the temperature at which the data was acquired, T_{data}, by deconvolving the spectrum to $T_0 = 0$ K with $\frac{d}{dE}F(E,T_{\text{data}})$, and then convolving the spectrum to an arbitrary simulation temperature T_{sim}. Spectra were convolved and deconvolved by multiplying and dividing in Fourier space, without the use of iterative deconvolutions. As discussed below, the deconvolution only required the use of the $T = 8$ K kernel $\frac{dF}{dE}(E, T = 8\text{K})$, which did not introduce meaningful deconvolution artifacts into the analysis.

We use this technique to compare the data to a simulated series of spectra whose only effect at higher T is due to thermal broadening. To obtain this sequence of simulated spectra, we use the normalized $T_{\text{data}} = 8$ K spectrum in Fig. 3.17c, thermally deconvolve the spectrum to 0 K and then thermally broaden the resultant spectra to T_{sim} to arrive at the series of simulated spectra at T_{sim} in Fig. 3.17d. A comparison between the normalized data in Fig. 3.17c with the simulated data in Fig. 3.17d shows that the peak and dip in the data are being suppressed at a faster rate than the thermal simulation. To more clearly show this, we plot the maximum/minimum value of the normalized spectra at each temperature with the maximum/minimum value of the simulated spectra in Fig. 3.18. Figure 3.18 clearly demonstrates that the peak and dip in the

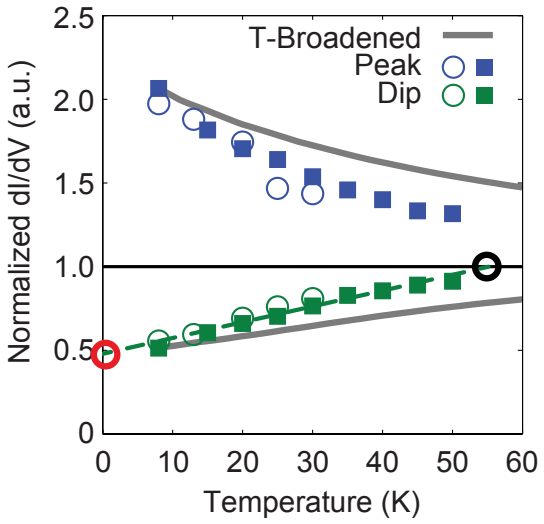

Figure 3.18: Temperature dependence of spectra on the 2×1 surface. Temperature dependence of the peak (blue) and dip (green) features in normalized dI/dV. Open vs. closed symbols indicate two different experimental datasets acquired on different samples with different tips. The simulated reduction (increase) in spectral weight at the peak (dip) due to thermal broadening alone are plotted with thick grey lines, and are slower than the corresponding trends in the data. The closed markers and grey lines are taken from the normalized amplitudes of Fig. 3.17c. The linear extrapolation of the green data upwards indicates that the dip fills around 55 K (black open circle); its extrapolation downwards indicates the existence of residual conductance (red open circle) around half of the background conductance at $T = 0$ K. The non-vanishing negative bias peak at $T = 50$ K indicates incomplete loss of f state coherence at that temperature.

data (squares and circles) are reduced as T increases at a faster rate than the simulation (gray lines). This trend shows a temperature dependent rate exceeding thermal broadening and is very suggestive of Kondo hybridization. Furthermore, it is clear that the Fermi level dip is nearly completely filled by $T \sim 55$ K, which is consistent with the reported T^* where previous bulk experiments have observed a sharp increase in resistivity [43], a sign change of the Hall coefficient [44], a change in the magnetic susceptibility [72], and an abrupt change in Sm valence [79].

3.5.2 Conclusions from temperature dependent spectroscopy

In addition to the upward T extrapolation, extrapolation of the intensity of the Fermi level dip to $T = 0$ K allows us to check whether the in-gap spectral weight is consistent with thermal excitation. Figure 3.18 shows that even at zero temperature, the extrapolated minimum dI/dV

is nonzero and approximately half the background conductance, implying the presence of additional states in the gap even at $T = 0$ K. This contrasts with a two-channel tunneling model of a clean Kondo insulator in which the hybridization gap should completely suppress the Fermi level tunneling conductance at $T = 0$ K [70, 75]. Furthermore, unlike previous STM observations of hybridization gap development in other heavy fermion materials [78, 81, 83], the 2×1 surface of SmB_6 is free from quantum critical fluctuations, impurities, or structural defects, which would increase the self-energy and move spectral weight into the gap [74]. The residual conductance at $T = 0$ and its implications for in-gap states, is consistent with our experimental observation of residual spectral weight in the gap on all four surfaces, as shown in Fig. 3.4. Indeed, we always observed residual zero bias conductance independent of the morphology. Our observation of zero bias tunneling conductance is consistent with the in-gap surface states of a TKI recently suggested by other experiments [48, 51, 54], but we cannot exclude the possibility of topologically trivial surface states [55, 57].

Having assigned the thermal evolution of the T-dependent spectra to Kondo hybridization, we can use the technique of Fig. 3.15 to measure the temperature dependence of the hybridization gap. We again assign the peak-kink energy separation of our experimental dI/dV spectra, Δ^{data}, with the hybridization gap in the f-band DOS, Δ_{hyb}, and plot the raw gap values in Fig. 3.19a. However, to separate the effect of thermal broadening from the temperature evolution of Δ^{data}, we compare Δ^{data} to that of a thermal simulation. The thermal simulation is calculated by measuring $\Delta = |V_p - V_k|$ of the simulated spectra derived by thermally broadening the $T = 8$ K spectrum to arbitrary T^{sim}: $\Delta^{\text{sim}}(T)$ (simulated spectra shown in Fig. 3.17d). $\Delta^{\text{sim}}(T)$ is plotted using solid lines in Fig. 3.19a. Despite the scatter, by comparing $\Delta^{\text{sim}}(T)$ with $\Delta^{\text{data}}(T)$, we observe that overall Δ^{data} is smaller than Δ^{sim}, indicative of a temperature dependent gap reduction. To extract the temperature dependent hybridization gap, instead of employing deconvolution of the higher temperature data, we instead phenomenologically quantify the trend shown in Fig. 3.19a. We define $\Delta_{\text{hyb}}(T) = \Delta(T = 8\,\text{K}) + (\Delta^{\text{data}}(T) - \Delta^{\text{sim}}(T))$. Because $\Delta^{\text{data}} < \Delta^{\text{sim}}$, Δ_{hyb} measures the gap reduction relative to 8K, and effectively removes the effect of thermal broadening. (We note that deconvolution of the spectra by high temperature kernels of the form shown

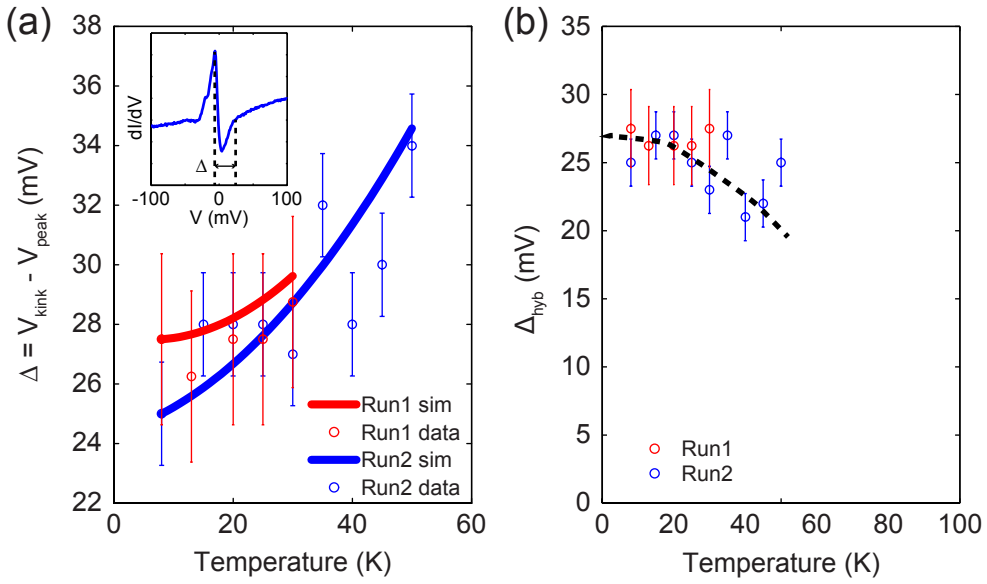

Figure 3.19: Variation of the hybridization gap as a function of temperature on the 2×1 **surface. (a)** Energy separation (Δ) between the positive bias dI/dV kink and the negative bias dI/dV peak at varying temperature. In the inset we plot the $T = 8$ K spectrum shown in Figure 3 and overlay dashed lines to indicate the peak-kink energy separation Δ. The temperature variation of Δ extracted from the data, Δ^{data} is plotted using open circles. The energy of the peaks and kinks were identified from the first and second derivatives of the dI/dV spectra. Red and blue traces reflect two independent temperature dependent datasets acquired on different samples. **(b)** Hybridization gap as a function of temperature. A black dashed line has been superposed as a guide to the eye to illustrate the reduction in Δ_{hyb} as a function of temperature. The error bars shown represent the sum in quadrature of the energy spacing of the measurement and the rms bias modulation amplitude for each dataset. The value of $\Delta_{\text{hyb}}(T = 8K) = 26 \pm 2$ meV reported earlier reflects the average of the values shown in (a) or (b) above with appropriate error propagation.

in Eqn. 3.15 was unreliable without using deconvolution techniques that required assumptions about the experimental noise. For this reason we chose to use the phenomenological definition of Δ_{hyb} to quantify the suppression.)

Figure 3.19b plots $\Delta_{\text{hyb}}(T)$ and shows that the gap has not closed by $T = 50$ K, the reported metal insulator transition in SmB_6. This effect can even be seen in the raw data of Fig. 3.17c, where the edge of the gap at positive bias (V_p) does not shift significantly with T. This partial but incomplete gap closure was recently observed by another ARPES result [64], where they proposed that the 50 K metal insulator transition is caused by the movement of the bands relative to the Fermi level, rather than $\Delta_{\text{hyb}} \to 0$ at 50 K.

The decomposition of dI/dV in Section 3.4 allows us to better understand the temperature evolution of the dI/dV spectra from the 2×1 surface, shown in Figs. 3.17, 3.18. From the decomposition, the dip represents the gap in the DOS from hybridization, while the peak at -8 meV represents the peak due to the interference and the DOS of the f band. Therefore the dramatic reduction in intensity of the -8 meV peak at 50 K stems from reduction of both the f band coherence (decreasing N_f) and the concomitant interference effect (decreasing N_{cf}) as the hybridization weakens. However, the weak residual peak at $T = 50$ K demonstrates that the loss of f band coherence is still incomplete at that temperature, in agreement with recent ARPES measurements [64]. Meanwhile, the more complete elimination of the Fermi level dip near $T = 50$ K could arise from a combination of partial closure of the hybridization gap (Fig. 3.19), as well as broadening of the N_c and N_f channel (and accompanying N_{cf}) into the gap, also in agreement with recent ARPES measurements [64]. The strong temperature dependence of both peak and dip that exceeds thermal broadening, as well as the agreement of our extracted gap-filling temperature around $\sim$ 55 K with abrupt property changes reported by other techniques [43, 44, 72, 79], suggests that our measured temperature dependent dI/dV spectra reflect the Kondo hybridization in SmB_6.

3.6 Discussion of main results

We briefly discuss the implications of our work on previous SmB_6 tunneling experiments, SmB_6 ARPES experiments and the study of Kondo insulators in general.

On all surfaces the STM-measured dI/dV spectra (Figs. 3.4e-h) consistently show a dominant peak on the filled state side, in contrast to PTS/PCS measurements, which show a dominant peak in dI/dV on the empty state side [50, 63]. Previous to our work, the PTS/PCS measurements were puzzlingly in disagreement with the expected lineshape for the bare hybridized DOS $N_c(V)$ and $N_f(V)$ expected for an electron-like $5d$ conduction band [42, 52–57, 65, 66]. To understand this contrast, we note that dI/dV depends on $N_c(V)$ and $N_f(V)$, which are intrinsic properties of the SmB_6 surface, and on the ratio t_f/t_c, which is an extrinsic property of the tunnel

junction. The dependence of dI/dV on t_f/t_c in Fig. 3.12c allows us to conclude that an empty state peak in dI/dV arises only when $t_f/t_c > 0$. For this regime we find that $N_{cf}(V)$ dominates dI/dV and masks the bare DOS by adding a positive bias peak and a suppression at the Fermi level, as shown in Fig. 3.14. The Fermi level dip in PTS/PCS data [50, 63] may therefore represent an energy range of destructive interference, and not necessarily the intrinsic hybridization gap. The relative prominence of the filled state peak in all our STM measurements demonstrates the consistent dominance of the bare DOS and the significance of the STM-observed spectral gap as representative of the true hybridization gap. Furthermore, throughout the $t_f/t_c < 0$ tunneling regime that matches our STM measurements, the modeled differential conductance is vanishingly small within the hybridization gap, in contrast to the in-gap spectral weight we observe on all four surfaces.

Our spatially resolved STM measurements of distinct electronic structure on the several surface morphologies of SmB_6 are consistent with existing ARPES measurements, and can reconcile some apparent discrepancies between them [52–57, 64, 66]. We expect that most ARPES experiments, with typical ∼hundred-micron spot size, will show momentum-resolved contributions from both the Sm-terminated 1×1 and 2×1 morphologies (Figs. 3.4a-b), and possibly the top few layers of the bulk, but not from the two disordered morphologies where k is a poor quantum number (Figs. 3.4c-d). Depending on the fractional composition of the cleaved surface structure, as well as the photon energy, depth probed, and detector resolution, ARPES may observe the spatial average of the -28 meV and -8 meV hybridized f bands from the two Sm-terminated surfaces as a single dispersing [64] or broadened f band at intermediate energy [53–55, 66], or as one [57] or two [52, 56] separate states. In the latter scenario, the -8 meV hybridized f band has been interpreted as an 'in-gap' state [52, 56]. However, we note that a topological in-gap state would be expected to span the upper and lower hybridized bands, and thus would appear as continuous spectral weight filling the hybridization gap, rather than as a sharp peak at a specific energy as claimed in Refs. [52, 56]. Indeed, we consistently observe broad in-gap spectral weight on all surfaces that could be consistent with in-gap states.

With these first atomically resolved spectroscopic measurements on SmB_6, we provide a gen-

eral new paradigm for interpreting Kondo hybridization, and lay the specific groundwork for understanding TKIs. First, our explicit decomposition of the measured tunneling conductance into DOS vs. interference channels provides an intuitive way to understand tunneling measurements of Kondo hybridization in a broad class of heavy fermion materials [50, 77, 78, 81, 83]. Second, we confirm that SmB_6 is a Kondo insulator, by using this decomposition to reveal the full f band hybridization gap, spanning the Fermi level, on all four observed surface morphologies. Our temperature dependent spectroscopy on the nonpolar 2×1 surface points to the hybridization gap first crossing the Fermi level around $T^* \sim 55$ K, in agreement with previous bulk measurements. However, at low T, the apparent broadening of states into the gap significantly exceeds that expected for the self energy of 8 K, indicating that there may be an independent source of states within the gap. Our hypothesis is in line with the ARPES experiments that have shown evidence of (not necessarily topological) surface states. Third, our observation of the hybridized f band shifts between polar and non-polar cleaved surfaces of SmB_6 reveals the dramatically different electronic environments in which the predicted topological surface state must exist. Theoretical modeling of bulk band shifts, surface states, and hybridization for different surface terminations is urgently needed. Our work provides the nanoscale spectroscopic details necessary for understanding the first strongly correlated topological insulator.

4

Impurity induced phase separation and scattering in $Bi_{2-x}Fe_xSe_3$

Recent work on the topological insulator Bi_2Se_3 has focused on doping Bi_2Se_3 to move the chemical potential into the bulk gap and inducing ferromagnetism using magnetic transition metal elements. In this chapter, we present experimental results on Bi_2Se_3 doped with the transition metal Fe. We observe an impurity phase separation which points to the difficulty of uniformly doping Fe into Bi_2Se_3. The Fe impurities form a scattering center from which we observe scattering of the TSS and a trivial surface state at higher energies than previously expected, which is supported by density functional theory calculations.

4.1 Introduction

Recent interest in the newly discovered topological insulator (TI) materials has been driven by the push to engineer novel devices utilizing the unique characteristics of TIs. In TIs, strong spin-orbit interactions cause a a band inversion that leads to a nontrivial band topology, and metallic topological surface states (TSS) that span the bulk band gap [1–4]. The TSS possess unique characteristics, namely spin-momentum locking, which leads to unique properties that can be exploited for potential applications in spintronics, transistors or in novel quantum computing devices [2–4].

Recent experimental efforts have focused on manipulating the prototypical TI Bi_2Se_3 in hopes of realizing novel topological devices. By tuning the magnetic interactions, for example via magnetic dopants, Bi_2Se_3 is predicted to enter a ferromagnetic phase which breaks the time reversal symmetry and topological character of the surface states [84, 85]. A number of studies have focused attention on using Fe to dope Bi_2Se_3 [86–91]. However, numerous unresolved questions remain regarding $Bi_{2-x}Fe_xSe_3$, including whether a gap opens at the Dirac point [86, 88, 89], the effect of trivial 2D surface states [88, 90], and whether the growth conditions in bulk $Bi_{2-x}Fe_xSe_3$ crystals permit a uniform ferromagnetic phase [92]. On another front, the fabrication of devices, such as field effect transistors, using Bi_2Se_3 have produced promising initial results [93]. While the band structure of the occupied states is well studied, understanding the effect of applying a positive bias gate to Bi_2Se_3 is complicated by the lack of spectroscopic studies at energies above the Fermi level. Recent studies have even pointed to a wealth of unexplained physics at large positive biases, including topologically trivial 2DEGs [94, 95], and an additional Dirac cone [96, 97].

4.1.1 Summary of Results

Scanning tunneling microscopy has been used to great effect in the study of TIs, and has been used to image nanoscale electronic variations in Bi_2Se_3 [98], dopant induced charge inhomogeneity [99] and TSS scattering processes [35, 100–102]. In this chapter we report on a study of bulk

doped crystals of $Bi_{2-x}Fe_xSe_3$ using scanning tunneling microscopy (STM) and spectroscopy. We observed a surprising macroscopic phase separation of the Fe dopants into Fe-doped and undoped regions of Bi_2Se_3. This dopant segregation is likely due to inhomogeneous local growth conditions related to the local anion/cation growth conditions. We used Fourier transform scanning tunneling spectroscopy to resolve two quasiparticle scattering modes in the unoccupied states in an energy range 0.65 to 0.85 eV above the Dirac point. We find that the two scattering modes are separated by 0.1 eV, and are caused by the SS and the topologically trivial quantum well state (QWS) respectively. Both scattering modes have a velocity of $v_q = 1.1 \pm 0.3$ eV Å, which is 3× lower than the velocity at the Dirac point [103], and is explained by our finite slab density functional theory (DFT) calculations. Our results show that the topological surface state remains quantized from the bulk to higher energies than expected [104], and point to the important effect of QWS on the TSS in Bi_2Se_3.

4.1.2 Experimental Methods

We studied $Bi_{2-x}Fe_xSe_3$ single crystals with nominal Fe doping of $x = 0.03$, $x = 0.07$, and undoped Bi_2Se_3 single crystals. Sample preparation methods and the characterization of the crystals has been described in previous work [105, 106]. The single crystals were cleaved along the (001) direction, in cryogenic vacuum at 40 K and immediately inserted into the STM. The (001) orientation was confirmed by measuring step heights that were integer multiples of the height of a Bi_2Se_3 quintuple layer (QL), as shown in Fig. 4.1.

Density functional theory (DFT) calculations were performed using the linearized augmented-plane-wave method in the WIEN2K packages [107], with structural parameters from Zhang *et al.* [104]. Spin-orbit interaction is included as a second variational step using scalar-relativistic eigenfunctions as a basis; exchange and correlation effects are treated within the generalized gradient approximation [107].

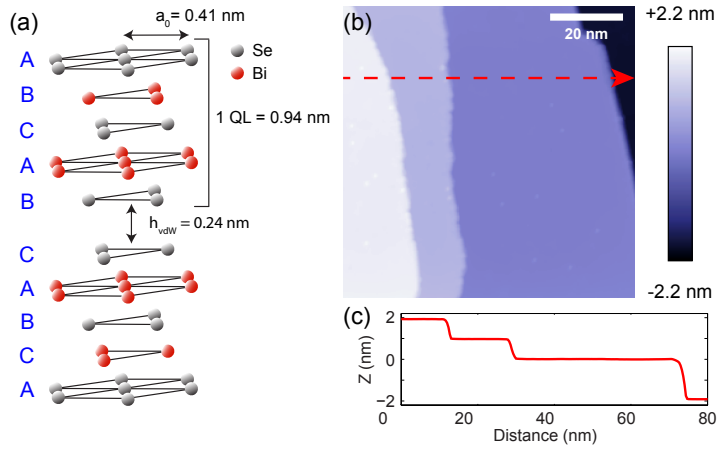

Figure 4.1: Crystal structure and characterization of $Bi_{2-x}Fe_xSe_3$. (a) Schematic crystal structure of Bi_2Se_3. Two quintuple layers (QL) of Bi_2Se_3 are shown, with the three lattice orientations of each of the sublayers, designated A-B-C. The natural cleavage plane is between the two QLs, which will expose a Se terminated layer in each half. **(b)** Topography of cleaved surface of $Bi_{2-x}Fe_xSe_3$ over an 80 nm x 80 nm field of view. Four atomically flat terraces are visible. ($T = 4.4$ K; $V_s = 800$ mV; junction resistance $R_J = 80$ GΩ.) **(c)** Height profile taken along the dashed red line of (b). The separation of the terraces is in integral multiples of the height of 1 QL of Bi_2Se_3.

4.2 Impurity phase separation

The majority of the cleaved $Bi_{2-x}Fe_xSe_3$ surfaces we studied were atomically flat over at least 10 - 100 nm length scales (see Fig. 4.2a). Figure 4.2b shows a typical dI/dV spectrum of $Bi_{2-x}Fe_xSe_3$ with a Dirac point at $V = -350$ mV, consistent with previous measurements [89]. Compared to the Dirac point on a pristine Bi_2Se_3 surface (spectrum shown in blue in Fig. 4.2b), $Bi_{2-x}Fe_xSe_3$ has a Dirac point that is 50 mV lower, in agreement with previous work showing that Fe is an electron donor [87, 90]. Topographic images of $Bi_{2-x}Fe_xSe_3$ acquired on the flat terraces revealed multiple species of three-fold symmetric impurities, as shown in Figure 4.2a,c. Following the work of Song *et al.* [87], using the topographic images in Fig. 4.2a,c we can identify the impurities based on the size of the impurity and its lattice orientation. Figure 4.1a shows that each sublayer of the Bi_2Se_3 crystal alternates between an A, B or C lattice orientation. Furthermore, the deeper the impurity is within the crystal, the larger its spatial extent on the topmost Se layer [108]. These two facts allow us to identify the impurity by its phase relative to the topmost Se layer and its vertex-vertex length. From the atomically resolved images of Fig. 4.2c, the

red circled dark triangular impurity is out of phase with the A lattice, and has a vertex-vertex length of $1a_0$. We identify it as a Fe substitution for a Bi atom in the 1st (topmost) Bi sublayer, denoted Fe_{Bi1}. The orange circled triangular impurity is in phase with the topmost Se lattice, and has a vertex-vertex length of $3a_0$, which leads us to identify it as a Bi atom in the 2nd Bi sublayer, denoted Fe_{Bi2}. We note that with one exception, shown in green in Figs. 4.2a,c which we discuss later, all of the other impurities in Figs. 4.2a,c are consistent with and were identified in previous work [87]. The presence of Bi substitutional impurities and the absence of Se vacancies is characteristic of other STM topographies of TM-doped Bi_2Se_3 compounds [90, 98, 109] and is in agreement with theoretical models [110–112]. However, in contrast to previous work that studied $Bi_{2-x}Fe_xSe_3$ *thin-films* [87], in our doped *crystals* the density of defects in Fig. 4.2a ($n \sim 0.04$ nm^{-2}) is lower than the nominal concentration by more than a factor of 10. This mismatch could be explained by our observation of dopant clustering as shown in Fig. 4.2d, which would result in an inhomogeneous distribution of Fe dopants.

On the same $Bi_{2-x}Fe_xSe_3$ cleaved surface but separated by > 10 μm, we acquired topographic images with a different defect distribution, as shown in Fig. 4.3a. Se vacancies, shown as bright triangular impurities (green circles in Fig. 4.3a), are the dominant impurities in this other region, as opposed to the Fe_{Bi1} impurities that dominate in Fig. 4.2a. In fact, throughout the ~ 1 μm area around the region shown in Fig. 4.3c, we did not find any of the Fe impurities identified by Song *et al.* [87]. We verified our identification of the green circled impurities as Se vacancies by comparing the impurities in Fig. 4.3a to the Se vacancies [113] in an undoped Bi_2Se_3 topographic image, as shown in Fig. 4.3b. The similar defect distribution in Figs. 4.3a and 4.3b suggests that the region shown in Fig. 4.3a is an undoped portion of the $Bi_{2-x}Fe_xSe_3$ crystal. Recent calculations [111, 112] have suggested that the allowed impurities in Bi_2Se_3 depend sensitively on the type of dopant and whether the crystal is grown in a Bi or Se rich environment. Because Fe is the smallest of the transition metal (TM) Bi_2Se_3 dopants, the size mismatch between Fe and Bi makes it relatively difficult to dope [111]. As shown in Fig. 4.3c, doping Fe into Bi_2Se_3 is only favored in Se-rich conditions [111] which also inhibits the formation of Se vacancies [114, 115]. Likewise, Bi-rich conditions inhibit Fe but promote Se vacancies [111]. Our results therefore point to

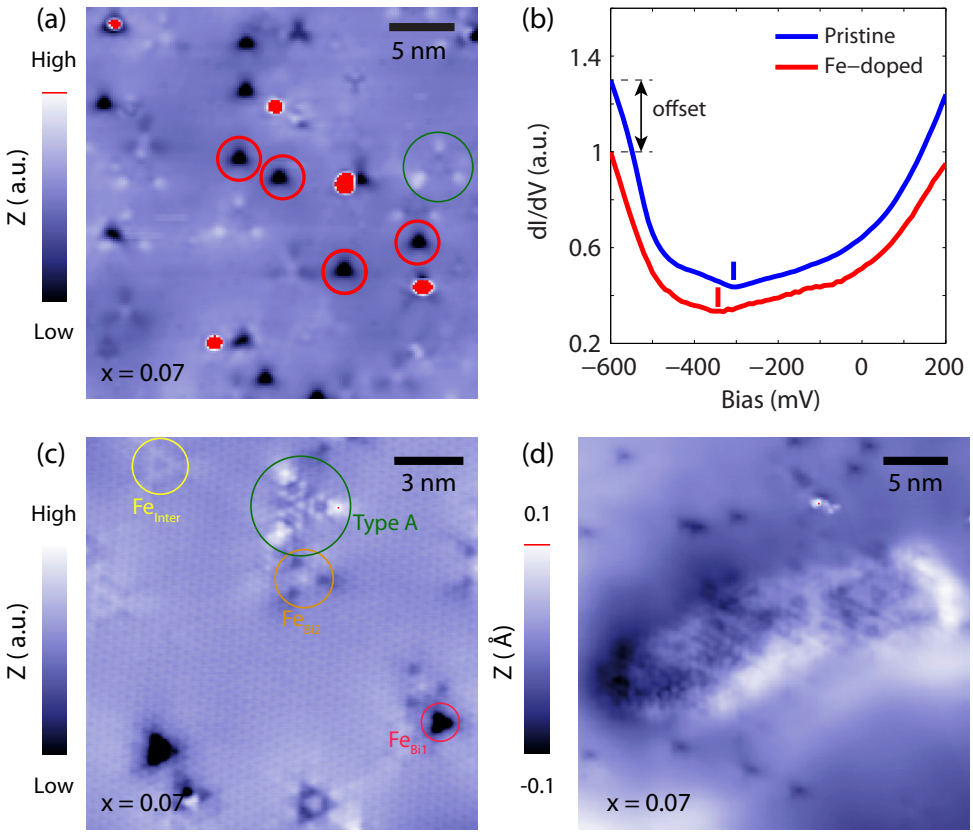

Figure 4.2: Characterization of $Bi_{2-x}Fe_xSe_3$ ($x = 0.07$). **(a)** Topography of 30×30 nm^2 field of view acquired at $T = 4.6$ K, $V_s = 1$ V, $I_s = 20$ pA. Red circles highlight Fe_{Bi1} impurities. **(b)** dI/dV spectra acquired on the $Bi_{2-x}Fe_xSe_3$ surface shown in red, and the Bi_2Se_3 surface shown in blue. The minimum in each spectrum is indicated with the red (-350 mV) and blue (-300 mV) dashes. The spectra have been scaled and offset for clarity. $Bi_{2-x}Fe_xSe_3$ spectrum acquired at $T = 4.4$ K, $V_s = 0.5$ V, $I_s = 200$ pA, $V_{\text{rms}} = 14$ mV. Bi_2Se_3 spectrum acquired at $T = 8.2$ K, $V_s = 0.4$ V, $I_s = 400$ pA, $V_{\text{rms}} = 10$ mV. **(c)** Identification of Fe impurities. Topographic image of a 16.8×16.8 nm^2 acquired at $T = 4.4$ K, $V_s = 500$ mV, $I_s = 100$ pA, $B = 0$ T. Three types of impurities that were previously identified [87] are highlighted: (1) Fe_{Bi1}, identified in red, is a Fe substituting for a Bi in the 2nd subsurface layer that has an B oriented lattice (see Fig. 4.1a); (2) Fe_{Bi2} identified in orange, is a Fe substituting for a Bi in the 4th subsurface layer that has an A oriented lattice (see Fig. 4.1a); (3) Fe_{inter} is an interstitial Fe impurity. The Type A impurity, identified in green, has not been previously reported [87, 90]. **(d)** Suspected Fe cluster in $Bi_{2-x}Fe_xSe_3$ crystals. 30×30 nm^2 topography acquired at 7 K, $V_s = 0.3$ V, $I_s = 30$ pA.

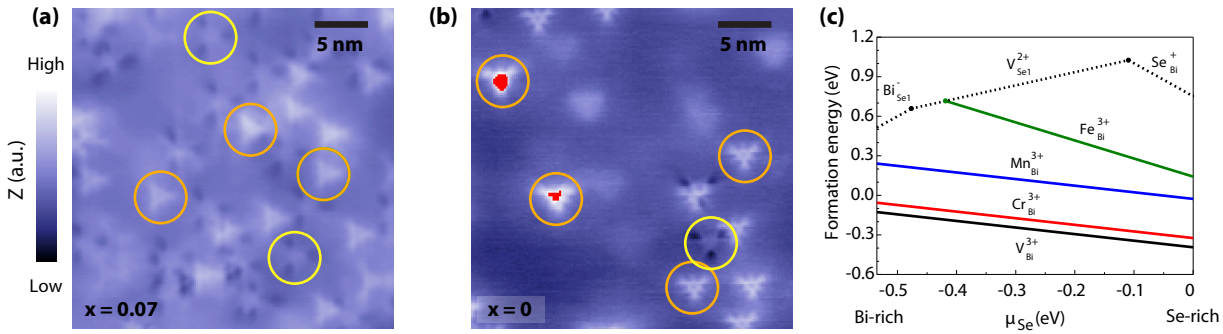

Figure 4.3: Macroscopic phase separation of impurities in $Bi_{2-x}Fe_xSe_3$ Topography of 30×30 nm^2 field of view of $Bi_{2-x}Fe_xSe_3$ ($x = 0.07$) (a), and Bi_2Se_3 (b). Orange circles highlight Se vacancies, which are common to undoped Bi_2Se_3. Yellow circles highlight a native defect that could be a Se_{Bi} antisite. Nominal dopant concentration indicated in the bottom left of each panel. Experimental conditions for topography: (a) $T = 4.4$ K, $V_s = 0.5$ V, $I_s = 50$ pA; (b) $T = 2.2$ K, $V_s = 0.4$ V, $I_s = 30$ pA **(c)** The dependence of impurity formation on growth conditions. Figure adapted from Ref. [111]. μ_{Se} is the Se chemical potential, and the far left indicates Bi rich growth conditions, while the far right side indicates Se rich growth conditions.

an inhomogeneous $Bi_{2-x}Fe_xSe_3$ growth process where impurities segregate depending on the local cation/anion environment, resulting in a very inhomogeneous Fe distribution in the crystal.

4.3 Quantum well state induced scattering

We now discuss results from our studies of the Fe-doped regions of $Bi_{2-x}Fe_xSe_3$.

4.3.1 Observation of Quasiparticle interference

Despite the weak warping of the CECs that limits the observation of quasiparticle interference (QPI) in Bi_2Se_3 [103, 116], in the Fe-doped regions similar to Fig. 4.2a,c we observed two scattering modes at $V_s > 0.3$ V. In Fig. 4.4 we show a topographic image of a region where we observed QPI. The distinguishing feature of this region is the high concentration of a large impurity, which we name "Type A", that to our knowledge has not been previously reported in $Bi_{2-x}Fe_xSe_3$ or other TM-doped Bi_2Se_3 compounds. As shown in Fig. 4.5a,e, the Type A impurities are large scattering centers, with a vertex to vertex distance of $6a_0 = 2.4$ nm. The spectroscopic signature of the impurity is mainly seen at positive biases (Fig. 4.5b-d, f), and it un-

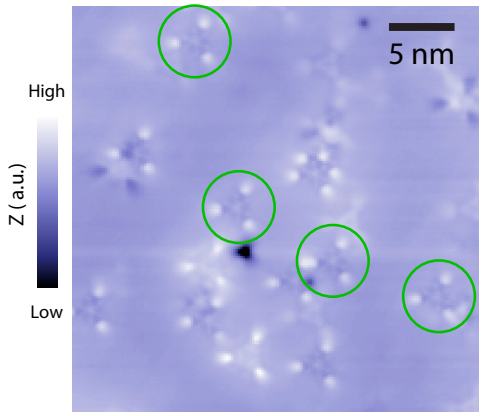

Figure 4.4: Fe-doped region with QPI. Topographic image of a 30 × 30 nm^2 region of $Bi_{2-x}Fe_xSe_3$ where QPI was observed (T = 6 K, V_s = 0.6 V, I_s = 30 pA). Area has a high concentration of Type A impurities, a subset of which are circled in green.

dergoes a phase inversion in dI/dV images at $\sim$ 400 mV. Fig. 4.5e shows that the center of the Type A impurity is centered on a lattice site of the topmost Se lattice. Therefore, because of its large size and its lattice orientation being in phase with the topmost Se lattice, the Type A could be an interstitial impurity sitting in the hollow between the Se layers that make up the van der Waals (vdW) gap.

The Type A impurity served as a high amplitude scattering center, allowing us to image quasiparticle interference from the surface states. The two quasiparticle scattering modes are shown in Fig. 4.6. The lower energy mode, q_1, disperses between 300 mV to 420 mV (Fig. 4.6a-e), while the higher energy mode, q_2 disperses between 430 mV to 520 mV (Fig. 4.6k-o). In the dI/dV maps of Fig. 4.6, the QPI can be seen as wavefronts that scatter off of the Type A impurities, and disperse with energy. To better visualize the scattering, we computed the Fourier transform of the real space dI/dV maps of Fig. 4.6, which shows that both q_1 (Fig. 4.6f-j)and q_2 (Fig. 4.6p-t) disperse in the Γ-M direction. We note that QPI was only observed in regions with a high density of Type A impurities, and we did not observe scattering in the Γ-K direction.

The dispersion of the scattering modes along the symmetry directions is shown in Fig. 4.7, which plots the intensity of the FT-dI/dV maps shown in Fig. 4.6 along the high symmetry directions. While the q_1 and q_2 modes are visible in the raw Fourier transform linecuts of Fig. 4.7, a common isotropic background is present in both the Γ-M and Γ-K linecuts that masks the in-

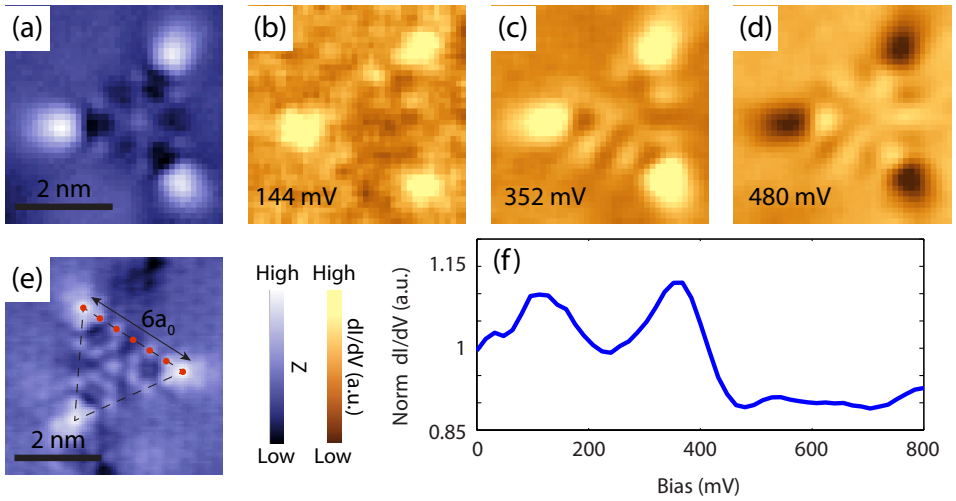

Figure 4.5: Characterization of Type A impurity. Topographic image **(a)** and associated dI/dV conductance maps at indicated bias **(b) - (d)** ($T = 4.4$ K, $V_s = 500$ mV, $I_s = 100$ pA, $V_{\rm rms} = 14$ mV, $B = 9$ T). **(e)** High resolution topography of Type A impurity. Red dots and dashed line have been overlaid as guides to the eye to illustrate the internal structure of the impurity. The vertex to vertex length of the impurity is exactly $6a_0$ ($T = 4.4$ K, $V_s = 500$ mV, $I_s = 100$ pA, $B = 0$ T). **(f)** dI/dV spectrum acquired on the vertex of the impurity shown in (a). The spectrum on the vertex has been normalized by a spectrum taken in the background away from impurities. Two prominent peaks are seen at ~ 110 mV and ~ 350 mV. The spectrum was acquired from the spectroscopic map of (a) - (d) using the same experimental parameters.

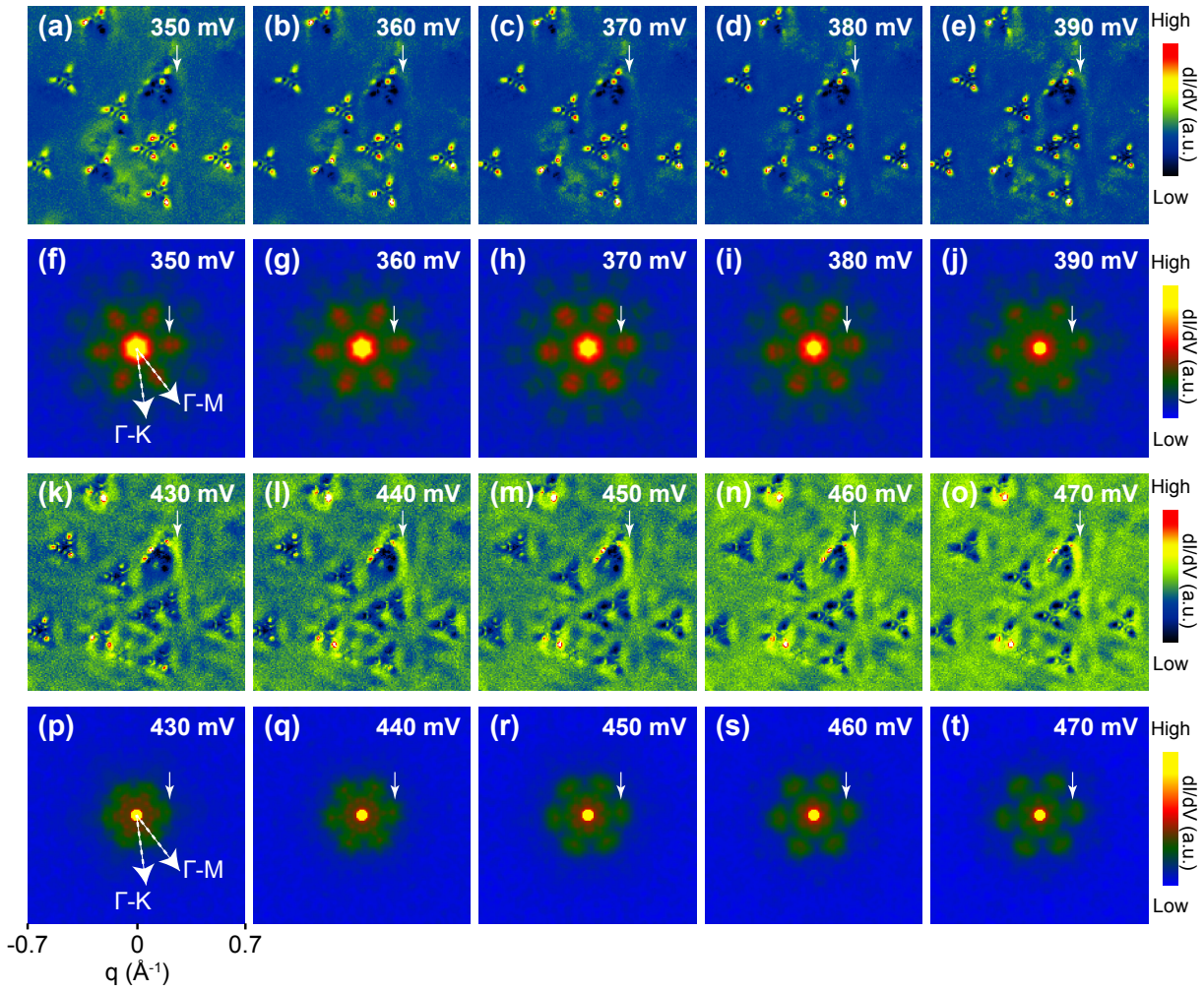

Figure 4.6: Quasiparticle interference in $Bi_{2-x}Fe_xSe_3$. Scattering of the q_1 mode shown in (a-j), and the q_2 mode shown in (k-t). **(a-e); (k-o):** dI/dV maps at the indicated bias over the 30×30 nm^2 region shown in Fig. 4.4 ($T = 6$ K, $V_s = 0.6$ V, $I_s = 300$ pA, $V_{\rm rms} = 7$ mV). A white arrow is overlaid over the images to show that as the energy is increased the wavefront moves towards the impurity. **(f-j); (p-t):** Fourier transform dI/dV maps at the indicated bias ($T = 6$ K, $V_s = 0.6$ V, $I_s = 300$ pA, $V_{\rm rms} = 5$ mV). The Fourier transforms were taken over 60×60 nm^2 regions encompassing the regions shown in (a-e), and (k-o), respectively. A white arrow is superposed to show that as energy increases the scattering wavevector increases in the Γ-M direction.

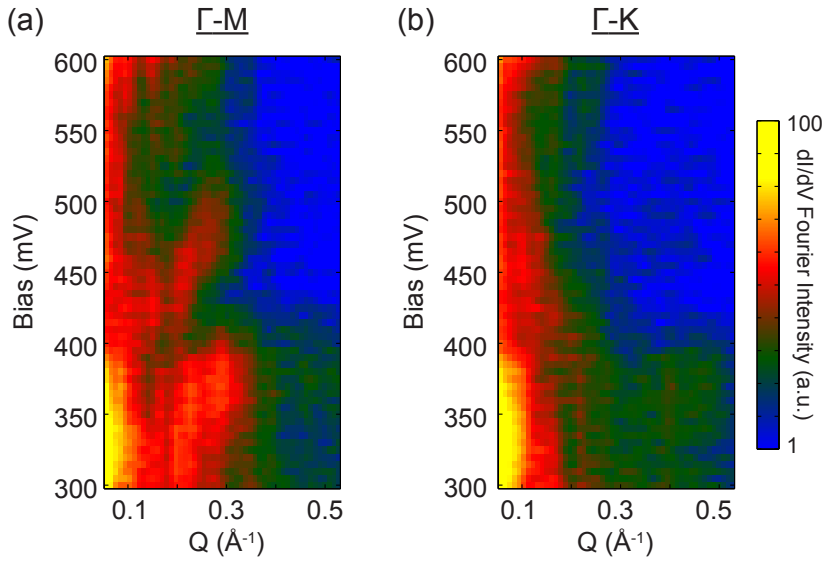

Figure 4.7: Scattering linecuts in symmetry directions. Linecuts of Fourier transform dI/dV spectroscopy map shown in Fig. 4.6. Linecuts are taken in the (a) Γ-M and (b) Γ-K directions. The difference of the two images gives the data plotted in Fig. 4.8, which highlights the q_1 and q_2 Γ-M scattering modes. The dI/dV maps were normalized by energy layer, Fourier transformed and six-fold symmetrized along a Bragg direction.

tensity of the scattering modes. Therefore to better display q_1 and q_2, we minimized the effect of this long wavelength isotropic background by subtracting the intensity of the FT-dI/dV maps in the Γ-M direction ($I(q_{\Gamma-M})$) from the intensity in the Γ-K direction ($I(q_{\Gamma-K})$). We then plot this quantity ($I(q_{\Gamma-M}) - I(q_{\Gamma-K})$) as a function of bias voltage V_s and wavevector q in Figure 4.8. The quantity $I(q_{\Gamma-M}) - I(q_{\Gamma-K})$, achieves the effect of minimizing the isotropic component of the long-wavelength background. Figure 4.8 clearly shows two scattering modes: q_1 between 300 - 420 mV bias, and q_2 between 430 - 520 mV bias, with similar slopes and an energy separation ~ 0.1 eV.

4.3.2 Parameters of the scattering modes

An examination of Fig. 4.8 shows that both q_1 and q_2 abruptly end at two wavelengths: $q = 0.2$ Å^{-1} and $q = 0.3$ Å^{-1}. The abrupt cut-off of the q_1 and q_2 modes can be understood by understanding the scattering length scales in this system. The high wavevector cutoff $q = 0.30$ Å^{-1} $\rightarrow$

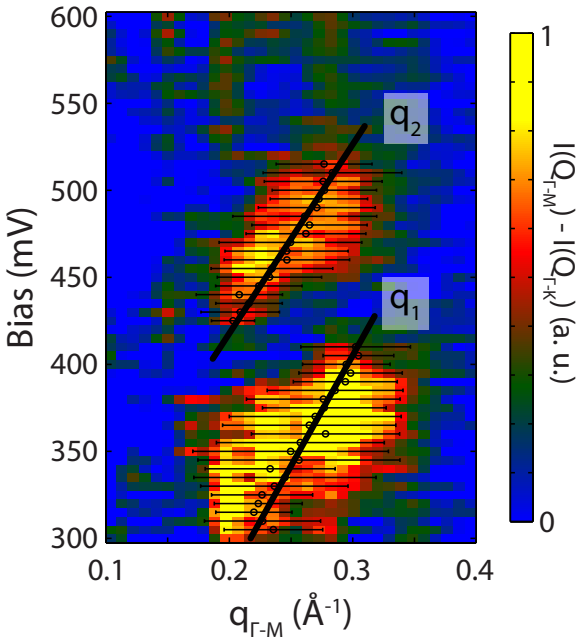

Figure 4.8: Scattering modes in $Bi_{2-x}Fe_xSe_3$. Fourier linecut showing q_1 and q_2 scattering modes. The Fourier intensity of a linecut in the Γ-M direction is subtracted by the Fourier intensity of a linecut in the Γ-K direction for the FT-dI/dV maps shown in Fig. 4.7. The superposed black circles and error bars are the respective center and standard deviation of Gaussian fits to the intensity at each bias (see Fig. 4.9). The thick black line is a linear best fit to the black circles, from which we extract the scattering velocities: $v_1 = 1.28 \pm 0.39$ eV Å, $v_2 = 1.06 \pm 0.32$ eV Å.

$l = 24.2$ Å matches well with the vertex-vertex length of the Type A impurity scattering centers $l = 6a_0 = 2.4$ nm. Meanwhile, the low wavevector cutoff $q = 0.20$ Å^{-1} $\rightarrow l = 36.3$ Å matches well with the average impurity separation $\sqrt{n^{-1}} = 5.2$ nm, where n is the observed defect density. Therefore the length scales from the size of Type A scattering center, and the defect density, can quantitatively explain the restricted q-space range of q_1 and q_2.

To quantify the dispersion, we first performed Gaussian fits to the Fourier intensity of Fig. 4.8 at each bias. Figure 4.9 shows a subset of the wavevector profiles at fixed energies that were extracted from $I(q_{\Gamma-M}) - I(q_{\Gamma-K})$ as shown in Fig. 4.8. Gaussian fits to each wavevector profile are overlaid on top of the data in Figure 4.9 and the centers and standard deviations of the Gaussians are overlaid on the scattering data in Fig. 4.8. To measure the velocities of q_1 and q_2, we fit the centers of the Gaussians to $E = vq + E_0$ and extracted the velocity from the best fit parameters to the data. We found the velocity of q_1: $v_1 = 1.28 \pm 0.39$ eV Å, and the velocity of q_2: $v_2 = 1.06 \pm 0.32$ eV Å, where the error bars represent confidence intervals of the fitting. The linear fits to the extracted scattering mode centers are superimposed on the data in Fig. 4.8. The fitting leads to two intriguing observations that we address in the remainder of this chapter. Firstly, the scattering velocities of q_1 and q_2, $v_q \sim 1.1 - 1.3$ eV Å, are substantially reduced from the band velocity at the Dirac point ($v_D = 3.5$ eV Å) [103]. Secondly, the velocities of q_1 and q_2 are equal within error, but the modes themselves are offset in energy by ~ 100 mV.

4.4 Quantum Well States in $Bi_{2-x}Fe_xSe_3$

4.4.1 Evidence for Quantum Well States

Our observation of two energy offset parallel dispersing modes is hard to explain based off of scattering from a single band, but could be explained using two bands separated in energy by ~ 0.1 eV. Indeed, ARPES experiments have observed additional quantized bands separated from the TSS by a comparable energy scale. These bands are 2 dimensional QWS [95, 117–120], whose origin is unclear but has been reported by multiple groups. An ARPES intensity map taken from Ref. [117] showing the QWS is shown in Fig. 4.10a.

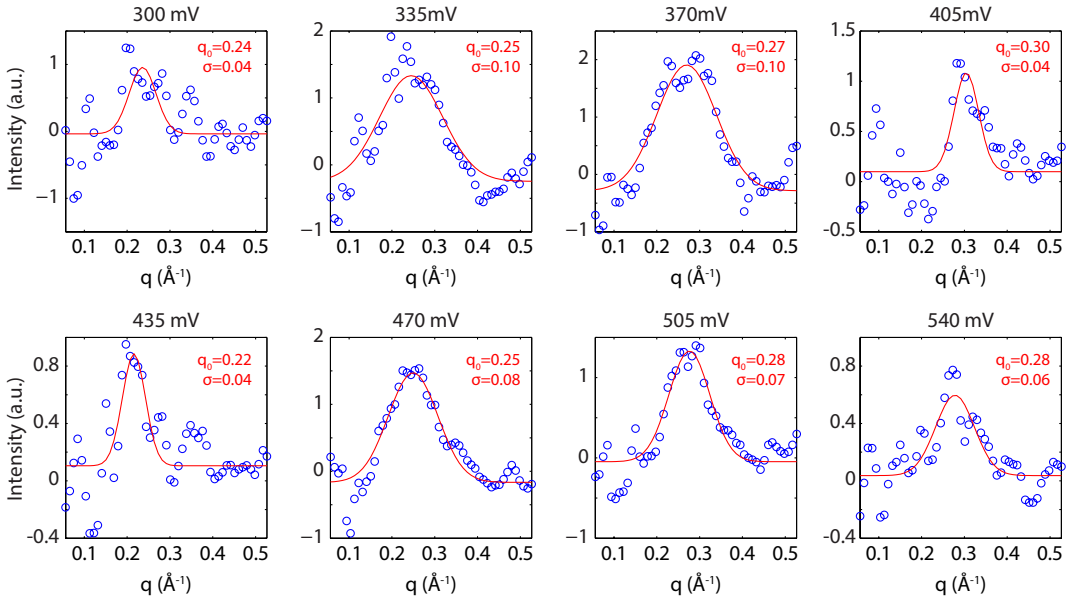

Figure 4.9: Gaussian fits of the q_1 and q_2 wavevectors. At each bias (indicated above the subpanels), I(Γ-M)-I(Γ-K) from Fig. 4.8 is plotted with blue circles, and is fitted to a Gaussian (red line) with a constant offset. The center of the Gaussian q_0 and the standard deviation σ of the fit are shown in each panel. For all energies, $q_0 \pm \sigma$ are plotted in Fig. 4.8.

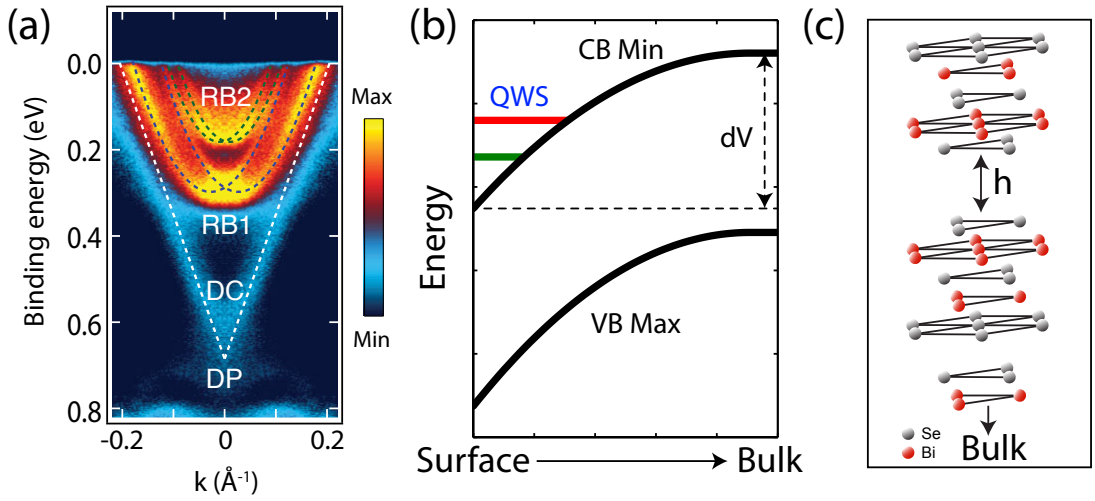

Figure 4.10: Quantum well states in Bi_2Se_3. (a) ARPES intensity map showing QWS induced by K adsorption onto the Bi_2Se_3 surface. The energy separation is on the order of ~ 0.1 eV. Figure adapted from data in Ref. [117]. **(b)** Band bending as a mechanism to induce QWS. The conduction band (CB) minimum and valence band (VB) maximum are shifted in energy downwards by dV at the surface relative to the bulk. Downward band bending of the CB creates a potential well, resulting in quantum well states (red and green). **(c)** Expansion of van der Waals gap as a mechanism to induce QWS. As the separation h between the topmost QL and the crystal increases, the electrons at the surface become more vertically confined leading to QWS.

The QWS is commonly believed to arise from either: (1) band bending caused by surface adsorbants [95, 117–122], or (2) structural asymmetry caused by a van der Waals gap expansion [123, 124]. Fig. 4.10b,c show cartoons illustrating both mechanisms. In the band bending scenario, an asymmetry at the surface causes an electrostatic potential gradient normal to the surface. The potential gradient shifts the energies of the bands as a function of depth, as shown in Fig. 4.10b, causing a potential well to form near the surface. The bound states of this potential well are the 2-dimensional quantum well states. In the van der Waals (vdW) gap expansion scenario, an expansion of the vdW gap isolates the topmost QL from the bulk, confining the electrons in the top QL. If the vdW is expanded by more than $\sim 0.24 - 0.48$ Å [123], QWS are induced at the surface. In our case, we cannot discount either scenario. We observed that the Type A impurities are charged surface impurities, which would support a band bending origin to the QWS. Alternatively, the extreme inhomogeneity of the dopants, including surface clusters with a height ($\sim$ 1 Å) that exceeds the threshold van der Waals gap expansion, points also to a structural origin of the QWS.

Regardless of the specific mechanism, we further validated the presence of QWS by finding spectroscopic evidence from dI/dV spectra. In Fig. 4.11 we show spatially averaged dI/dV spectra over a range of bias where we observed QPI, and at a variety of different experimental conditions. In all cases, we observed kinks in the spectra, indicated with grey vertical bars, which are signatures of the TSS and the QWSs. This conclusion is supported by our modeling, in which we performed density functional theory (DFT) calculations, as shown in Fig. 4.12. Fig. 4.12 shows that for a range of slab thicknesses, the DOS resulting from the calculated DFT bands shows kinks on top of an increasing background DOS. Therefore we associate the kinks with the presence of abrupt changes in the band structure due to the onset of QWS. From the DFT calculations the Dirac point became gapped for $N \leq 4$, and so we chose to focus on calculations with a thickness $N \geq 5$ QL because it was the simplest system that preserved the Dirac degeneracy in our calculations (we will later show that $N = 5$ also self-consistently reproduced the energy separation between q_1 and q_2 modes - see Sec. 4.4.3).

In Figure 4.13 we summarize the agreement between our DFT calculations and the high bias

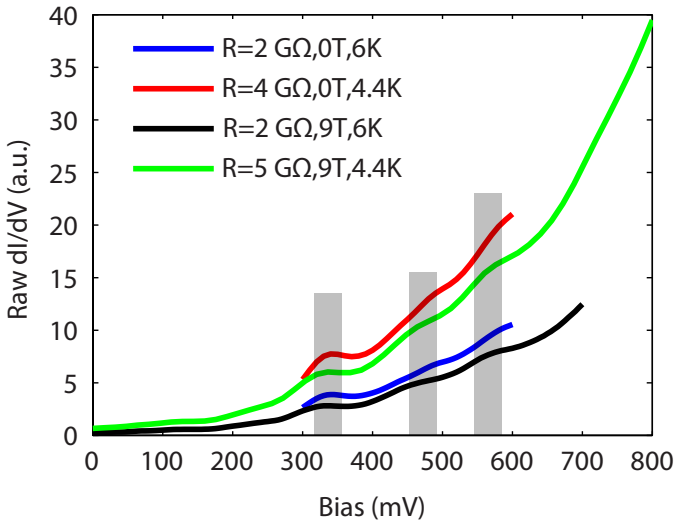

Figure 4.11: High bias dI/dV showing kinks due to QWSs. dI/dV spectra were acquired at the listed experimental conditions, with varying junction resistance $R = V_s/I_s$. The junction resistance is exponentially dependent on the tip-sample separation. Grey bars are overlaid to show the approximate positions of kinks in the spectra, which we identify as signatures of the TSS and QWSs. The energy kinks are consistent across spectra taken with different experimental conditions, both in and out of magnetic field. Experimental conditions not listed in the legend: blue ($V_s = 600$ mV, $V_{\text{rms}} = 5$ mV), red ($V_s = 400$ mV, $V_{\text{rms}} = 14$ mV), black ($V_s = 700$ mV, $V_{\text{rms}} = 5.6$ mV), green ($V_s = 500$ mV, $V_{\text{rms}} = 14$ mV).

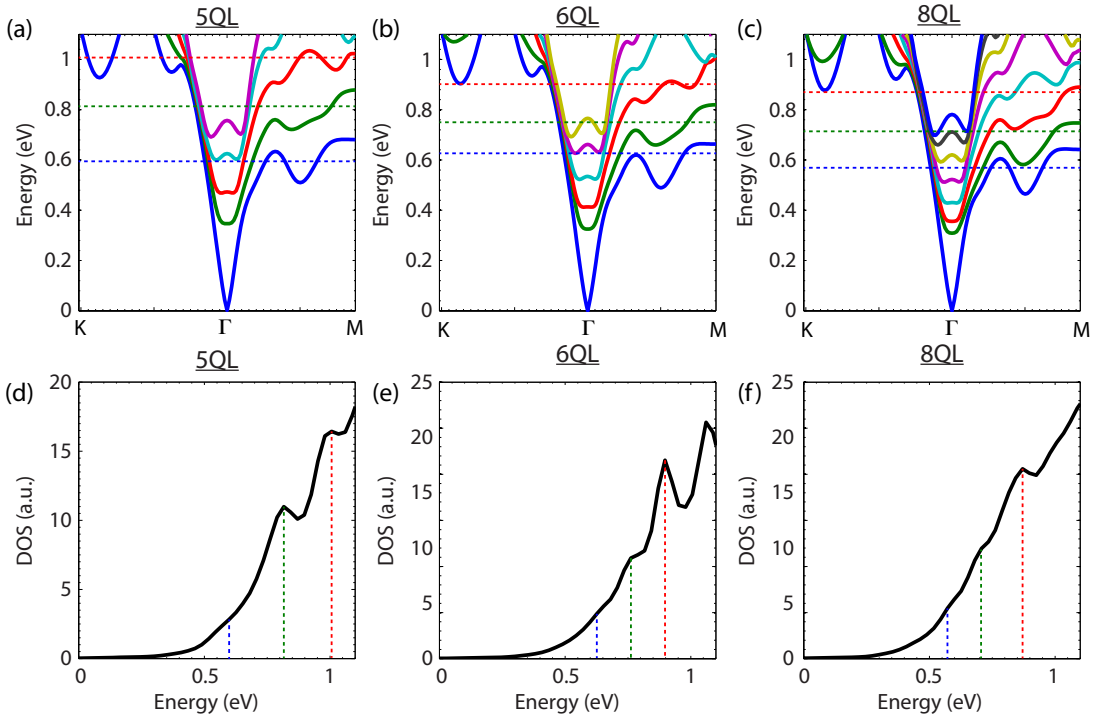

Figure 4.12: DFT calculations at different slab thicknesses. (a)-(c): DFT bands at varying QL thicknesses. **(d)-(f)**: Calculated DOS at varying QL thicknesses. Dashed vertical lines in (d)-(f) are the guides illustrating the energies of the kinks in the DOS. Horizontal lines in (a)-(c) match the respective energies of the kinks in (d)-(f). Calculations for the DFT bands were conducted with a much finer k-mesh than the DOS calculations in (d)-(f). 5QL DOS calculation of (d) was performed with a coarse k-mesh comparable to (e),(f), but less well resolved compared to Figs. 4.13, 4.14. The effective energy resolution of (d)-(f) is 21 meV, 62 meV, and 76 meV respectively.

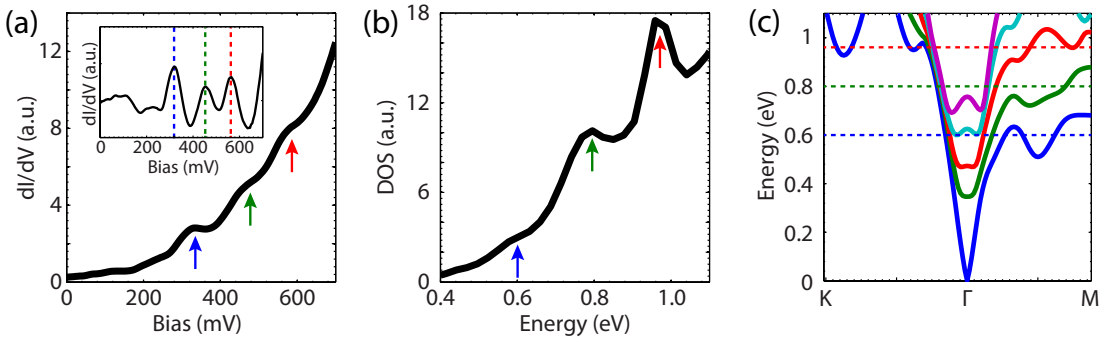

Figure 4.13: Evidence for quantum well states in dI/dV spectroscopy. **(a)** Positive high bias dI/dV spectrum shows three prominent peaks at 320, 455 and 565 mV. The inset shows the spectrum after removing a third order polynomial background. Spectrum was acquired by spatially averaging the spectra acquired over a 36×21 nm^2 region at $T = 6$ K, $B = 9$ T, $V_s = 0.7$ V, $I_s = 0.35$ nA, $V_{\text{rms}} = 5.6$ mV. **(b)** Calculated DOS from the DFT band structure of (c). Within an energy window: $E_{DP} : E_{DP}+1.1$ eV, three kinks in the calculated DOS are shown with arrows. The energies of these kinks are indicated with dashed lines in the band structure in (c). Calculation was performed on a k-mesh with higher resolution than the k-mesh used in Fig. 4.12. **(c)** DFT calculated bands for a 5 QL slab of Bi_2Se_3. Dashed lines correspond to energies of kinks in the calculated DOS in (b). $E = 0$ is referenced to the Dirac point. Horizontal axis spans the k-space distance from the high symmetry K and M points to the Γ point.

dI/dV spectra. The calculated DOS (Fig. 4.13b) and the data (Fig. 4.13a) qualitatively agree on the overall increasing shape of the spectrum, the existence of three kinks, and the decreasing energy separation between the kinks. Furthermore, by comparing the band structure (Fig. 4.13c) with the calculated DOS (Fig. 4.13b), we can see that the three kinks in the DOS occur at energies where the respective bands turn over, as indicated using dashed lines in Fig. 4.13c. Therefore the qualitative agreement between the DFT and the dI/dV spectra leads us to associate the kinks in dI/dV to the QWS. The subsequent sections provide further justification supporting the presence of QWS in this sample.

4.4.2 Intraband QWS scattering

We further demonstrate the existence of QWS by ascribing the origin of the scattering modes to a wavevector that connects specific parts of the CECs. Dominant scattering modes in STS studies arise from q wavevectors that connect high DOS or nested portions of the CECs. In Bi_2Te_3, at energies away from the Dirac point, scattering modes connect k-states on the CEC that are nested because of hexagonal warping [35, 101, 116, 125, 126]. In analogy, we can expect that scat-

tering modes in Bi_2Se_3 also depend on nesting due to hexagonal warping. Recent ARPES experiments have found that for both the TSS [103], and the 1st QWS [119] the hexagonal warping is maximal in the Γ-K direction. The inset of Fig. 4.14 shows an illustration of the hexagonally warped CECs of the TSS (outer band) and the 1st QWS (inner band) [119]. At the energy shown in the inset, Q_{M-M} is a Γ-M wavevector that connects nested parts of the CEC of the TSS. Because Q_{M-M} connects adjacent M points that are separated by an angle of $\pi/3$, the velocity of the Q_{M-M} mode is the same as the band velocity along the Γ-M direction: $v_{Q(M-M)} = v_{k(\Gamma-M)}$. Furthermore, because the CEC of the QWS1 and the TSS have the same warping, their CECs will evolve in the same way but shifted in energy. Therefore if Q_{M-M} connects nested portions of the CEC for the TSS, then at a higher energy, Q_{M-M} will also connect nested portions of the CEC for the QWS.

From this reasoning, we expect that the band velocity in the Γ-M direction should disperse like a $M-M$ scattering mode ($v_{k(\Gamma\text{-M})} \approx v_{Q(M-M)}$), and that both q_1 and q_2 should be parallel and offset in energy. To verify this hypothesis, in Figure 4.14 we plot the band structure of the SS, QWS1 and QWS2 along the Γ-M direction and superpose the dispersion of q_1 and q_2 (Figs. 4.8, 4.9). Figure 4.14 shows that there is an excellent agreement between the dispersion of q_1 and the TSS band, and between the dispersion of q_2 and the QWS1 band. We computed the band velocities of the DFT bands by fitting each band to a linear dispersion between $k = 0.15 - 0.30$ Å^{-1}. The velocities of the two bands are $v_{\mathrm{SS}} = 1.12 \pm 0.04$ eV Å and $v_{\mathrm{QWS1}} = 1.41 \pm 0.08$ eV Å. These band velocities match well to within error to their respective scattering velocities: $v_1 = 1.28 \pm 0.39$ eV Å $\approx v_{\mathrm{SS}}$, $v_2 = 1.06 \pm 0.32$ eV Å $\approx v_{\mathrm{QWS1}}$.

Discrepancies between the velocities of the DFT and the scattering modes could be caused by the fact that in our model, the QWS is spin-degenerate, in contrast to the spin-polarization of the QWS due to Rashba splitting [119]. The Rashba splitting would split the QWS into two bands, reducing the velocity of one band, thereby bringing its velocity closer to value of v_2 extracted from the data. To account for the spin-polarization, we used $k \cdot p$ theory to simulate the expected q scattering modes from the CECs of a spin-polarized SS and Rashba-split QWS. The simulation is shown in Fig. 4.15. We calculated the CEC for a single band by solving the $k \cdot p$

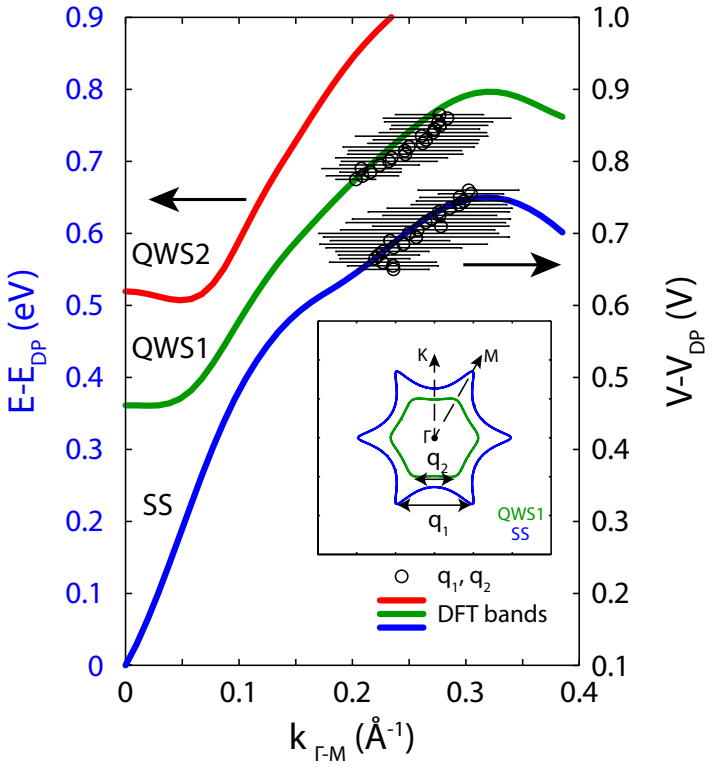

Figure 4.14: Dispersion of scattering modes from the SS and QWS. The QPI wavevectors from Figure 4.8,4.9 are plotted using black circles on top of the DFT bands in the Γ-Mdirection from Fig. 4.13. The DFT bands have been labeled and colored to match the bands in Fig. 4.13. The bands for the SS and the QWS1 match well with the measured scattering modes q_1 and q_2 between $k \sim 0.2 - 0.3$ Å^{-1}. The inset shows a CEC with a warped QWS (green) and a warped SS (blue) that would produce the measured scattering modes indicated using black arrows.

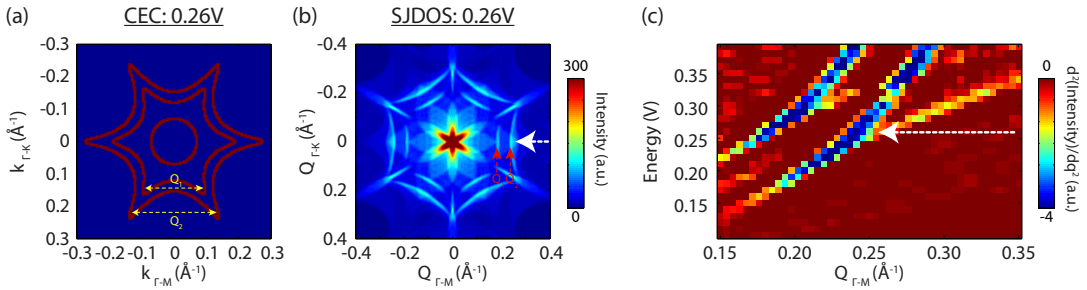

Figure 4.15: $k \cdot p$ **scattering wavevector simulation of SS and QWS. (a)** Constant energy contours of three separate hexagonally warped bands, in agreement with ARPES measurements of band bending induced QWS. The outer band corresponds to the SS, and the inner two bands correspond to the Rashba split, hexagonally deformed QWS. Dashed lines indicate two nesting wavevectors Q_1 and Q_2 between the tips of the SS and the 1st QWS. **(b)** Spin dependent joint density of states of the constant energy contour of (a). The spin matrix element, $T(s_1, s_2) = |\langle \vec{s}_1 | \vec{s}_2 \rangle|^2$ modifies the joint density of states of the constant energy contours and suppresses back-scattering. Two prominent peaks are seen in the Γ-M direction. The two Γ-M peaks match well with the nested wavevectors from the SS and QWS shown in (a). White dashed box corresponds to the region of q space shown in (c) **(c)** Γ-M linecut of the SJDOS as a function of energy and q. The second derivative of the SJDOS intensity is plotted to more clearly show the Q_1 and Q_2 wavevectors. The energy of (a) and (b) is highlighted in the horizontal white dashed box. Two parallel dispersing modes are seen corresponding to the Q_1 and Q_2 wavevectors of (a) and (b).

Hamiltonian in the spin basis [116, 126]:

$$H = v_k(k_x\sigma_y - k_y\sigma_x) + \frac{\lambda}{2}(k_+^3 + k_-^3)\sigma_z \tag{4.1}$$

where $v_k = v_D$ is the Dirac velocity, $\sigma_{x,y,z}$ are the Pauli spin matrices, λ is a phenomenological warping parameter, and $k_\pm = k_x \pm ik_y$. Guided by ARPES which shows that the 1st QWS's two Rashba subsplit bands are warped in the Γ-K direction [119], we offset the eigenstates in energy to create the constant energy contours shown in Fig. 4.15a. We calculated the SJDOS, which accounts for the spin matrix element that depends on the initial and final spin polarization, as shown in Fig. 4.15b,c. Even with the presence of three spin-polarized bands, we found two parallel Γ-M scattering modes, offset in energy, with q wavevectors coming from $M - M$ scattering, and a lack of scattering in the Γ-K direction. All of these observations are consistent with the experimental observations of the q_1 and q_2 modes. The good agreement between our DFT calculations, $k \cdot p$ model and our scattering modes confirms that q_1 and q_2 represent scattering between adjacent $M - M$ portions of the CEC of the SS, and QWS1, respectively.

4.4.3 Choice of Slab Thickness

We further discuss our choice of a 5QL thickness for our DFT calculations.

Our choice of using a 5QL slab of Bi_2Se_3 for our DFT calculations is within the range of acceptable thicknesses for the band bending length scale in Bi_2Se_3. If the QWS are induced by surface band bending, the potential is commonly thought to have the form of a triangular potential [127]:

$$E_0(z) = \begin{cases} \nabla V(z - z_l) + E_0^{\text{bulk}} & z < z_l \\ E_0^{\text{bulk}} & z > z_l \end{cases} \tag{4.2}$$

where $z = 0$ defines the surface, $z > 0$ measures the distance into the material, z_l is the depth of the band bending potential, $\nabla V \sim dV/z_l$, and dV is the magnitude of the energy shift at the surface relative to the bulk (see Fig. 4.10b). A slab of thickness t is effectively a square well approximation to a triangular well potential where $t \sim z_l/2$. In the literature [122], the band bending causing potential gradient $\nabla V \sim 0.75 - 2$ meV Å^{-1}, and has been measured to shift the energy by $dV = 130$ meV [95] to $dV = 230$ meV [127]. This leads to a wide range of possible thicknesses for the extent of the band bending potential, from $z_l = 6.5$ nm to $z_l = 30$ nm. Therefore the range of acceptable slab thicknesses ranges from $t = z_l/2 = 3.25$ nm to $t = 15$ nm, or approximately 3QL to 15QL. Furthermore, the Dirac point was gapped for DFT calculations with $N \leq 4$ QL. Therefore the choice of $N = 5$ QL is the simplest system that preserves the topological character of the SS, while also being within an acceptable experimental range for the band bending depth.

After attributing the q_1 and q_2 modes to the band dispersion of the TSS and the 1st QWS we were able to self-consistently check two quantities to verify our choice of $N = 5$. Firstly, our observation that induced QWS cause a reduction in the band velocity at $k \sim 0.2 - 0.3$ Å^{-1} is independent of our choice of N. To show this, in Fig. 4.16a-c we plot the band structure for different slab thicknesses, and show the velocity extracted from a fit of the TSS. We find that the velocity of the TSS is consistently $v = 1.10$ eVÅ to within $\sim 3\%$ from $N = 5$ to $N = 8$. This demonstrates that the band velocity is reduced for all QL thicknesses. Secondly, we can use the energy scale of

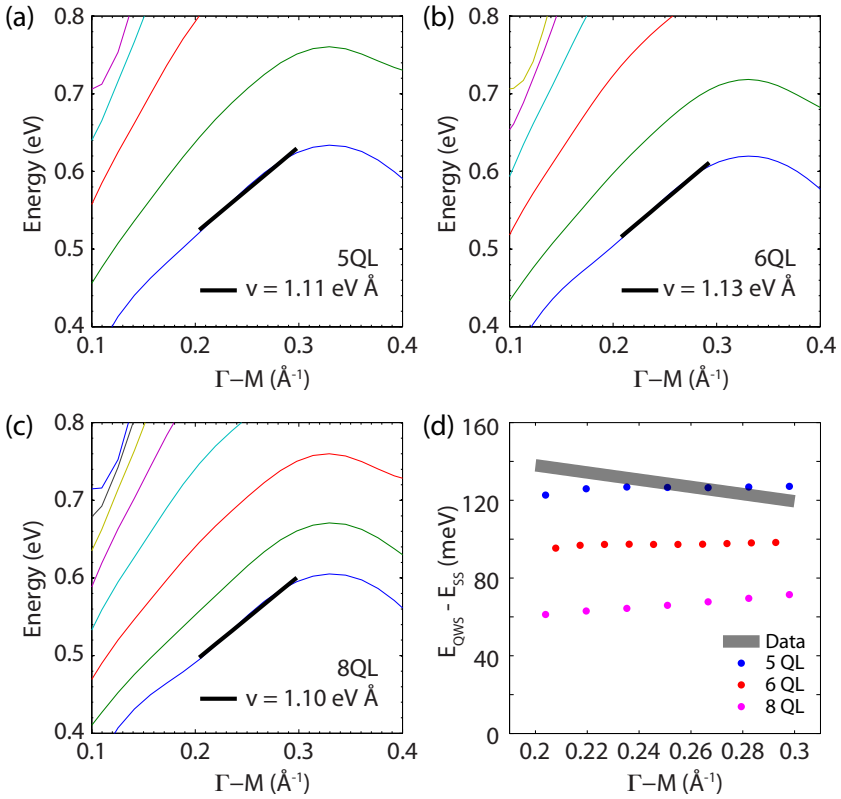

Figure 4.16: DFT parameters for different slab thicknesses. (a)-(c): Band structure in the Γ-M direction at the indicated QL slab thickness, in an energy and k-space range corresponding to the q_1 and q_2 scattering modes in the data. The color of the bands matches the color of the bands in Fig. 4.12 (e.g. blue band is the TSS band, green is QWS1). The black line shows a linear best fit ($E = vk + E_0$) in the range $k = 0.2$ Å^{-1} to $k = 0.3$ Å^{-1}. The velocity extracted from the fit is indicated in the panels. **(d)** Energy separation between the two lowest lying bands: $E_{QWS} - E_{SS}$ at varying slab thicknesses. The energy separation is calculated from panels (a)-(c) in a narrow k range matching the scattering modes from the data. The energy separation between the q_1 and q_2 modes in the data (main text fitted curves in Fig. 4.14) is plotted using a thick grey line.

separation between q_1 and q_2 as another parameter to self consistently verify our choice of N. In Fig. 4.16d we plot the energy separation of the two lowest bands at different slab thicknesses as a function of k (Γ-M), along with the energy separation between the q_1 and q_2 modes from the data. We can see that only the 5QL slab reproduces the energy separation within this window of k. This is further evidence validating our choice of $N = 5$.

4.5 Discussion

Our results have implications on the use of Bi_2Se_3 in potential nanoscale devices. In the idealized bulk band structure calculations of Bi_2Se_3 the TSS merge into the bulk bands at approximately 0.35 eV above the Dirac energy [104]. Significant experimental efforts have focused on tuning the chemical potential within this bulk gap to increase the transport sensitivity to the TSS. While previous work has suggested that the SS might exist at energies beyond the CB minimum in Bi-chalcogenides [125], our results show that extending the energy range of the TSS can be achieved by purposefully inducing QWS. The lack of Γ-K scattering suggests that despite the emergence of QWS, the chiral nature of the SS is preserved, which is of importance for spintronics applications that require the spin-momentum locking of the surface state. This is in line with previous experiments on $Bi_{2-x}Fe_xSe_3$ that found the resilience of the TSS to Fe-doping [89, 90]. However, the reduced band velocity of the SS at these energies could lead to a reduction in the mobility of the carriers. Furthermore, while the TSS remains quantized, transport will still have to disentangle the response of the TSS from the trivial QWS. Further transport experiments on QWS induced Bi_2Se_3 are required to deduce whether inducing QWSs is an effective alternative to tuning the chemical potential in Bi_2Se_3.

In summary, we report STS measurements on bulk crystals of $Bi_{2-x}Fe_xSe_3$. We observed extreme defect inhomogeneity, with macroscopic phase separation into regions with no Fe atoms, low Fe concentration, and clusters of Fe atoms. This dopant inhomogeneity is likely due to nonuniform local growth conditions during the crystal growth process. We were able to use a specific Fe defect as a high amplitude scattering center. Due to the presence of QWS, we observed two scattering modes that connect M-M points of the CEC of the TSS and the 1st QWS. The scattering velocity is 3× smaller than the velocity at the Dirac point, as reproduced by our DFT calculations. Our results suggest that inducing QWSs can cause the TSS to remain quantized from the bulk, and provides important spectroscopic information for future device applications.

5

Charge order in $Bi_2Sr_{2-x}La_xCuO_{6+\delta}$

Charge ordering in the cuprates, as observed at the surface via STM, and in the bulk via neutron or x-ray scattering, has never been fully reconciled. In this chapter, we detail experiments performed on La-doped Bi-2201, in conjunction with collaborators using bulk sensitive probes, to look for charge ordering in the cuprates. Some of the results in this chapter were published in Ref. [28]: Comin, Frano, Yee et al., **Science 343**, 390 (2014).

5.1 Introduction

Understanding the mechanism of superconductivity in the cuprate superconductors has been complicated by the multiple observations of charge, spin, and structural modulations. The effect of these modulations on the the electronic structure of cuprates, and whether it is related to the mysterious pseudgap phase has been actively studied for the past three decades [128]. Owing to differences between the multiple cuprate compounds, certain techniques are better suited for studying specific compounds, leading to a poor understanding of what is ubiquitous to the cuprate family. For example, some experiments have shown signatures of charge ordering, such as the $4a_0$ stripe ordering in the bulk of La-based cuprates [129, 130]. Similarly, x-ray scattering experiments on the bulk of Y-based cuprates also found evidence for charge ordering with $\sim 3.3a_0$ periodicity [131, 132]. In contrast to the prior bulk measurements of charge order (CO), STM measurements on the surface of Bi and Cl based cuprates have long reported evidence of CO [133–138]. Whether the surface observed CO via STM is related to the bulk observed ordering in La or Y cuprates remains an open question.

Single layer Bi-2201 is well suited for studies using low-T STM because of its easily cleavable surface, and the ability to probe the PG state at relatively low temperatures [139, 140]. While the bilayer compound Bi-2212 has been better studied than the single layer Bi-2201 compound, many of the previous experiments on Bi-2201 have focused on using Pb-doped Bi-2201 [137, 141, 142]. Pb-doping serves to suppress the supermodulation that could lead to bilayer-splitting, Umklapp bands [143], or modulate the pseudogap energy on a local scale [144]. However, Pb, which substitutes for Bi, typically overdopes the system [139, 140] (although it can bring Bi-2201 in the extreme underdoped region [145]). On the other hand, La, which substitutes for Sr, can continuously span a wide range of the superconducting dome, from $p = 0.10$ in the underdoped regime to $p = 0.19$ in the overdoped regime [139, 140, 146]. This makes non-Pb doped Bi-2201 ($Bi_2Sr_{2-x}La_xCuO_{6+\delta}$) ideal for studying the underdoped regime, despite the possible structural reconstructions and their electronic effects. While $Bi_2Sr_{2-x}La_xCuO_{6+\delta}$ has been studied in the optimal and overdoped regime using STM [147], the deeply underdoped regime ($p \leq 0.12$),

with its electronic complexity [23], has not been studied via STM, leaving open the question of whether a CO-state exists in this strong pseudogap regime.

5.1.1 Summary of Results

In this chapter we report on our STM studies of UD15K $Bi_2Sr_{2-x}La_xCuO_{6+\delta}$ near the hole doping $p \sim 1/8$. We acquire topographic images of a $\lambda = 4a^*$ commensurate supermodulation in Bi-2201, which differs from the, $\lambda \sim 5a^*$ supermodulation in the parent Bi-2201 compound [148], and incommensurate supermodulation in Bi-2212 [144]. We observe another incommensurate $\lambda \approx 8.1a^*$ superstructure which does not have a measureable temperature dependence (shown in Fig. 5.4), in contrast to LEED results that report a strong temperature dependence of a superstructure wavevector [149]. Our STS measurements of $Bi_2Sr_{2-x}La_xCuO_{6+\delta}$ find a non-dispersive CO wavevector of $q_{CO} = 0.248 \pm 0.012$ r.l.u., which is in agreement with the CO wavevector measured from the bulk using resonant X-ray scattering (REXS). Combined with the temperature dependent REXS measurements, this work provides the first crucial verification that surface CO measured via ARPES and STM is related to the bulk CO measured by neutron and X-ray scattering, and suggests an intimate link between the CO state and the pseudogap phase.

Some of the work in this chapter was published in: *Comin, Frano, Yee et al.*, "Charge Order Driven by Fermi-Arc Instability in $Bi_2Sr_{2-x}La_xCuO_{6+\delta}$", **Science 343**, 390 (2014) [28].

5.1.2 Experimental Methods

Bulk single crystals of $Bi_2Sr_{2-x}La_xCuO_{6+\delta}$ ($x = 0.8$, $p \approx 0.115$, $T_c = 15$ K) were cleaved in-situ at $T \sim 40$ K and immediately inserted into the STM. The samples were prepared in the laboratory of Dr. H. Eisaki in the National Institute of Advanced Industrial Science and Technology, Tsukuba, Japan. Prior to STM studies, our collaborators measured the T_c of the crystals via in-plane resistivity and magnetic susceptibility measurements. The hole doping p was then determined from the T_c using Ref. [146]. Complementary resonant X-ray scattering (REXS) and ARPES experiments were performed under the supervision of Prof. A. Damascelli at the Univer-

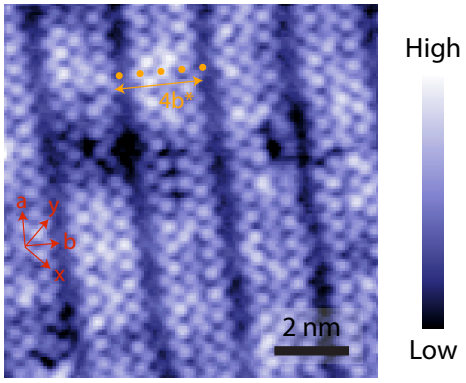

Figure 5.1: High resolution topography of $Bi_2Sr_{2-x}La_xCuO_{6+\delta}$. Topographic image acquired over a 10×10 nm^2 region ($V_s = -1.2$ V, $I_s = 100$ pA, $T = 4.5$ K), and post-corrected for scan-piezo drift [150, 151]. Orange dots are overlaid to represent the atomic positions. The supermodulation has a periodicity $\lambda = 4b^*$ in the b direction. Square lattice unit vectors (x, y) and orthorhombic unit vector (a, b) are indicated in red.

sity of British Columbia [28].

5.2 Structural reconstructions in $Bi_2Sr_{2-x}La_xCuO_{6+\delta}$

5.2.1 Topographies of $Bi_2Sr_{2-x}La_xCuO_{6+\delta}$

Cleaving the $Bi_2Sr_{2-x}La_xCuO_{6+\delta}$ crystal exposed a clean BiO layer and the surfaces subsequently studied were atomically flat over long (> 100 nm) length scales. Figure 5.1 shows high resolution topography acquired over a 100×100 Å^2 region. Bi atoms are clearly resolvable in Fig. 5.1, and are arranged in a square lattice along the Cu-O lattice directions (x, y), separated by a tetragonal lattice constant of $a_0 = 3.86$ Å. Along the b direction that is 45 degrees between the (x,y) directions, we observe a periodic superstructure with a periodicity of $\sim 4 \times \sqrt{2}a_0$. Orange circles have been overlaid in the b direction on top of Bi atoms to indicate the superstructure periodicity. Intriguingly, compared to the supermodulation (SM) in the parent Bi-2201 compound [148], OP Bi2201 [147], or in Bi-2212 [144] the supermodulation in the $Bi_2Sr_{2-x}La_xCuO_{6+\delta}$ samples studied here are missing a similar characteristic "dollar-sign ($)" modulation. Instead, the modulation shows up as a "zig-zag" crease on the surface.

To more accurately measure the periodicity of the structures seen in real space, we take the

Fourier transform of topographic images over large fields of view. Figure 5.2a shows a topographic image with its associated Fourier transform image in Fig. 5.2b. By taking the Fourier transform of the topographic image, periodicities with wavevector λ in the topographic image are represented by high intensity peaks at wavevectors $Q = 2\pi/\lambda$. Following Ref. [151], a clear peak is seen at a wavevector $Q_{\text{Bragg}} = 2\pi/a_0$ in the Cu-O bond directions (x,y). In the a direction, a structural peak is visible at $Q_{\text{ortho}} = 2\pi/a^*$, which is due to an orthorhombic distortion that is caused by an asymmetric expansion between the x and y directions [151]. The true unit cell is then orthorhombic, rotated 45 degrees relative to the tetragonal unit cell, and is spanned by vectors along the (a,b) directions, and where $a^* = b^* = \sqrt{2}a_0$ is the orthorhombic unit cell [151]. Lastly, supermodulation peaks (green circles) are observed along the b direction, perpendicular to the orthorhombic distortion. However, the signature of the SM also shows up as satellite peaks between the orthorhombic peak (0,1) and the Bragg peak (1,1). Measuring the periodicity from the satellite peaks avoids the isotropic long wavelength $Q = 0$ background that obscures the SM. A linecut through the satellite peaks (blue arrow at the bottom box), is shown in Fig. 5.2c. Now, the SM wavevector can be precisely determined: $Q = 2\pi/4a^*$. In addition to the SM wavevector, an additional series of satellite peaks are seen with a wavevector of $Q = 2\pi/8a^*$, indicated with orange stars. This leads us to conclude that there exist two supermodulation wavevectors, $Q_1 = 2\pi/4a^*$, and $Q_2 = 2\pi/8a^*$, both with distortions perpendicular to the orthorhombic distortion.

Surprisingly, the periodicities of superstructures measured in the Bi-based cuprate family varies in the literature. In the parent compound, the periodicity of the supermodulation was found to be $\lambda = 5b^* \approx 2.7$ nm [148], and in Bi-2212 the periodicity of the supermodulation was found to be $\lambda = 4.8b^* \approx 2.6$ nm [144]. However, STM topography on optimally doped $Bi_2Sr_{2-x}La_xCuO_{6+\delta}$ found a superstructure with modulation $\lambda = 2.2$ nm $\approx 4b^*$ [152], in agreement with our Q_1 modulation. The prominence of the '\$' superstructure in Refs. [144, 148] seems to be related to a $\sim 5b^*$ modulation, whereas in our work and Ref. [152] where $\lambda_2 \sim 4b^*$, the superstructure is characterized by the "zig-zag" pattern. In all of the previous STM references [144, 148, 152] however, the $Q_2 = 2\pi/8a^*$ modulation has not been previously observed. But

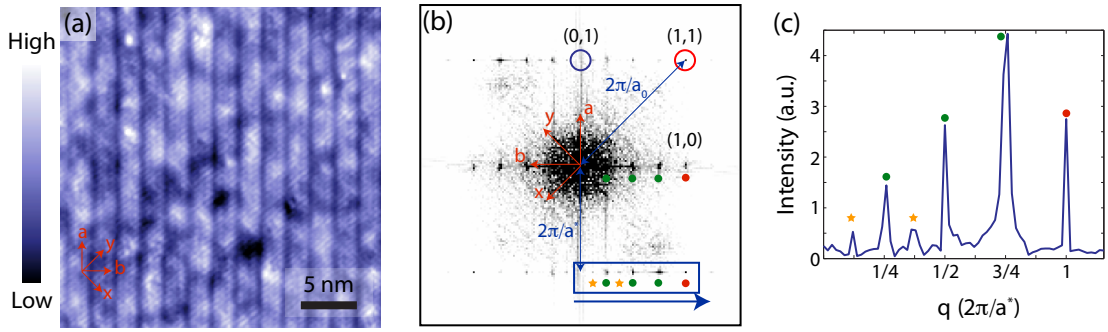

Figure 5.2: Topography and Fourier transform topography of $Bi_2Sr_{2-x}La_xCuO_{6+\delta}$. (a) Topography of $Bi_2Sr_{2-x}La_xCuO_{6+\delta}$ over a 29×29 nm^2 region ($T = 4.5K$, $V_s = 200$ mV, $I_s = 20$ pA). Topographic image has been corrected for experimental noise due to scan-piezo drift [150, 151]. Red direction arrows have been superposed to match those shown in (b). **(b)** Fourier transform of topography shown in (a). Red circle identifies the Bragg peak and blue arrows denote the distances in reciprocal space. Green circles and orange stars denote the periodicities of the Q_1 and Q_2 wavevectors respectively. Red arrows denote the directions in Fourier space related to those directions shown in (a). A coordinate system has been superposed in the (a, b) coordinate system where $2\pi/a^* = 1$. **(c)** Intensity linecut through Fourier transform of (b). Linecut taken from (b) from the point (0,-1) towards (1,-1) along the blue arrow, inside the rectangular blue box box of (b).

Reference	Compound	λ_1	λ_2	T-dep?
Reported here	La-Bi2201 UD15K	$4b^*$; "zig-zag"	$8b^*$	No
Machida *et al.* [152]	La-Bi2201 OP34K	$\sim 4b^*$; "zig-zag"	None	No
Shan *et al.* [148]	La-Bi2201	$\sim 5b^*$; '$'	None	No
Slezak *et al.* [144]	Bi-2212	$\sim 4.8b^*$; '$'	None	No
Rosen *et al.* [149]	La-Bi2201 UD15K	$\sim 4b^*$	$8b^*$ at low T	Yes for λ_2

Table 5.1: Properties of the reported superstructures in Bi-2201.

there has been a temperature dependent modulation with a low-T periodicity of $\lambda = 8a^*$ that was observed by low energy electron diffraction (LEED) measurements [149] which could coincide with our Q_2 wavevector. To summarize the literature, we compiled the various supermodulation observations in Table 5.1.

5.2.2 Temperature dependence of supermodulation

To investigate whether the measured Q_1 and Q_2 correspond to the wavevectors recently seen in LEED measurements [149], we performed T-dependent topography. In the LEED measurements of Ref. [149], $Q_2 = 2\pi/\lambda_2$ was found to have a strong temperature dependence with $\lambda_2 = 8a^*$ at

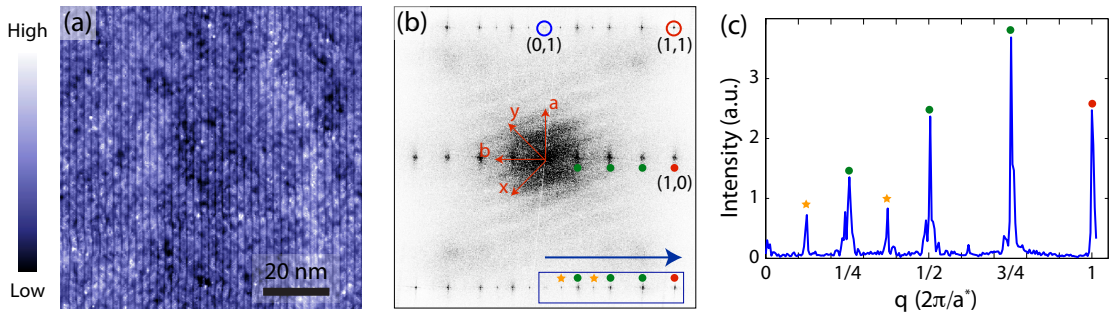

Figure 5.3: High temperature topography of $Bi_2Sr_{2-x}La_xCuO_{6+\delta}$. **(a)** Topography of $Bi_2Sr_{2-x}La_xCuO_{6+\delta}$over a 90×90 nm^2 region at $T = 30$ K ($V_s = -200$ mV, $I_s = 10$ pA). Topographic image has been corrected for experimental noise due to scan-piezo drift [150, 151]. **(b)** Fourier transform of topography shown in (a). Red circle at (1,1) identifies the Bragg peak, and blue circle at (0,1) identifies the orthorhombic peak. Green circles and orange stars denote the periodicities of the Q_1 and Q_2 wavevectors respectively. **(c)** Intensity linecut through Fourier transform of (b). Linecut was symmetrized about the orthorhombic peak, and taken from the orthorhombic peak towards the Bragg peak as illustrated using the rectangular box of (b).

$T = 6$ K, and increasing to $\lambda_2 \approx 12.1a^*$ at $T \geq 120$ K [149]. We therefore focused on studying the Q_2 peak in our data, evidenced by satellite peaks from the orthorhombic peak. Figure 5.3 shows an example of a topographic image, acquired over a large field of view to maximize Fourier-space resolution, at $T = 30$ K. As in Fig. 5.2, Q_1 and Q_2 are seen as satellite peaks between (0,1) and (1,1) (shown in blue box with blue indicated arrow). We measure $Q_1(T = 30\text{ K}) = 2\pi/4a^*$, and $Q_2(T = 30\text{ K}) \approx 2\pi/8a^*$, as shown in the Fourier linecut in Fig. 5.3c. We summarize the wavevectors Q_1 and Q_2 measured from a series of topographies with different tips, acquired between 6 K and 40 K in Figure 5.4. The results shown in Fig. 5.4 demonstrate that in contrast to Ref. [149], we did not observe a meaningful temperature dependence of the Q_2 peak. In fact, at $T = 40$ K, our highest measured temperature, $Q_2 = 2\pi/a^* \times 0.123 \pm 0.005$, whereas from Ref. [149], $Q_2 \approx 2\pi/a^* \times 0.101$ at $T = 40K$. This corresponds to a wavelength mismatch of $\lambda_{2,\text{STM}} = 8.1 \pm 0.3a^* = 44.2 \pm 1.8$ Å vs. $\lambda_{2,\text{LEED}} \approx 9.9a^* = 54$ Å, well outside of the error bars of our measurement.

The mismatch in the temperature dependence of the incommensurate Q_2 wavevector between STM, and LEED, which are both surface sensitive probes, is surprising. One possibility, is that the discrepancy is due to the different vacuum environments between the LEED measurements

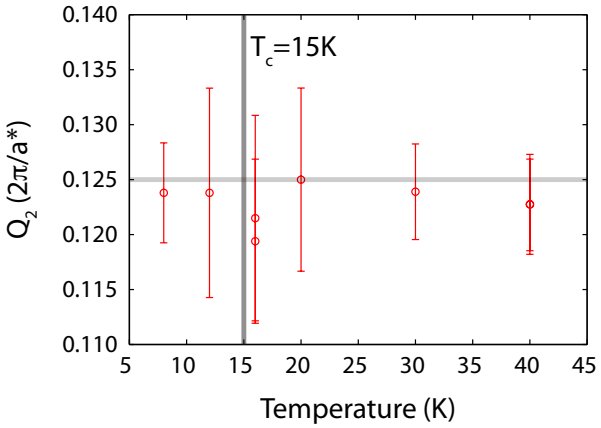

Figure 5.4: Temperature dependence of Q_2 wavevector. Q_2 wavevectors were extracted from the Fourier transforms of topographies taken at different temperatures over similar but not identical regions of $Bi_2Sr_{2-x}La_xCuO_{6+\delta}$. Junction resistances were typically R_J $\sim>$ 1GΩ. A vertical gray bar indicates the superconducting T_c in this sample, and the horizontal gray bar indicates the wavevector corresponding to $\lambda = 8a^*$. Topographic images were corrected for scan-piezo drift. Fourier transform linecuts were taken from the symmetrized linecut between the orthorhombic peak and the Bragg peak. Error bars represent the pixel resolution in Fourier space, which was determined by the pixel resolution of the topographic image.

and the STM measurements. In our STM experiments, the sample is cleaved in-situ at cryogenic vacuum, surrounded by a cryostat that is bathed in liquid helium. The cryogenic temperatures of our environment allow us to maintain a cryogenic ultrahigh vacuum over the span of months. Meanwhile, the LEED experiments were performed in vacuum chambers requiring line-of-sight access at pressure $P \sim 5 \times 10^{-11}$ torr [149], but in a room temperature cryostat. The temperature dependence of Q_2 could then be related to different temperature dependent surface effects between the two systems.

5.3 Scanning tunneling spectroscopy of $Bi_2Sr_{2-x}La_xCuO_{6+\delta}$

5.3.1 Spatially resolved spectroscopy

Having characterized the surface modulations in $Bi_2Sr_{2-x}La_xCuO_{6+\delta}$, we performed spatially resolved tunneling spectroscopy to image the electronic density variations. Figure 5.5 displays representative dI/dV spectra of $Bi_2Sr_{2-x}La_xCuO_{6+\delta}$ over different energy ranges. Fig. 5.5a shows a sudden increase in dI/dV at $V = -1.3$ V and $V = +1.6$ V corresponding to the onset of two

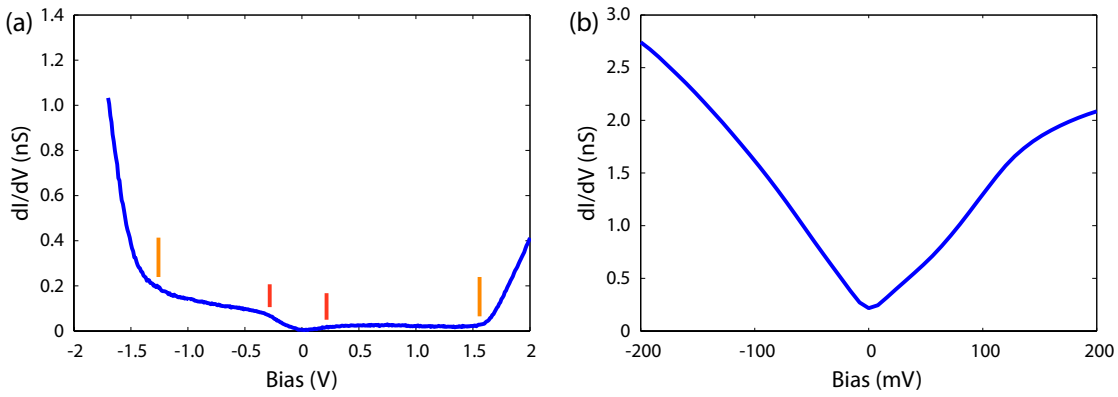

Figure 5.5: dI/dV **spectroscopy of** $\mathbf{Bi_2Sr_{2-x}La_xCuO_{6+\delta}}$**. (a)** High bias spectroscopy. Data acquired at $V_s = -1$ V, $I_s = 100$ pA, $V_{\text{rms}} = 7$ mV, $T = 8.4$ K. Orange markers indicate the onset of additional bands at $V = 1.6$ V and at $V = -1.3$ V. Red markers indicate a E_F centered suppresion in dI/dV. **(b)** Low bias spectroscopy. Data acquired at $T = 9$ K, $V_s = -200$ mV, $I_s = 250$ pA, $V_{\text{rms}} = 8.5$ mV. Each spectrum is a well-averaged single-point spectrum that is representative of the typical surface spectra.

different bands. The band onset at -1.3 V roughly agrees with a similar rise in dI/dV at negative biases in Bi-2212 [153, 154]. The increase in dI/dV in the unoccupied states at 1.6 V is likely related to the onset of Bi or O bands predicted at $E_F + 2$ eV [155]. Fig. 5.5b shows a low bias spectrum illustrating the DOS near the Fermi level. The spectrum shows a suppression in the DOS near the Fermi level which is $\Delta \sim 100$ mV, which is of the correct order for highly underdoped systems [156].

We performed multiple spatially resolved scanning tunneling spectroscopy maps at varying temperatures, an example of which is shown in Fig. 5.6. The topographic image in Fig. 5.6a shows the presence of the Q_1 supermodulation throughout the large field of view. However, the supermodulation is absent from the dI/dV map shown in Fig. 5.6b. In fact, the most prominent feature is an x and y oriented modulation, shown in Fig. 5.6b, and the inset of Fig. 5.6b, that has been described as a checkerboard [133], fluctuating stripes [138], or a charge density wave (CDW) [137]. The FT-dI/dV map shown in Fig. 5.6c shows a prominent peak in the direction of the Cu-O bonds at a wavevector smaller than the Bragg wavevector. Experiments in Bi-based cuprates have attributed this modulation in dI/dV to a static charge ordering that is dopant dependent [137]. In Fig. 5.7 we show an additional two dI/dV maps taken with a different area, tip, and temperature, which also shows the prominence of the CO wavevector along the Cu-O

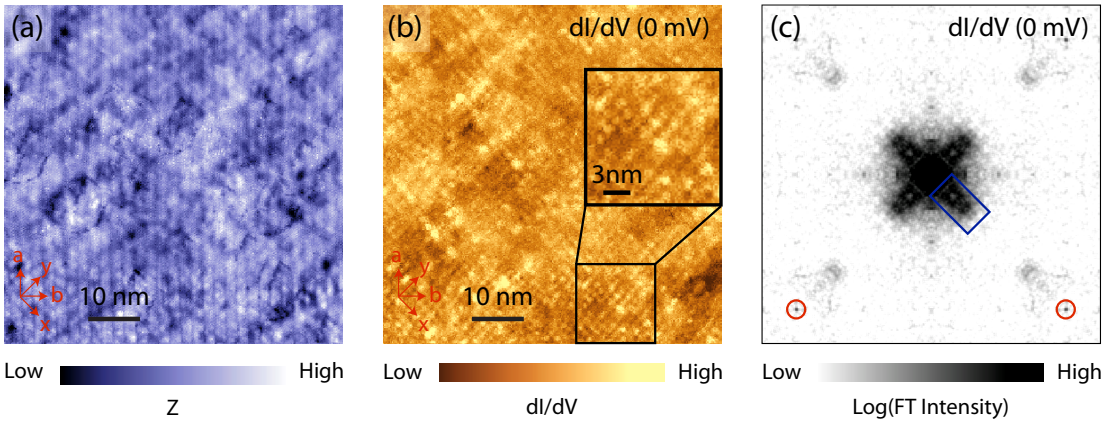

Figure 5.6: Scanning tunneling spectroscopy of $Bi_2Sr_{2-x}La_xCuO_{6+\delta}$. **(a)** Topography, **(b)** $dI/dV(V{=}0)$, and **(c)** Fourier transform $dI/dV(V{=}0)$ map of a 65 $\times$ 65 nm^2 region of $Bi_2Sr_{2-x}La_xCuO_{6+\delta}$. Inset in (b) is a magnification of a 15 $\times$ 15 nm^2 area showing the charge order modulation. Red circles in (c) highlight the Bragg periodicity in the x and y directions. Blue circle highlights the peak due to the charge order shown in (b). Data from a-c were acquired simultaneously at: $T = 40$ K, $V_s = -200$ mV, $I_s = 200$ pA, $V_{\rm rms} = 14.1$ mV. Topographic image (a) and dI/dV map (b) were corrected for scan-piezo drift. Fourier transform dI/dV image of (c) was 4-fold symmetrized to better resolve the CDW periodicity.

bond direction.

Non-dispersive behaviour of CO peak

To verify that the dI/dV modulation is actually a static CO rather than modulations due to disorder induced quasiparticle interference [157], we show the energy dependence of the FT-dI/dV map in Fig. 5.8. In Fig. 5.8a we show the Fourier linecut taken along the CO bond direction as a function of energy. The color plot clearly shows the presence of a modulation at $Q \sim 0.25$ r.l.u., over a large range of energy. Here we define 1 reciprocal lattice unit (r.l.u) $= 2\pi/a_0$ for convenience. The background subtracted linecuts in Fig. 5.8c more clearly show that the peak exists over a wide range of energy, and does not disperse more than ~ 0.02 r.l.u.. Because the $4a_0$ peak is nondispersive, the modulations in dI/dV observed in Figs. 5.6, 5.7 is a static charge order. The charge order seen in dI/dV, as shown in Fig. 5.8, is independent of STM matrix element effects, as shown by the Z^+ normalized map in Fig. 5.9. Our observation of a static charge order is similar to the observation of static charge order between 0 - 50 mV in Bi-2212 [158], and static charge order between 5 - 35 mV in Pb-doped Bi-2201 [137].

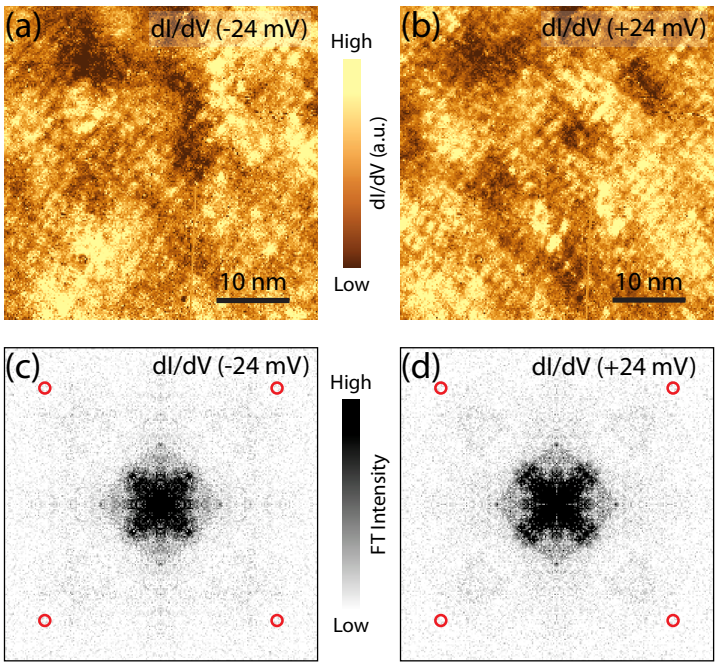

Figure 5.7: Scanning tunneling spectroscopy of $Bi_2Sr_{2-x}La_xCuO_{6+\delta}$. **(a)** dI/dV (V = -24 mV). **(b)** dI/dV (V= +24 mV). **(c)** Fourier transform dI/dV (V = -24 mV). **(d)** Fourier transform dI/dV (V = +24 mV). Red circles in (c), and (d) indicate the location of the Bragg peaks in Fourier space. Fourier transforms have been 4-fold symmetrized along the crystal directions to better show the CDW periodicity. A subset of this data was used in *Comin et al.* (with the color bar of the dI/dV images inverted) [28]. Data acquired at T = 9 K, V_s = −200 mV, I_s = 250 pA, $V_{\rm rms}$ = 8.5 mV over a 43 × 43 nm^2 region as shown in (a) and (b).

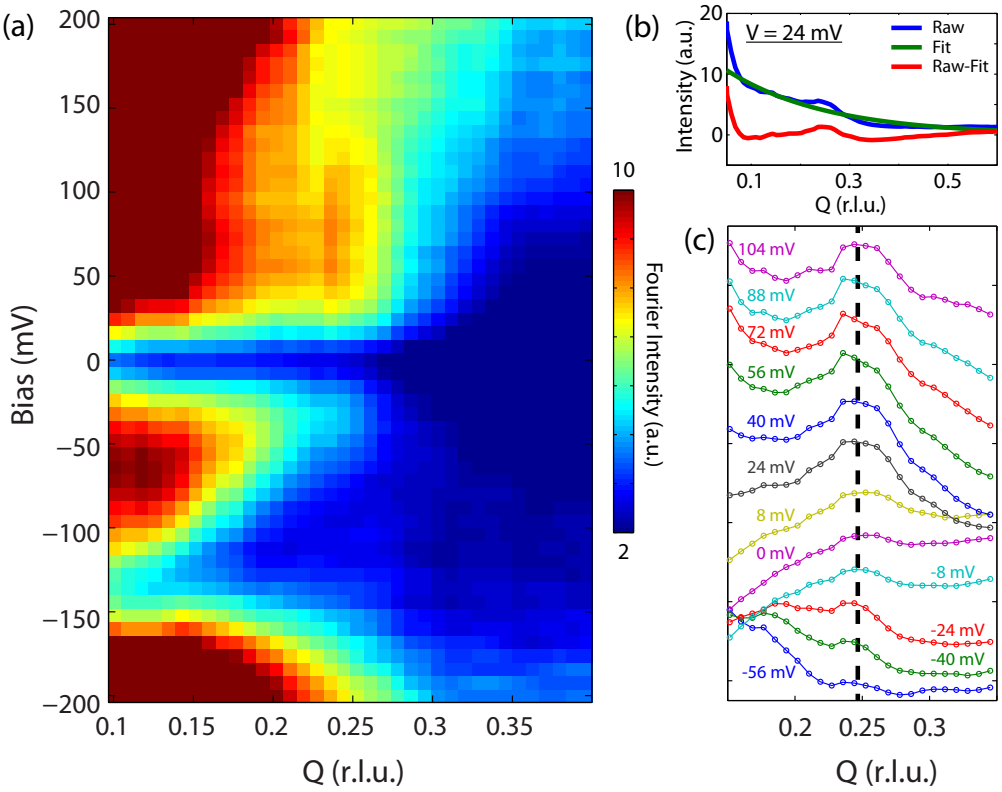

Figure 5.8: Fourier linecut showing $Q \sim 1/4$ peak. (a) Fourier linecut from $Q = 0$ along the Bragg direction as indicated in Fig. 5.7 **(b)** Low Q background subtraction. The data from the $V = +24$ mV linecut (blue) was exponentially fit to give the background shown in green. The CO peak is more clearly shown by taking the difference between the data and the fit, as shown in red. **(c)** Fourier intensity along the Bragg direction at specified energies (labeled in figure). Vertical dashed line indicates $Q \sim 0.248$. To obtain the individual Q dependent profiles, an exponential background was subtracted from the data shown in (a). All profiles were subtracted by the exponential fitted to the $V = 24$ mV profile that is shown in (b). Data taken from the Fourier STS map shown in Fig. 5.7.

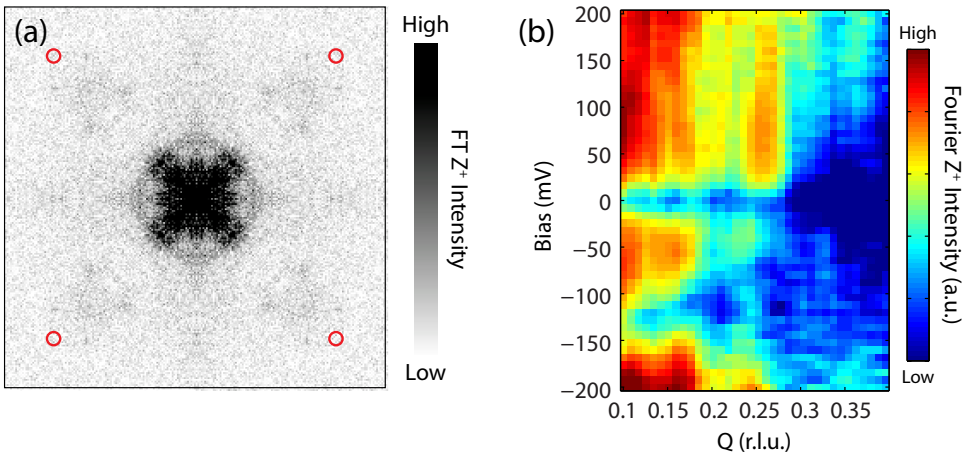

Figure 5.9: Fourier space signature of CO using Z^+ normalization. (a) Fourier transform of $Z^+(\vec{r},V) = dI/dV(\vec{r},V)/dI/dV(\vec{r},200\text{ mV})$. Red circles are placed over the Bragg location. Z^+ map was four-fold symmetrized to better display Q space signatures. **(b)** Fourier linecut of Z^+ map shown in (a) along the symmetrized x direction.

5.3.2 CDW ordering at $q = 1/4$

Having established the existence of CO in this system, we now move to precisely determining the magnitude of the CO wavevector. In other studies of Bi-based cuprates, the CO wavevector was found to be $Q = 0.3$ r.l.u. in UD45K Bi-2212 [158], 0.15 r.l.u. to 0.23 r.l.u. over a range of dopings in Pb-doped Bi-2201 [137], 0.2 r.l.u. in OP32K La-Bi2201 [147, 152, 159], and 0.25 r.l.u. in UD29K La-Bi2201 [160]. We chose to measure the wavevector primarily from the dI/dV modulations at $V = 24$ mV, because we found the CO wavevector to be most pronounced in Fourier space at that energy, in agreement with similar measurements [158]. For $V = 24$ mV, the Fourier linecut along the Cu-O bond direction is shown in Fig. 5.10. The center of the Gaussian is an extracted fit parameter: $q_0 = 0.248 \pm 0.002$ r.l.u., where the error bar is the 95% confidence interval of the fit. However, the dominant uncertainty in determining the CO wavevector is the range of CO wavevectors at different energies. From the linecut in Fig. 5.8c, we can see that for some energies, the maxima in the Fourier linecuts are located at $q = 0.236$ r.l.u. (e.g. V = 72 mV). We therefore take the separation between the center from the fit, and this point to be the error in our measurement of $q_{\text{CO}} = 0.248 \pm 0.012$. From the fitting parameters shown in Fig. 5.10, the linewidth of the CO peak is $w = s/\sqrt{2}$, for the fitting parameter $s = 0.044 \pm 0.004$ r.l.u..

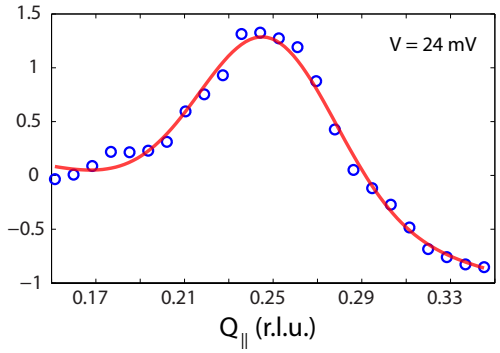

Figure 5.10: Determining the Q_{CDW} periodicity. Example of fitting procedure for Fourier intensity profile $I(q, V = 24\mathrm{mV})$. Blue circles represent the data taken after removing an exponential background, as described in Fig. 5.8. The red profile is the best fit to a Gaussian profile with a linear background: $I = A\exp(-(q-q_0)^2/s^2) + aq + b$. Fit parameters extracted from the best fit are: $q_0 = 0.248 \pm 0.002$, $s = 0.044 \pm 0.004$, where the fit parameter error bars represent the 95% confidence interval of the fit. The separation between the pixels in Q space is 0.0075 r.l.u.

The FWHM can then be evaluated using the fact that for a Gaussian, FWHM $= 2\sqrt{2\ln 2}w = 0.073 \pm 0.07$ r.l.u., which leads to a correlation length as reported in Ref. [28] of $\xi = 28 \pm 2$ Å.

5.3.3 Evidence from REXS and ARPES

Our measurement of the CO wavevector $q_{\mathrm{CO}} = 0.248 \pm 0.01$ in UD15K $Bi_2Sr_{2-x}La_xCuO_{6+\delta}$ samples was corroborated by independent measurements on the same crystals by our collaborators at the University of British Columbia, and the Max Planck Institute for Solid State Research [28]. On the same $Bi_2Sr_{2-x}La_xCuO_{6+\delta}$ compounds and over a larger range of doping, resonant x-ray scattering (REXS) experiments were able to probe variations in the electronic density profile in the CuO_2 planes. In REXS, the photon energy is tuned to be in resonance with the absorption of specific elements, allowing atomic sensitivity to electronic density variations in the bulk [28, 130]. At the same doping (UD15K), REXS measured a $q_{\mathrm{CO}} = 0.265 \pm 0.01$ [28], in agreement with our measurement. Because REXS is a bulk probe, the coincidence of these two wavevectors demonstrates that the surface CO measured in STM is the same bulk CO measured via REXS. Furthermore, ARPES measurements in these UD15K crystals showed that the $Q_{\mathrm{CO}} \approx 0.25$ r.l.u. wavevector matches to the k-space distance between the hot spots of the Fermi arcs ($Q_{\mathrm{HS}} = 0.255 \pm 0.1$) [28]. The combination of these surface and bulk probes of the same

Bi-based cuprate crystals at the same doping is strong empirical evidence for a $\lambda = 4a_0$ surface and bulk charge order at $x = 1/8$ doping. This CO is related to the wavevector that connects the hot-spots of the Fermi arcs in the UD regime, as opposed to antinodal nesting as previously assumed [132, 137, 161].

5.4 Discussion

The doping dependence of the CO wavevector measured in Ref. [28], and recent work on the bilayer compound [158], verify that the surface CO extensively studied previously [133, 134, 136–138, 162–164] is not restricted to some surface phenomenon, but represents a CO that pervades into the bulk. The coincidence of the CO wavevector in doping with the $q \sim 0.25$ wavevector at $x = 1/8$ in La-based cuprates [129, 130], and in Y-based cuprates [132], suggests that the CO is ubiqutous throughout the cuprate family. Furthermore, the temperature dependent measurements of $Bi_2Sr_{2-x}La_xCuO_{6+\delta}$ by our collaborators [28] shows that the onset temperature of the CO is coincident with the pseudogap temperature measured by NMR [28, 165]. This suggests a close relationship between the ubiquitous CO observed and the PG phase. While these findings still leave open the question of the mechanism driving superconductivity or charge ordering, the universality of the CO reported here provides important insight into understanding the cuprates.

6

Nematic Order in Bi-based Cuprates

This chapter discusses experiments that we performed investigating the experimental validity of broken electronic intra-unit cell rotational symmetry in Bi-2201. We conducted high resolution STS maps under varying conditions to verify the analysis techniques of the work by Lawler *et al.* [150].

6.1 Introduction

6.1.1 Intra-unit cell electronic nematicity in cuprates

Understanding whether the pseudogap phase in high-T_c cuprates has any associated broken symmetries is key to unraveling the pseudogap phases's mysterious origin [166, 167]. Recent experiments have found evidence for an electronic intra-unit cell nematic order [150], where the electronic states break rotational symmetry but preserve the translational symmetry of the lattice [150, 168]. These experiments used the high-spatial resolution of STS to image rotational symmetry breaking on the atomic length scale. In particular, Lawler *et al.* [150] found evidence for an electronic inequivalence between the states at the oxygen sites in the x and y directions. This four-fold symmetry breaking, where the electronic order preferentially chooses one direction over the other, was found to scale with the pseudogap energy, and is therefore in agreement with other observations of broken symmetries that scale with the pseudogap temperature [169–171].

However, there is still some debate on the experimental validity of the claimed observation of electronic intra-unit cell nematicity in the cuprates [172], and additional STM experiments have been conducted to investigate the issue further [172, 173]. Different experiments have come out against and in support of the observed nematicity. According to one paper, the nematicity is likely due to tip structure [172], while another paper has supported the observation of nematicity by verifying the high spatial resolution of the technique in Lawler *et al.* [173]. In this chapter we provide additional insight into the experimental validity of Lawler *et al.*'s observation of electronic nematicity [150] by performing high-resolution STS experiments under a variety of experimental conditions.

6.1.2 Experimental definition of intra-unit cell nematicity

Lawler defined an intra-unit cell nematic parameter of variable M, as [150]:

$$O_N(M) = Re[\tilde{M}(Q_y)] - Re[\tilde{M}(Q_x)] \tag{6.1}$$

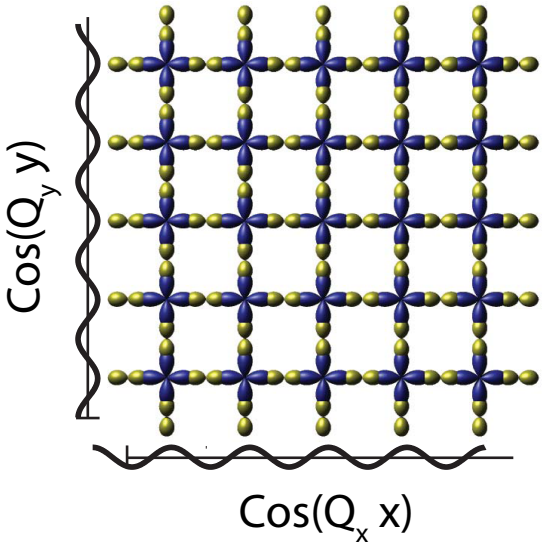

Figure 6.1: Real-space interpretation of Nematic order parameter. The real components of the Bragg periodicities Q_x and Q_y are interpreted as the periodicity that is in-phase with the Cu atoms. Figure adapted from Ref. [150].

where $Q_{x,y}$ are the Bragg peaks in the x and y directions, and $\tilde{M}$ is the complex-valued Fourier transform of M. Figure 6.1 illustrates the real-space interpretation of Eqn. 6.1. Lawler *et al.* showed that within each unit cell,

$$Re[\tilde{M}(Q_x)] = M_{\mathrm{Cu}} + M_{\mathrm{O}_y} - M_{\mathrm{O}_x} \tag{6.2}$$

$$Re[\tilde{M}(Q_y)] = M_{\mathrm{Cu}} + M_{\mathrm{O}_x} - M_{\mathrm{O}_y} \tag{6.3}$$

Therefore the Nematic order parameter as defined in Eqn. 6.1 reduces to,

$$O_N[M] = 2(M_{\mathrm{O}_y} - M_{\mathrm{O}_x}) \tag{6.4}$$

and the Nematic order parameter, which is defined based on the Bragg periodicities in the Fourier transform, can be interpreted as a global average of the difference between the O_y and the O_x sites. In this way, $O_N \neq 0$ implies that there is an inequivalence between the O bond directions in the x and y directions, breaking the rotational symmetry of the CuO_2 unit cell.

We probe three assumptions in Ref. [150]. First, we discuss whether electronic intra-unit cell nematicity can reliably be observed in dI/dV maps, which are the most straightforward experimental quantity. Secondly, we discuss the utility of Ref. [150]'s use of the Z-map normalization. Finally, we discuss whether experimental errors within the STM measurement techniques can give rise to an erroneous nematic signal.

6.2 Experimental demonstration of dI/dV matrix elements

We first address whether the $Z(\vec{r},V) = \frac{dI/dV(\vec{r},V)}{dI/dV(\vec{r},-V)}$ normalization scheme used by Lawler *et al.* is required to look for intra-unit cell broken symmetry, and whether strictly using the experimental dI/dV maps is sufficient. Recall from Chapter 2 that the differential tunneling conductance can be expressed as,

$$\frac{dI}{dV}(V) = I_0 e^{-2\kappa\Delta z}\rho(eV) \tag{6.5}$$

where I_0 is a constant with units of current, κ is the local barrier height, and Δz is the tip-sample separation. dI/dV is commonly associated directly to the local density of states, without consideration for the STM tunneling matrix elements: $\exp(-2\kappa\Delta z)$. For interpreting dI/dV for high resolution purposes, such as intra-unit cell broken symmetry, we have to be very careful in understanding the lengthscales of the matrix element, and whether it will couple into our desired signal.

We tested whether dI/dV could directly be associated with the DOS by acquiring two simultaneous dI/dV maps with different matrix elements. We varied the matrix elements by changing the experimental voltage and current feedback setpoints, (V_s, I_s) so that $V_{s1} = -V_{s2}$, but $|I_{s1}| = |I_{s2}|$. The two dI/dV maps were performed simultaneously by first setting the setpoint to $(V_s, I_s)_1$, acquiring a dI/dV spectrum, changing the setpoint to $(V_s, I_s)_2$, and then performing a second dI/dV spectroscopy. This process was repeated at each pixel, so that each pixel within dI/dV_1 is taken within ~ 2 seconds of dI/dV_2. If instead, we had acquired the two dI/dV maps in succession, rather than simultaneously, the piezoelectrics that comprise the STM scanner would be required to scan **twice** over the same area, increasing drift and other artifacts due to

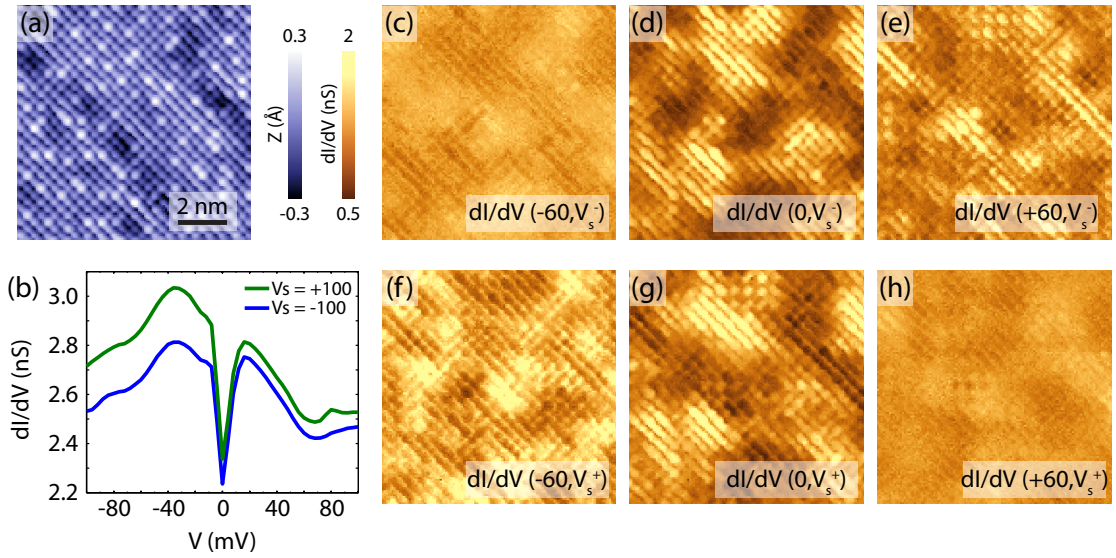

Figure 6.2: Robustness of dI/dV maps to V_s. **(a)** High resolution STM topography over a 9.5 × 9.5 nm^2 region of overdoped T_c = 16 K $Bi_{2-y}Pb_ySr_2CuO_{6+\delta}$. Topography was simultaneously acquired over the same field of view as shown in (c)-(h), with $V_s = -100$ mV. **(b)** Average spectra at different V_s. **(c-h)** dI/dV maps at the indicated bias (in mV) acquired with $V_s = -100$ mV for (c)-(e), and $V_s = +100$ mV for (f)-(h). All data was acquired at T = 4.75 K, I_s = 100 pA, $V_{\rm rms}$ = 2.1 mV. The STS maps were corrected for scan-piezo drift using the algorithm of Refs. [150, 151]. The drift fields used for each dataset were acquired from that dataset's own simultaneously acquired topographic image (i.e. $dI/dV(V_s^-)$ was corrected using the simultaneous topograph acquired at V_s^-).

piezoelectric errors.

The results of this experiment are shown in Fig. 6.2. Figure 6.2a shows a topographic image of the 9.5 × 9.5 nm^2 region that we studied. The topograph has excellent spatial resolution, and allows resolution of individual Bi atoms, as well as Pb atoms, which appear as larger bright atoms. Each atom is resolved by a $\sim$ 7 × 7 pixel grid, ensuring excellent atomic intra-unit cell resolution. Fig. 6.2b shows the field-of-view averaged spectra for the two dI/dV maps. The spectra shows characteristic gap features at $\Delta \sim 25$ mV, in agreement with previous measurements of Bi-2201 [141]. The vertical offset between the two spectra are the result of the fact that there is more integrated spectral weight from $V = 0 \rightarrow V = -100$ mV, than from $V = 0 \rightarrow V = +100$ mV. This causes the z position of the $V_s = -100$ mV dI/dV map to be further away from the surface to fix $I = I_s$, thereby reducing the conductance.

Figs. 6.2c-h are the key results of this experiment. We plot representative dI/dV images at the same biases of the two acquired datasets beside each other in Fig. 6.2c-h. What is most

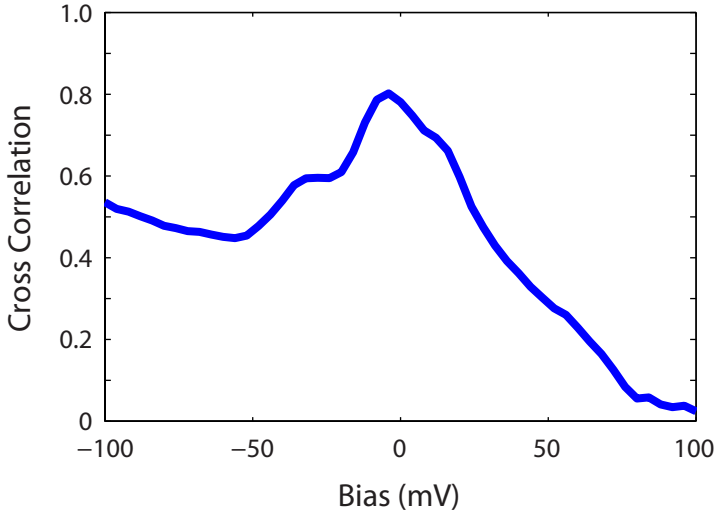

Figure 6.3: Cross correlation of dI/dV maps at different V_s. The correlation is computed from the quantity: $dI/dV(\vec{r}, V_{s1}) * dI/dV(\vec{r}, V_{s2})$, where the dI/dV maps are taken from those shown in Fig. 6.2. Cross correlation = 1 indicates a correlation between identical images.

striking between the two datasets acquired at different V_s is that each of the corresponding maps are not the same. While similar patterns are resolvable between corresponding maps at the same bias, there are still significant differences between the two. These findings are summarized in Fig. 6.3 which shows the cross correlation of the corresponding dI/dV maps as a function of bias. We can see that the correlation gets progressively worse, and is far from the ideal correlation of 1. Overall this implies that the matrix elements in dI/dV are significant, and that $dI/dV \neq \rho$, strictly speaking.

6.2.1 Differential Tunneling Conductance Matrix Elements

We now discuss the cause of the matrix element dependence on V_s shown in Figs. 6.2,6.3. Recall from Chapter 2 that the tunneling current and differential tunneling conductance are given by:

$$I(\vec{r}, V) = I_0 \exp(-2\kappa\Delta z) \int_{E_F}^{E_F+eV} \rho(\vec{r}, V')dV' \tag{6.6}$$

$$\frac{dI}{dV}(\vec{r}, V) = I_0 \exp(-2\kappa\Delta z)\rho(\vec{r}, eV) \tag{6.7}$$

where we have inserted $\vec{r}$ dependence into the above relations. At fixed $\vec{r}$, the matrix element is determined by the separation between the tip and the sample, Δz. Recall from Chapter 2 that Δz is determined by $I = I_s$ at a bias of V_s, so that (as shown in Eqn. 2.15):

$$\Delta z(\vec{r}) = \frac{-1}{2\kappa} \cdot \ln \left[\frac{I_s/I_0}{\int_{-V_s}^{0} \rho_s(\vec{r}, eV')dV'} \right] \tag{6.8}$$

which, when substituted into Eqn. 6.7 becomes:

$$\frac{dI}{dV}(\vec{r}, V) = \left(\frac{I_s}{\int_{E_F}^{E_F+eV_s} \rho(\vec{r}, eV')dV'} \right) \cdot \rho(\vec{r}, eV) \tag{6.9}$$

and so we define the matrix element for these purposes as:

$$|M|^2 = \left(\frac{I_s}{\int_{E_F}^{E_F+eV_s} \rho(\vec{r}, eV')dV'} \right) \tag{6.10}$$

This formulation of dI/dV relates dI/dV to the sum of the spectral weight from E_F to $E_V + eV_s$. To first order, if we ignore the spatial dependence in Eqn. 6.9, the two STS maps shown in Figs. 6.2,6.3 would differ by an overall multiplicative constant that is related to the sum of the spectral weight on the two sides: $\left(\int_{-100}^{0} \rho(\vec{r}, eV')dV'\right)^{-1}$ for $V_s = -100$ mV, and $\left(\int_{0}^{+100} \rho(\vec{r}, eV')dV'\right)^{-1}$ for $V_s = +100$ mV, and where V' is in units of mV. This fact would explain the overall change in the contrast for the two images.

However, an additional fact that we have ignored is the spatial dependence of $|M|^2$. From Eqn. 6.10, we can see that $|M|^2$ has $\vec{r}$ dependence (in the denominator of Eqn. 6.10) so that for $\vec{r}_1 \neq \vec{r}_2$, $|M(\vec{r}_1)|^2 \neq |M(\vec{r}_2)|^2$. Specifically, the square of the matrix elements differs by the sum of the spectral density at each location, as described in Eqn. 6.10. In instances where there is charge ordering or density of states modulations, $|M|^2$ at the peaks of the charge density wave will be different from $|M|^2$ at the zeros of the charge density wave, and have the relation: $\int \rho(\vec{r}_{\rm pk}, V)dV > \int \rho(\vec{r}_{\rm zero}, V)dV$. This implies that even within a single STS map, each point in the dI/dV map will differ from every other point by a multiplicative constant that depends on the integrated spectral weight. In most cases, we assume that by fixing the tip-sample separation

in a feedback loop at each location, we are explicitly fixing $\int_0^{V_{s1}} \rho(\vec{r}, eV')dV' \approx \int_0^{V_{s2}} \rho(\vec{r}, eV')dV'$, so that the matrix elements differ on a small scale compared to the variations in the density of states. This assumption allows us to typically interpret $\frac{dI}{dV}(\vec{r}, V)$ maps as representative of $\rho(\vec{r}, eV)$ maps. However, for the stringent experimental requirements of intra-unit cell nematicity, careful consideration must be paid to eliminate the source of this false spatial dependence.

6.3 Z MAP NORMALIZATION

We now discuss whether dI/dV normalization techniques can be used to correct the spatial and experimental dependence of the dI/dV maps shown in Fig. 6.2.

In Lawler *et al.* [150], the broken intra-unit cell rotational symmetry was found in Z normalized maps that were introduced by Lee *et al.* [174] to remove the effect of the tunneling matrix elements $|M|^2$. The Z-map is defined by performing the following operation to dI/dV maps:

$$Z(\vec{r}, V) = \frac{dI/dV(\vec{r}, V)}{dI/dV(\vec{r}, -V)} \quad \text{for } V > 0. \tag{6.11}$$

Because the expression for the square of the matrix elements in Eqn. 6.10 depends only on $(\vec{r}, V_s, I_s)$, dI/dV data taken at different energies, but at the same spatial location, will have the same matrix element. Therefore any normalization scheme that divides $dI/dV(\vec{r}, V_1)$ by $dI/dV(\vec{r}, V_2)$, will eliminate the effect of the matrix element, but the key is choosing a normalization scheme that has physical significance. In the case of the Z map defined in Eqn. 6.11, straightforward evaluation leads to:

$$Z(\vec{r}, V) = \frac{\rho(\vec{r}, V)}{\rho(\vec{r}, -V)} \quad \text{for } V > 0. \tag{6.12}$$

The Z map can then be interpreted as measuring the particle-hole asymmetry of the system, which theoretically should be free of matrix element effects.

We verified the robustness of the Z map normalization to different matrix elements of the underlying dI/dV maps, by performing the Z normalization to the dI/dV maps acquired in Fig. 6.2. A subset of the Z normalized images acquired at $V_s = -100$ mV and at $V_s = +100$ mV

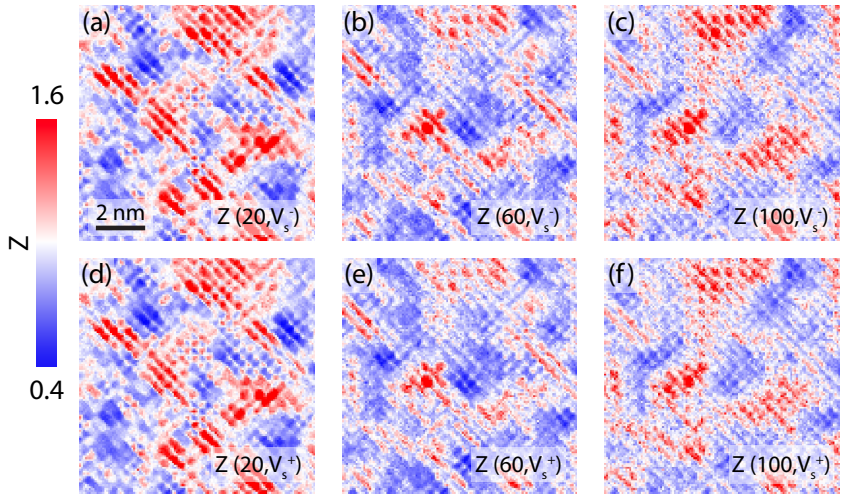

Figure 6.4: Robustness of Z-map normalization to V_s. Z-map normalization of dI/dV map from Fig. 6.2 acquired at $V_s = -100$ mV **(a-c)** , $V_s = +100$ mV **(d-f)**. Note all panels are plotted on the same color scale, and that white in this color scale corresponds to $Z = 1$, and can be interpreted as being a location that is particle-hole symmetric.

are shown in Figs. 6.4a-c and 6.4d-f, respectively. The two Z normalized maps are in excellent agreement with each other, even though the respective dI/dV maps were acquired with different V_s. The spatial patterns in both maps, and the Z intensities are all in agreement spatially, in contrast to the differences in the original dI/dV maps shown in Fig. 6.2. We summarize the findings of Fig. 6.4 by plotting the cross correlation of the two independently acquired Z maps as a function of energy in Fig. 6.5. The cross correlation coefficient is consistently > 0.85 across the entire energy range, indicating the validity of the Z map in eliminating the matrix element effects inherent in dI/dV maps.

6.4 Erroneous nematic signal due to piezoelectric drift

While the Z-map normalization eliminates spatial and experimental setpoint dependence in dI/dV maps, because the normalization procedure involves a quotient of datapoints taken at different times, it is unclear whether other experimental errors could give rise to an erroneous nematic signal in Z. In this section we describe a toy model that demonstrates that the nematic signature described by Lawler *et al.* [150] could arise from experimental errors in the STM data

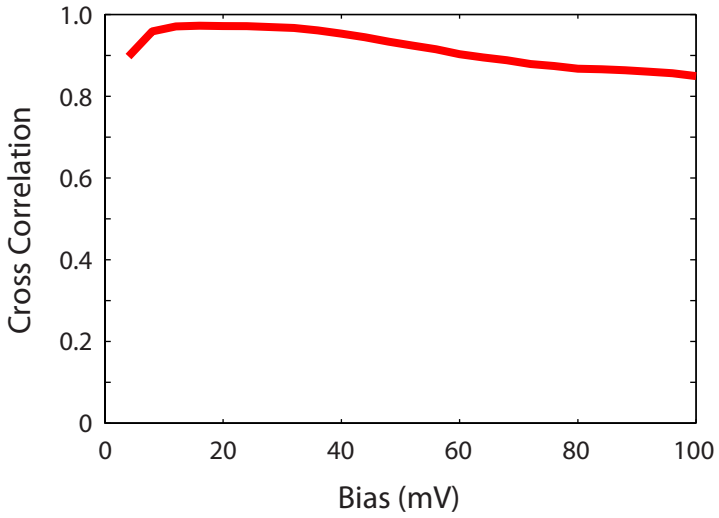

Figure 6.5: Cross-correlation of Z maps at different V_s. The correlation is computed from the quantity: $Z(\vec{r}, V; V_{s1}) * Z(\vec{r}, V; V_{s2})$ where Z is defined from its respective $dI/dV(\vec{r}, V; V_{s1,s2})$ using Eqn. 6.11. The Z maps are taken from those shown in Fig. 6.4. Cross correlation = 1 indicates an ideal correlation.

acquisition and analysis procedure.

The broken rotational symmetry in $Bi_2Sr_2CaCu_2O_{8+\delta}$ was found by observing that the x-y symmetry was broken on the unit-cell lengthscale by looking at the Fourier transform of the $Z(x, y)$ maps [150]. As shown previously in Eqn. 6.4, evaluating the real-part of the Fourier transform peak at the Bragg periodicity, $Re[\tilde{Z}(Q_y)]$, is essential to the interpretation that O_N measures intra-unit cell nematicity. This requires precise phase information, to ensure that the STS data is perfectly in-phase with the Cu atoms in CuO_2 lattice. However, STM does not measure the CuO_2 plane directly. Instead, STM measurements scan the BiO plane, and assume that because the Bi and Cu atoms are directly on top of each other in the crystal lattice (see Fig. 1.6 in Chap. 1), the imaged Bi atoms of the BiO lattice serves as a direct registry of the Cu atoms in the CuO_2 plane.

The perfect registry of the imaged Bi lattice to the underlying CuO_2 lattice is true in ideal situations. However, experimental artifacts from the STM piezoelectric scanning head can cause erroneous smearing or "drift" effects that might cause a misalignment in the apparent positions of the BiO and CuO_2 lattices. Because the piezoelectric scanners are essentially capacitors, sud-

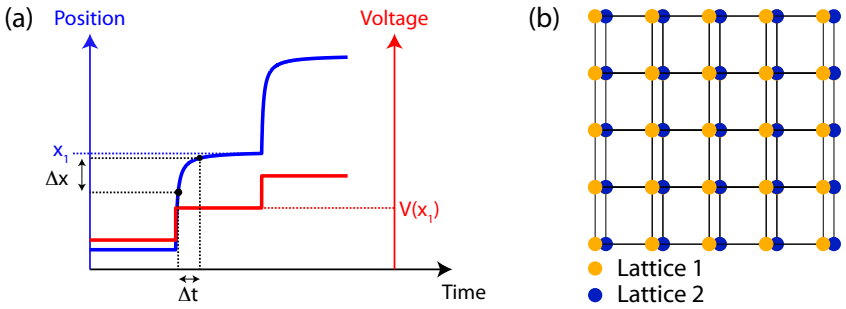

Figure 6.6: Error in Lattice Registry due to Piezoelectric Drift. (a) Mis-registry due to piezo relaxation. The location of the tip is in principle controlled by the voltage (red), so that for $V = V(x_1)$, the position of the tip should be $x = x_1$ asymptotically. However, depending on the time of the measurement, the actual position of the tip will differ from x_1. At two indicated times (black dots), separated by Δt, the position drifts by up to Δx. **(b)** Piezoelectric drift shown in (a) could lead to a shift in the perceived location of the lattice in one measurement versus the next measurement.

den voltage changes applied to change the spatial location of the STM tip will result in the actual voltage across the piezo being slightly different from the asymptotic value. If however, the voltage to the piezo is held constant for a sufficiently long "relaxation time", the position of the piezo will reach its asymptotic value. This situation is schematically illustrated in Fig. 6.6a. As the STM tip is relaxing into the asymptotic position, the computer does not take into account this misregistry, and because the voltage applied to the piezo is the steady state value V_{x1}, the computer assumes that the tip is at position at x_1. The results in artificial streaks in the image that are familiar to all STM experimentalists. The standard technique to combat this effect is to apply a constant voltage on the piezos for a long time period before acquiring data.

This effect is particularly important in evaluating the Fourier transforms of the Z-map. Because the Z map is a quotient of two datapoints measured separately in time by up to $1-2$ seconds, in principal there could be significant piezo drift between the two measurements $dI/dV(-V)$ and $dI/dV(+V)$. The result of drift between of the STM tip relative to the CuO_2 lattice measured at $dI/dV(-V)$ and $dI/dV(+V)$ would correspond to some directional phase shift of the Cu lattice of the two measurements, as shown in Fig. 6.6b. dI/dV modulations that would otherwise be in-phase with the Cu lattice and have the form $dI/dV = A\cos(Q_x x)$ would gain an additional

phase and become,

$$\frac{dI}{dV} = A\cos(Q_x x + \phi_x) = A\cos\phi_x \cos(Q_x x) - A\sin\phi_x \sin(Q_x x) \tag{6.13}$$

which reduces the magnitude of the real component of the Fourier transform from $A \to A\cos\phi_x$.

6.4.1 Toy Model of Lattice Drift

This problem is particularly important for the Z map given the misregistry between the $+V$ and $-V$ measurements. If we approximate the dI/dV modulations in a given direction by,

$$\frac{dI}{dV}(x) \approx 1 + A_x \cos(Q_x x) \tag{6.14}$$

where $A_x \sim 0.1 - 0.01$ and represents the fraction of the total amplitude of dI/dV that is in the Bragg channel, then the Z map is represented by,

$$Z_x = \frac{dI/dV(+V)}{dI/dV(-V)} = \frac{1 + A_x \cos(Q_x x)}{1 + B_x \cos(Q_x x + f_x)} \tag{6.15}$$

where A_x and B_x represent the fractional amplitudes of the $+V$ and $-V$ measurements, and f_x is the relative phase shift between the $+V$ and $-V$ measurements. The phase mismatch within a single spectrum was estimated by Hamidian *et al.* [173] to be $< 2\%$ of a lattice constant, and so we fix $f_x = 2\pi \times 0.02$ to be the maximum drift in a STM spectrum. The form of Z_x from Eqn. 6.15 depends on the values of A_x, B_x. For $A = 0.1$, we plot the form of Z_x as a function of (B,x) in Fig. 6.7. We can clearly see that the region around $B \approx A$ represents a region in phase space where Z_x is heavily shifted away from the Q_x periodicity. For $B < 0.8A$, Z_x is still in phase with the lattice and the dI/dV measurements, while for $B > 1.2A$, Z_x is out of phase with the dI/dV measurements. This shows that the effect of scan piezo drift on any Z_x measurement is to induce a non-trivial phase. Overall, this demonstrates that scan-piezo drift couples into the Z maps, which have been used to find evidence for broken intra-unit cell rotational symmetry.

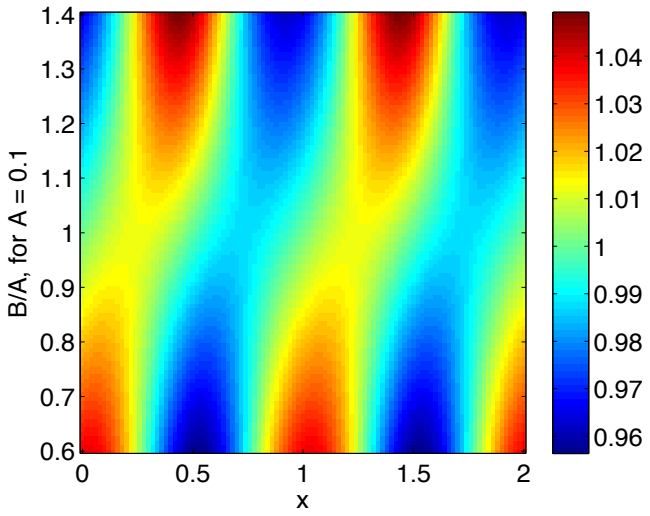

Figure 6.7: Toy Model simulation of Z_x. Simulation uses the approximation in Eqn. 6.15 to model Z_x for $f = 0.02 * Q_x$ and $A = 0.1$. For $B < 0.8A$ Z_x shifts phase by π compared to Z_x for $B > 1.2A$. The intermediate region where $B \approx A$ causes non-trivial phase shifts as well.

6.5 Order Parameters under Rotation

6.5.1 Robustness of $O_N(Z)$ to Rotation

We performed an experimental test to determine whether scan-piezo noise could infiltrate the Nematic signal. In a STS map, the tip scans the pixels along each row, designated the fast-scan axis, before moving up to the next row. Therefore, because the piezo is being moved most quickly in this direction, we would expect the fast-scan axis to have the dominant noise due to piezoelectric drift. To investigate whether this would infiltrate the Nematic signal, we acquired two identical STS maps with their fast-scan axes oriented 90° to each other. The maps are designated as the $+45°$, and $-45°$ maps. To check whether the two maps agree with each other, we evaluated the local Nematic order parameter in space, over a 5 atom lengthscale, to give $O_N(Z(\vec{r}, V; \pm 45°))$. This experimental test is shown in Fig. 6.8. By eye, all of the panels associated with the $+45°$ map are well correlated with the panels associated with the $-45°$ map. The nematic domain boundaries, regions with asymmetry along one axis vs. the other axis, are well correlated, and have the same shape and magnitude. Together, these maps show that for the experimental pa-

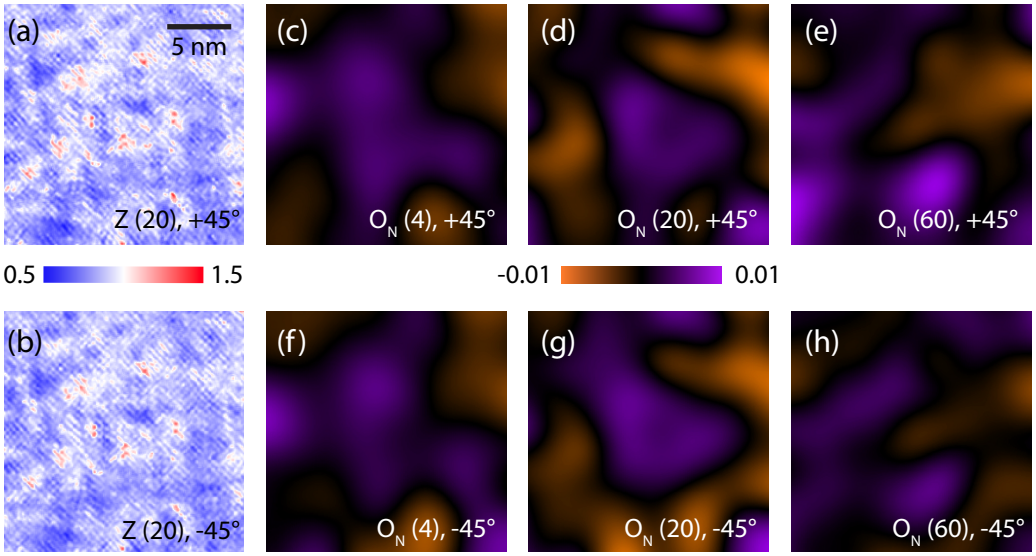

Figure 6.8: Nematic order parameter under rotation. Robustness of the Nematic order parameter to the angle of scan rotation. Two dI/dV spectral maps were obtained with their fast scan axes perpendicular to each other (designated $+45°$ and $-45°$). **(a,b)** Z maps at $V = 20$ mV for the two spectral maps obtained. The $-45°$ map has been rotated $90°$ to allow for easier comparison with (a). **(c-h)** Local nematic order parameter $O_N(Z(\vec{r}, V))$ at the indicated bias (in mV), for the $+45°$ and $-45°$ maps, as indicated. Data were acquired over an 18.5×18.5 nm^2 region of OD $T_c = 16$ K, $Bi_{2-y}Pb_ySr_2CuO_{6+\delta}$, at $T = 4.8$ K, $V_s = -100$ mV, $I_s = 100$ pA. All conductance maps have been drift corrected and aligned according to their own respective simultaneously acquired topographic images. Each STS map was processed independently from the other.

rameters used to acquire the data in Fig. 6.8, the electronic parameters, specifically the Z map and $O_N(Z(\vec{r}, V))$, are independent of scan-axis, and therefore independent of scan-piezo error.

6.5.2 Robustness of Amplitude Order Parameter

We now discuss whether other order parameters could be used to measure electronic nematicity. In contrast to the nematic definition relying on the real component of the Bragg wavevectors in Eqn. 6.1, which we now denote,

$$O_N^{\mathrm{Re}} = Re[\tilde{M}(Q_y)] - Re[\tilde{M}(Q_x)] \tag{6.16}$$

we could instead measure the total difference in the amplitude along the x and y directions:

$$O_N^{\mathrm{Amp}} = |\tilde{M}(Q_y)| - |\tilde{M}(Q_x)|. \tag{6.17}$$

Because $|\tilde{M}(Q)|^2 = Re[\tilde{M}(Q)]^2 + Im[\tilde{M}(Q)]^2$, we need to understand the physical interpretation of $Im[\tilde{M}(Q_x)]$ to gain intuition for O_N^{Amp}. If we look at the cartoon illustration of the CuO_2 lattice in Fig. 6.1, we can see that $Im[\tilde{M}(Q_x)]$ can be understood as a $\sin(Q_x x)$ modulation, centered at the Cu site, analogous to how $Re[\tilde{M}(Q_x)]$ is understood as a $\cos(Q_x x)$ modulation. Thus, $Im[\tilde{M}(Q_x)]$ can be understood as measuring the asymmetry of the adjacent Cu-O bond sites. However, as discussed in Hamidian *et al.* [173], an imaginary order parameter:

$$O_N^{\mathrm{Im}} = Im[\tilde{M}(Q_y)] - Im[\tilde{M}(Q_x)] \tag{6.18}$$

would be extremely sensitive to scan-piezo noise because a phase-shift δ in the lattice, caused by lattice mis-registry, would couple into O_N^{Im} because for x close to $x = 0$,

$$\sin(Q_x x + \delta) \approx \sin(\delta) + Q_x \cos(\delta) x \approx Q_x x + \delta + O(\delta^2) \tag{6.19}$$

where the last line used the relationship that $\delta << 1$. On the other hand, for O_N^{Re} which is represented by $\cos(Q_x x)$, the impact of a phase shift δ would be (for small x close to $x = 0$):

$$\cos(Q_x x + \delta) \approx \cos(\delta) - Q_x \sin(\delta) x \sim O(\delta^2) \tag{6.20}$$

where the last line assumes that for small x, $Q_x x \sim O(\delta)$. The two results in Eqns. 6.19,6.20 show that the atom centered order O_N^{Re} is sensitive to phase shifts only to second order, while the bond-centered order O_N^{Im} is sensitive to phase shifts to first order. This invalidates the use of O_N^{Im}.

However, the question remains, how sensitive is the amplitude order parameter O_N^{Amp} to phase shifts? To answer this question we show in Fig. 6.9 the effect of different scan angles on the

$O_N^{\mathrm{Re}}(Z(\vec{r},V;\pm45°))$ and $O_N^{\mathrm{Amp}}(Z(\vec{r},V;\pm45°))$ maps. The set of images in Fig. 6.9 show that $O_N^{\mathrm{Re}}(Z(\vec{r},V;\pm45°))$ is significantly better correlated between different scan angles compared to $O_N^{\mathrm{Amp}}(Z(\vec{r},V;\pm45°))$. To better quantify this trend, we plot the energy dependence of,

$$O_N^{\mathrm{Re,Amp}}(Z(\vec{r},V;+45°)) * O_N^{\mathrm{Re,Amp}}(Z(\vec{r},V;-45°)),$$

where $*$ indicates a cross correlation, in Fig. 6.10. Because the cross correlations of O_N^{Re} in Fig. 6.10 is consistently larger than 0.7 across all energies shown, we can conclude that O_N^{Re} is robust to scan-angle rotation and therefore scan-piezo induced phase shifts. However, the poor correlation of O_N^{Amp} across scan angles, even becoming anti-correlated for $E > 40$ mV, shows that O_N^{Amp} is not robust to scan-piezo induced phase shifts. This demonstrates that the phase information that is lost in the definition of O_N^{Amp} is crucial to measure any form of broken symmetry and the results of Figs. 6.9,6.10 invalidate the use of O_N^{Amp} to measure broken symmetries.

6.6 Conclusion

Our results point to the validity of the analysis technique used by Lawler *et al.*, while filling in some of the required experimental details. We have demonstrated that matrix element effects in dI/dV maps render them unsuitable for high resolution studies, such as the search for electronic intra-unit cell nematicity. Secondly, we show that the Z map normalization, while not being unique in eliminating matrix element effects, does eliminate the spatial and setpoint dependence of the matrix elements. We used a simple toy model to illustrate how scan piezo errors could infiltrate the Nematic signal of a $Z(x,y)$ map and give rise to an erroneous nematic signal. However, our demonstration of the robustness of nematic ordering to scan direction indicates that for a well chosen set of experimental parameters, it is possible to eliminate scan piezo noise from the measurement of $O_N(Z)$. Furthermore, our analysis of an amplitude order parameter and demonstration of its sensitivity to scan-piezo error, further validates the use of $O_N(Z)$ as defined in Ref. [150]. This validates the results of Lawler *et al.* [150], and points to the importance of understanding the relationship between broken symmetries and the pseudogap phase.

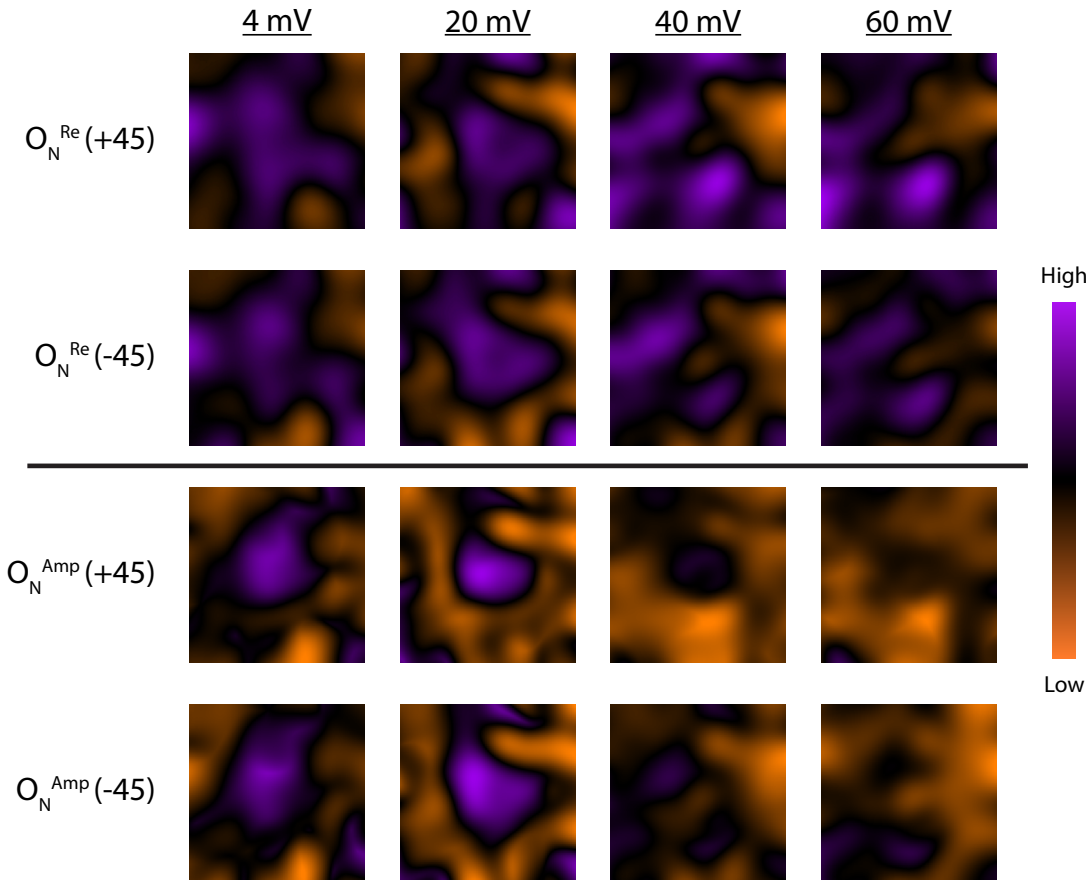

Figure 6.9: Broken symmetry order parameters under rotation. The $Z(+45°)$ and $Z(-45°)$ maps shown in Fig. 6.8 are used to calculate broken symmetry order parameters as defined in Eqn. 6.1 for O_N^{Re} and Eqn. 6.17 for O_N^{Amp}. The column labels at the top show the energy of the respective O_N maps, while the rows indicate the O_N order and the scan rotation angle. Each pair of rotated images that fixes O_N and E (i.e. $O_N^{\mathrm{Re}}(+4\ \mathrm{mV}, +45°)$ and $O_N^{\mathrm{Re}}(+4\ \mathrm{mV}, -45°)$) are plotted using the same numerical color bar. However, to increase the contrast available between energies, we allow the max/min of the color bars between energies to vary. The images cover a $18.5 \times 18.5\ \mathrm{nm}^2$ region of Bi-2201.

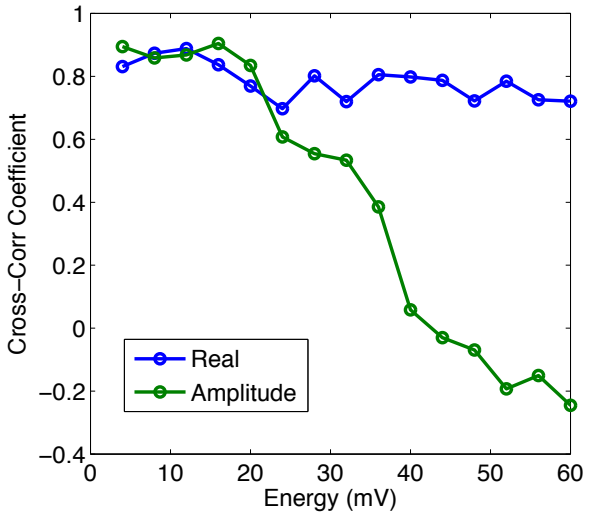

Figure 6.10: Cross correlation of Order Parameters acquired at different Scan Angles. The cross correlation coefficient of $O_N^{\mathrm{Re,Amp}}(Z(\vec{r},V;+45^\circ)) * O_N^{\mathrm{Re,Amp}}(Z(\vec{r},V;-45^\circ))$ is plotted as a function of energy for the Real (O_N^{Re}) and Amplitude (O_N^{Amp}) order parameters as indicated in the legend. The order parameters are taken from the data shown in Fig. 6.9. A cross correlation coefficient of 1 is an ideal correlation.

References

[1] Liang Fu, Charles L Kane, and Eugene J Mele. Topological insulators in three dimensions. *Phys. Rev. Lett.*, 98(10):106803, 2007.

[2] M Zahid Hasan and C L Kane. *Colloquium*: Topological insulators. *Reviews of Modern Physics*, 82(4):3045–3067, November 2010.

[3] Xiao-Liang Qi and Shou-Cheng Zhang. Topological insulators and superconductors. *Reviews of Modern Physics*, 83(4):1057–1110, October 2011.

[4] Yoichi Ando. Topological Insulator Materials. *Journal of the Physical Society of Japan*, 82:102001, 2013.

[5] Joel E Moore. The birth of topological insulators. *Nature*, 464(7286):194–198, March 2010.

[6] B I Halperin. Quantized Hall conductance, current-carrying edge states, and the existence of extended states in a two-dimensional disordered potential. *Phys. Rev. B*, 25(4):2185–2190, February 1982.

[7] C L Kane and E J Mele. Z2 Topological Order and the Quantum Spin Hall Effect. *Phys. Rev. Lett.*, 95(14):146802 EP –, September 2005.

[8] B A Bernevig, T L Hughes, and S C Zhang. Quantum Spin Hall Effect and Topological Phase Transition in HgTe Quantum Wells. *Science*, 314(5806):1757–1761, December 2006.

[9] J E Moore and L Balents. Topological invariants of time-reversal-invariant band structures. *Phys. Rev. B*, 75(12):121306 EP –, March 2007.

[10] Rahul Roy. Topological phases and the quantum spin Hall effect in three dimensions. *Phys. Rev. B*, 79(19):195322 EP –, May 2009.

[11] Y Xia, D Qian, D Hsieh, L Wray, A Pal, H Lin, A Bansil, D Grauer, Y S Hor, R J Cava, and M Zahid Hasan. Observation of a large-gap topological-insulator class with a single Dirac cone on the surface. *Nat Phys*, 5(6):398–402, May 2009.

[12] Jungpil Seo, Pedram Roushan, Haim Beidenkopf, Y S Hor, R J Cava, and Ali Yazdani. Transmission of topological surface states through surface barriers. *Nature*, 466(7304):343–346, July 2010.

[13] Ion Garate and M Franz. Inverse Spin-Galvanic Effect in the Interface between a Topological Insulator and a Ferromagnet. *Phys. Rev. Lett.*, 104(14):146802 EP –, April 2010.

[14] Liang Fu and C L Kane. Superconducting Proximity Effect and Majorana Fermions at the Surface of a Topological Insulator. *Phys. Rev. Lett.*, 100(9):096407 EP –, March 2008.

[15] Frank Wilczek. Majorana returns. *Nat Phys*, 5(9):614–618, September 2009.

[16] Jeffrey C Y Teo and C L Kane. Majorana Fermions and Non-Abelian Statistics in Three Dimensions. *Phys. Rev. Lett.*, 104(4):046401 EP –, January 2010.

[17] J Bardeen, L Cooper, and JR Schrieffer. Microscopic theory of superconductivity. *Physical Review*, January 1957.

[18] H K Onnes. . *Commun Phys Lab Leiden*, 1911.

[19] Jennifer E Hoffman. *A Search for Alternative Electronic Order in the High Tc Superconductor Bi-2212 by STM*. PhD thesis, University of California, Berkeley, December 2003.

[20] JG BEDNORZ and KA MULLER. POSSIBLE HIGH-TC SUPERCONDUCTIVITY IN THE BA-LA-CU-O SYSTEM. *Z Phys B Con Mat*, 64(2):189–193, January 1986.

[21] M K Wu, J R Ashburn, C J Torng, P H Hor, R L Meng, L Gao, Z J Huang, Y Q Wang, and C W Chu. Superconductivity at 93 K in a new mixed-phase Y-Ba-Cu-O compound system at ambient pressure. *Phys. Rev. Lett.*, 58(9):908–910, March 1987.

[22] Ilija Zeljkovic. *Visualizing the Interplay of Structural and Electronic Disorders in High-Temperature Superconductors using Scanning Tunneling Microscopy*. PhD thesis, Harvard University, May 2013.

[23] Patrick A Lee, Naoto Nagaosa, and Xiao-Gang Wen. Doping a Mott insulator: Physics of high-temperature superconductivity. *Reviews of Modern Physics*, 78(1):17–85, January 2006.

[24] Y He, Y Yin, M Zech, A Soumyanarayanan, M M Yee, T Williams, M C Boyer, K Chatterjee, W D Wise, I Zeljkovic, T. Kondo, T Takeuchi, H Ikuta, P Mistark, R S Markiewicz, A Bansil, S Sachdev, Eric W Hudson, and Jennifer E Hoffman. Fermi Surface and Pseudogap Evolution in a Cuprate Superconductor. *Science*, 344(6184):608–611, May 2014.

[25] A R Schmidt, K Fujita, Eun-Ah Kim, M J Lawler, H Eisaki, S Uchida, D-H Lee, and J. C. Seamus Davis. Electronic structure of the cuprate superconducting and pseudogap phases from spectroscopic imaging STM. *New J. Phys.*, 13(6):065014, June 2011.

[26] Michael M Yee, Yang He, Anjan Soumyanarayanan, Dae-Jeong Kim, Zachary Fisk, and Jennifer E Hoffman. Imaging the Kondo Insulating Gap on SmB6. *arXiv*, page 1308.1085, August 2013.

[27] Michael M Yee, Z H Zhu, Anjan Soumyanarayanan, Yang He, Can-Li Song, Zaher Salman, Amit Kanigel, Yoichi Ando, and Jennifer E Hoffman. Impurity induced phase separation and scattering in Bi2-xFexSe3. April 2014.

[28] R Comin, A Frano, M M Yee, Y Yoshida, H Eisaki, E Schierle, E Weschke, R Sutarto, F He, A Soumyanarayanan, Yang He, M Le Tacon, Jennifer E Hoffman, B Keimer, and Andrea Damascelli. Charge Order Driven by Fermi-Arc Instability in Bi2Sr2−xLaxCuO6+δ. *Science*, 343(6169):390–392, January 2014.

[29] J Bardeen. Tunnelling from a Many-Particle Point of View. *Phys. Rev. Lett.*, 6(2):57–59, January 1961.

[30] G Binnig, H Rohrer, Ch Gerber, and E Weibel. Surface Studies by Scanning Tunneling Microscopy. *Phys. Rev. Lett.*, 49(1):57–61, July 1982.

[31] Yi Yin. *The Investigation of Scanning Tunneling Microscopy and Spectroscopy on High-Tc Superconductors: Cuprates and Pnictides*. PhD thesis, Harvard University, October 2009.

[32] A Raccanelli, L A Reichertz, and E Kreysa. Eliminating the vibrational noise in continuously filled 1 K pots. *Cryogenics*, 41(10):763–766, October 2001.

[33] P Gorla, C Bucci, and S Pirro. Complete elimination of 1K Pot vibrations in dilution refrigerators. *Nuclear Instruments and Methods in Physics Research Section A: Accelerators, Spectrometers, Detectors and Associated Equipment*, 520(1-3):641–643, 2004.

[34] K Nagaoka, T Jamneala, M Grobis, and M F Crommie. Temperature dependence of a single Kondo impurity. *Phys. Rev. Lett.*, 88(7):077205, 2002.

[35] Tong Zhang, Peng Cheng, Xi Chen, Jin-Feng Jia, Xucun Ma, Ke He, Lili Wang, Hai-Jun Zhang, Xi Dai, Zhong Fang, and Qi-Kun Xue. Experimental Demonstration of Topological Surface States Protected by Time-Reversal Symmetry. *Phys. Rev. Lett.*, 103(26):266803, December 2009.

[36] Piers Coleman. Heavy fermions: Electrons at the edge of magnetism. *Handbook of Magnetism and Advanced Magnetic Materials*, 2007.

[37] J Kondo. Resistance Minimum in Dilute Magnetic Alloys. *Progress of Theoretical Physics*, 32(1):37–49, July 1964.

[38] D Goldhaber-Gordon, Hadas Shtrikman, D Mahalu, David Abusch-Magder, U Meirav, and M A Kastner. Kondo effect in a single-electron transistor. *Nature*, 391(6663):156–159, January 1998.

[39] Maxim Dzero, Kai Sun, Victor Galitski, and Piers Coleman. Topological Kondo insulators. *Phys. Rev. Lett.*, 104(10):106408, 2010.

[40] Tetsuya Takimoto. SmB6: A Promising Candidate for a Topological Insulator. *Journal of the Physical Society of Japan*, 80(12), 2011.

[41] Mengxing Ye, J W Allen, and Kai Sun. Topological crystalline Kondo insulators and universal topological surface states of SmB $_6$. *arXiv preprint*, 2013.

[42] Feng Lu, JianZhou Zhao, Hongming Weng, Zhong Fang, and Xi Dai. Correlated Topological Insulators with Mixed Valence. *Phys. Rev. Lett.*, 110(9):096401 EP –, February 2013.

[43] A. Menth, E. Buehler, and T. Geballe. Magnetic and Semiconducting Properties of SmB_6. *Phys. Rev. Lett.*, 22(7):295–297, February 1969.

[44] J. Allen, B. Batlogg, and P. Wachter. Large low-temperature Hall effect and resistivity in mixed-valent SmB_6. *Phys. Rev. B*, 20(12):4807–4813, December 1979.

[45] J. Cooley, M. Aronson, Z. Fisk, and P. Canfield. SmB6: Kondo Insulator or Exotic Metal? *Phys. Rev. Lett.*, 74(9):1629–1632, February 1995.

[46] D J Kim, S Thomas, T Grant, J Botimer, Z. Fisk, and Jing Xia. Surface Hall Effect and Nonlocal Transport in SmB6: Evidence for Surface Conduction. *Sci. Rep.*, 3:3150, 2013.

[47] Steven Wolgast, Çağlıyan Kurdak, Kai Sun, J W Allen, Dae-Jeong Kim, and Zachary Fisk. Low-temperature surface conduction in the Kondo insulator SmB 6. *Phys. Rev. B*, 88(18):180405, 2013.

[48] D J Kim, J Xia, and Z. Fisk. Topological surface state in the Kondo insulator samarium hexaboride. *Nature Materials*, 13(5):466–470, March 2014.

[49] S. Thomas, D. Kim, S. Chung, T. Grant, and Z. Fisk. Weak Antilocalization and Linear Magnetoresistance in The Surface State of SmB6. *arXiv*, page 1307.4133, July 2013.

[50] Xiaohang Zhang, N P Butch, P Syers, S Ziemak, Richard L Greene, and Johnpierre Paglione. Hybridization, inter-ion correlation, and surface states in the Kondo insulator SmB 6. *Phys. Rev. X*, 3(1):011011, 2013.

[51] G Li, Z Xiang, F Yu, T Asaba, B Lawson, P Cai, C Tinsman, A Berkley, S Wolgast, Y S Eo, Dae-Jeong Kim, C Kurdak, J W Allen, K Sun, X H Chen, Y Y Wang, Z. Fisk, and Lu Li. Quantum oscillations in Kondo Insulator SmB6. *arXiv*, June 2013.

[52] Hidetoshi Miyazaki, Tetsuya Hajiri, Takahiro Ito, Satoru Kunii, and Shin-ichi Kimura. Momentum-dependent hybridization gap and dispersive in-gap state of the Kondo semiconductor SmB 6. *Phys. Rev. B*, 86(7):075105, 2012.

[53] N Xu, X Shi, P K Biswas, C E Matt, R S Dhaka, Y Huang, N C Plumb, M Radovic, E Pomjakushina, K Conder, A Amato, Z. Salman, D McK Paul, J Mesot, H Ding, and M Shi. Surface and bulk electronic structure of the strongly correlated system SmB_6 and implications for a topological Kondo insulator. *Phys. Rev. B*, 88(12):121102 EP –, September 2013.

[54] J Jiang, S Li, T Zhang, Z Sun, F Chen, Z R Ye, M Xu, Q Q Ge, S Y Tan, X H Niu, M Xia, B P Xie, Y F Li, X H Chen, H-H Wen, and D L Feng. Observation of possible topological in-gap surface states in the Kondo insulator SmB6 by photoemission. *Nat Commun*, 4 SP -:1306.5664, June 2013.

[55] Z-H Zhu, A Nicolaou, G Levy, N P Butch, P Syers, X F Wang, J Paglione, G A Sawatzky, I S Elfimov, and Andrea Damascelli. Polarity-Driven Surface Metallicity in SmB6. *Phys. Rev. Lett.*, 111(21):216402, 2013.

[56] M Neupane, N Alidoust, S Y Xu, T. Kondo, Y Ishida, Chang Liu, I Belopolski, Y J Jo, T R Chang, H T Jeng, T. Durakiewicz, L Balicas, H Lin, A Bansil, S Shin, and M Zahid Hasan. Surface electronic structure of the topological Kondo-insulator candidate correlated electron system SmB6. *Nature Communications*, 4 SP -:2991, December 2013.

[57] E Frantzeskakis, N de Jong, B Zwartsenberg, Y K Huang, Y Pan, X Zhang, J X Zhang, F X Zhang, L H Bao, O Tegus, A Varykhalov, A de Visser, and M S Golden. Kondo Hybridization and the Origin of Metallic States at the (001) Surface of SmB6. *Phys. Rev. X*, 3(4):041024 EP –, December 2013.

[58] K Flachbart, K Gloos, E Konovalova, Y Paderno, M Reiffers, P Samuely, and P Švec. Energy gap of intermediate-valent SmB 6 studied by point-contact spectroscopy. *Phys. Rev. B*, 64(8):085104, 2001.

[59] G Travaglini and P Wachter. Intermediate-valent Sm B 6 and the hybridization model: An optical study. *Phys. Rev. B*, 29(2):893, 1984.

[60] B Gorshunov, N Sluchanko, A Volkov, G Knebel, and S Kunii. Low-energy electrodynamics of SmB6. *Phys. Rev. B*, 59(3):1808–1814, January 1999.

[61] P Nyhus, S L Cooper, Z. Fisk, and J Sarrao. Light scattering from gap excitations and bound states in SmB 6. *Phys. Rev. B*, 52(20):R14308, 1995.

[62] G Güntherodt, W A Thompson, F Holtzberg, and Z. Fisk. Electron Tunneling into Intermediate-Valence Materials. *Phys. Rev. Lett.*, 49(14):1030–1033, October 1982.

[63] B. Amsler, Z. Fisk, J. Sarrao, S. Molnar, M. Meisel, and F. Sharifi. Electron-tunneling studies of the hexaboride materials SmB6, EuB6, CeB6, and SrB6. *Phys. Rev. B*, 57(15):8747–8750, April 1998.

[64] J D Denlinger, J W Allen, J S Kang, K Sun, J W Kim, J H Shim, B I Min, Dae-Jeong Kim, and Z. Fisk. Temperature Dependence of Linked Gap and Surface State Evolution in the Mixed Valent Topological Insulator SmB6. *arXiv*, December 2013.

[65] Victor Alexandrov, Maxim Dzero, and Piers Coleman. Cubic Topological Kondo Insulators. *arXiv*, page 1303.7224, March 2013.

[66] Shigemasa Suga, Kazuyuki Sakamoto, Taichi Okuda, Koji Miyamoto, Kenta Kuroda, Akira Sekiyama, Junichi Yamaguchi, Hidenori Fujiwara, Akinori Irizawa, Takahiro Ito, Shinichi Kimura, T Balashov, W Wulfhekel, S Yeo, Fumitoshi Iga, and Shin Imada. Spin-Polarized Angle-Resolved Photoelectron Spectroscopy of the So-Predicted Kondo Topological Insulator SmB6. *Journal of the Physical Society of Japan*, 83(1):014705, December 2013.

[67] M Aono, R Nishitani, C Oshima, T Tanaka, E Bannai, and S Kawai. LaB 6 and SmB 6(001) surfaces studied by angle-resolved XPS, LEED and ISS. *Surface Science*, 86:631–637, 1979.

[68] John Ozcomert and Michael Trenary. Atomically resolved surface structure of LaB6(100). *Surface Science*, 265(1-3):L227–L232, April 1992.

[69] Miao Gao, Fengjie Ma, Zhong-Yi Lu, and Tao Xiang. Surface structures of ternary iron arsenides AFe_2As_2 (A=Ba, Sr, or Ca). *Phys. Rev. B*, 81(19):193409, May 2010.

[70] Jeremy Figgins and Dirk K Morr. Differential Conductance and Quantum Interference in Kondo Systems. *Phys. Rev. Lett.*, 104(18):187202, May 2010.

[71] Naoyuki Nakagawa, Harold Y Hwang, and David A Muller. Why some interfaces cannot be sharp. *Nature Materials*, 5(3):204–209, January 2006.

[72] T Caldwell, A P Reyes, W G Moulton, P L Kuhns, MJR Hoch, P Schlottmann, and Z. Fisk. High-field suppression of in-gap states in the Kondo insulator Sm B 6. *Phys. Rev. B*, 75(7):075106, 2007.

[73] Yi-feng Yang. Fano effect in the point contact spectroscopy of heavy-electron materials. *Phys. Rev. B*, 79(24):241107, 2009.

[74] P Wölfle, Y Dubi, and A V Balatsky. Tunneling into Clean Heavy Fermion Compounds: Origin of the Fano Line Shape. *Phys. Rev. Lett.*, 105(24):246401, December 2010.

[75] M Maltseva, M. Dzero, and P. Coleman. Electron Cotunneling into a Kondo Lattice. *Phys. Rev. Lett.*, 103(20):206402, November 2009.

[76] V Madhavan, W Chen, T Jamneala, M F Crommie, and N S Wingreen. Tunneling into a single magnetic atom: spectroscopic evidence of the Kondo resonance. *Science*, 280(5363):567–569, 1998.

[77] W K Park, P H Tobash, F Ronning, E D Bauer, J L Sarrao, J D Thompson, and L H Greene. Observation of the hybridization gap and Fano resonance in the Kondo lattice URu 2 Si 2. *Phys. Rev. Lett.*, 108(24):246403, 2012.

[78] S Ernst, S Kirchner, C Krellner, C Geibel, G Zwicknagl, F Steglich, and S Wirth. Emerging local Kondo screening and spatial coherence in the heavy-fermion metal YbRh2Si2. *Nature*, 474(7351):362–366, 2011.

[79] Masaichiro Mizumaki Iga, Satoshi Tsutsui, and Fumitoshi. Temperature dependence of Sm valence in SmB 6 studied by X-ray absorption spectroscopy. *J. Phys.: Conf. Ser.*, 176(1):012034, 2009.

[80] Adel Benlagra, Thomas Pruschke, and Matthias Vojta. Finite-temperature spectra and quasiparticle interference in Kondo lattices: From light electrons to coherent heavy quasiparticles. *Phys. Rev. B*, 84(19):195141, November 2011.

[81] Pegor Aynajian, Eduardo H da Silva Neto, András Gyenis, Ryan E Baumbach, J D Thompson, Zachary Fisk, Eric D Bauer, and Ali Yazdani. Visualizing heavy fermions emerging in a quantum critical Kondo lattice. *Nature*, 486(7402):201–206, June 2012.

[82] V N Antonov, B N Harmon, and A N Yaresko. Electronic structure of mixed-valence semiconductors in the LSDA+U approximation. II. SmB6 and YbB12. *Phys. Rev. B*, 66(16):165209 EP –, October 2002.

[83] A R Schmidt, M H Hamidian, P Wahl, F Meier, A V Balatsky, J D Garrett, T J Williams, G M Luke, and J. C. Seamus Davis. Imaging the Fano lattice to 'hidden order' transition in URu2Si2. *Nature*, 465(7298):570–576, June 2010.

[84] Rui Yu, Wei Zhang, Hai-Jun Zhang, Shou-Cheng Zhang, Xi Dai, and Zhong Fang. Quantized Anomalous Hall Effect in Magnetic Topological Insulators. *Science*, 329(5987):61–64, July 2010.

[85] Qin Liu, Chao-Xing Liu, Cenke Xu, Xiao-Liang Qi, and Shou-Cheng Zhang. Magnetic Impurities on the Surface of a Topological Insulator. *Phys. Rev. Lett.*, 102(15):156603 EP –, April 2009.

[86] L Andrew Wray, Su-Yang Xu, Yuqi Xia, David Hsieh, Alexei V Fedorov, Yew San Hor, Robert J Cava, Arun Bansil, Hsin Lin, and M Zahid Hasan. A topological insulator surface under strong Coulomb, magnetic and disorder perturbations. *Nat Phys*, 7(1):32–37, December 2010.

[87] Canli Song, Ye-Ping Jiang, Yi-Lin Wang, Zhi Li, Lili Wang, Ke He, Xi Chen, Xu-Cun Ma, and Qi-Kun Xue. Gating the charge state of single Fe dopants in the topological insulator Bi2Se3 with a scanning tunneling microscope. *Phys. Rev. B*, 86(4):045441 EP –, July 2012.

[88] M R Scholz, J Sánchez-Barriga, D Marchenko, A Varykhalov, A Volykhov, L V Yashina, and O Rader. Tolerance of Topological Surface States towards Magnetic Moments: Fe on Bi2Se3. *Phys. Rev. Lett.*, 108(25):256810 EP –, June 2012.

[89] J Honolka, A A Khajetoorians, V Sessi, T O Wehling, S Stepanow, J-L Mi, B B Iversen, T Schlenk, J Wiebe, N B Brookes, A I Lichtenstein, Ph Hofmann, K Kern, and Roland Wiesendanger. In-Plane Magnetic Anisotropy of Fe Atoms on Bi2Se3(111). *Phys. Rev. Lett.*, 108(25):256811 EP –, June 2012.

[90] T Schlenk, M Bianchi, M Koleini, A Eich, O Pietzsch, T O Wehling, T Frauenheim, A Balatsky, J-L Mi, B B Iversen, J Wiebe, A A Khajetoorians, Ph Hofmann, and Roland Wiesendanger. Controllable Magnetic Doping of the Surface State of a Topological Insulator. *Phys. Rev. Lett.*, 110(12):126804 EP –, March 2013.

[91] Mao Ye, Kenta Kuroda, Yukiharu Takeda, Yuji Saitoh, Kazuaki Okamoto, Si-Yuan Zhu, Kaito Shirai, Koji Miyamoto, Masashi Arita, Masashi Nakatake, Taichi Okuda, Yoshifumi Ueda, Kenya Shimada, Hirofumi Namatame, Masaki Taniguchi, and Akio Kimura. Perpendicular magnetic anisotropy with enhanced orbital moments of Fe adatoms on a topological surface of Bi2Se3. *Journal of Physics: Condensed Matter*, 25(23):232201, May 2013.

[92] Duming Zhang, Anthony Richardella, David W Rench, Su-Yang Xu, Abhinav Kandala, Thomas C Flanagan, Haim Beidenkopf, Andrew L Yeats, Bob B Buckley, Paul V Klimov, David D Awschalom, Ali Yazdani, Peter Schiffer, M Zahid Hasan, and Nitin Samarth. Interplay between ferromagnetism, surface states, and quantum corrections in a magnetically doped topological insulator. *Phys. Rev. B*, 86(20):205127 EP –, November 2012.

[93] Hao Zhu, Curt A Richter, Erhai Zhao, John E Bonevich, William A Kimes, Hyuk-Jae Jang, Hui Yuan, Haitao Li, Abbas Arab, Oleg Kirillov, James E Maslar, Dimitris E Ioannou, and Qiliang Li. Topological Insulator Bi2Se3 Nanowire High Performance Field-Effect Transistors. *Sci. Rep.*, 3, April 2013.

[94] Yi Zhang, Ke He, Cui-Zu Chang, Canli Song, Li-li Wang, Xi Chen, Jin-Feng Jia, Zhong Fang, Xi Dai, Wen-Yu Shan, Shun-Qing Shen, Qian Niu, Xiao-Liang Qi, Shou-Cheng Zhang, Xu-Cun Ma, and Qi-Kun Xue. Crossover of the three-dimensional topological insulator Bi2Se3 to the two-dimensional limit. *Nat Phys*, 6(8):584–588, June 2010.

[95] Marco Bianchi, Dandan Guan, Shining Bao, Jianli Mi, Bo Brummerstedt Iversen, Philip D C King, and Philip Hofmann. Coexistence of the topological state and a two-dimensional electron gas on the surface of Bi2Se3. *Nat Commun*, 1(8):128, November 2010.

[96] D Niesner, Th Fauster, S V Eremeev, T V Menshchikova, Yu M Koroteev, A P Protogenov, E V Chulkov, O E Tereshchenko, K A Kokh, O Alekperov, A Nadjafov, and N Mamedov. Unoccupied topological states on bismuth chalcogenides. *Phys. Rev. B*, 86(20):205403 EP –, November 2012.

[97] J A Sobota, S L Yang, A F Kemper, J J Lee, F T Schmitt, W Li, R G Moore, J G Analytis, I R Fisher, P S Kirchmann, T P Devereaux, and Zhi-Xun Shen. Direct Optical Coupling to an Unoccupied Dirac Surface State in the Topological Insulator Bi2Se3. *Phys. Rev. Lett.*, 111(13):136802 EP –, September 2013.

[98] Haim Beidenkopf, Pedram Roushan, Jungpil Seo, Lindsay Gorman, Ilya Drozdov, Yew San Hor, R J Cava, and Ali Yazdani. Spatial fluctuations of helical Dirac fermions on the surface of topological insulators. *Nat Phys*, 7(12):939–943, 2011.

[99] Chris Mann, Damien West, Ireneusz Miotkowski, Yong P Chen, Shengbai Zhang, and Chih-Kang Shih. Mapping the 3D surface potential in Bi2Se3. *Nature Communications*, 4:–, August 2013.

[100] Pedram Roushan, Jungpil Seo, Colin V Parker, Y S Hor, D Hsieh, Dong Qian, Anthony Richardella, M Zahid Hasan, R J Cava, and Ali Yazdani. Topological surface states protected from backscattering by chiral spin texture. *Nature*, 460(7259):1106–1109, August 2009.

[101] Zhanybek Alpichshev, J G Analytis, J-H Chu, Ian R. Fisher, Y L Chen, Zhi-Xun Shen, Alan Fang, and Aharon Kapitulnik. STM imaging of electronic waves on the surface of Bi 2 Te 3: topologically protected surface states and hexagonal warping effects. *Phys. Rev. Lett.*, 104(1):016401, 2010.

[102] Anjan Soumyanarayanan, Michael M Yee, Yang He, Hsin Lin, Dillon R Gardner, Arun Bansil, Young S Lee, and Jennifer E Hoffman. Imaging the Nanoscale Band Structure of Topological Sb. *arXiv*, page 1311.1758, November 2013.

[103] K Kuroda, M Arita, K Miyamoto, M Ye, J Jiang, A Kimura, E E Krasovskii, E V Chulkov, H Iwasawa, T Okuda, K Shimada, Y Ueda, H Namatame, and M Taniguchi. Hexagonally Deformed Fermi Surface of the 3D Topological Insulator Bi2Se3. *Phys. Rev. Lett.*, 105(7):076802 EP –, August 2010.

[104] Haijun Zhang, Chao-Xing Liu, Xi Dai, Zhong Fang, and Shou-Cheng Zhang. Topological insulators in Bi2Se3, Bi2Te3 and Sb2Te3 with a single Dirac cone on the surface. *Nat Phys*, 5(6):438–442, May 2009.

[105] Kazuma Eto, Zhi Ren, A A Taskin, Kouji Segawa, and Yoichi Ando. Angular-dependent oscillations of the magnetoresistance in Bi2Se3 due to the three-dimensional bulk Fermi surface. *Phys. Rev. B*, 81(19):195309 EP –, May 2010.

[106] Z. Salman, E Pomjakushina, V Pomjakushin, A Kanigel, K Chashka, K Conder, E Morenzoni, T Prokscha, K Sedlak, and A Suter. The Nature of Magnetic Ordering in Magnetically Doped Topological Insulator $Bi_{2-x}Fe_xSe_3$. *arXiv*, March 2012.

[107] P. Blaha, K. Schwarz, G. Madsen, D. Kvasnicka, and J. Luitz. In K. Schwarz, editor, *An augmented plane wave plus local orbitals program for calculating crystal properties*. Technical University of Wien, Vienna, 2001.

[108] S Urazhdin, D Bilc, S D Mahanti, S H Tessmer, Theodora Kyratsi, and M G Kanatzidis. Surface effects in layered semiconductors Bi2Se3 and Bi2Te3. *Phys. Rev. B*, 69(8):085313 EP –, February 2004.

[109] M Ye, S V Eremeev, K Kuroda, E E Krasovskii, E V Chulkov, Y Takeda, Y Saitoh, K Okamoto, S Y Zhu, K Miyamoto, M Arita, M Nakatake, T Okuda, Y Ueda, K Shimada, H Namatame, M Taniguchi, and A Kimura. Quasiparticle interference on the surface of Bi2Se3 induced by cobalt adatom in the absence of ferromagnetic ordering. *Phys. Rev. B*, 85(20):205317 EP –, May 2012.

[110] Jian-Min Zhang, Wenmei Ming, Zhigao Huang, Gui-Bin Liu, Xufeng Kou, Yabin Fan, Kang L Wang, and Yugui Yao. Stability, electronic, and magnetic properties of the magnetically doped topological insulators Bi2Se3, Bi2Te3, and Sb2Te3. *Phys. Rev. B*, 88(23):235131, December 2013.

[111] Jian-Min Zhang, Wenguang Zhu, Ying Zhang, Di Xiao, and Yugui Yao. Tailoring Magnetic Doping in the Topological Insulator Bi2Se3. *Phys. Rev. Lett.*, 109(26):266405 EP –, December 2012.

[112] L B Abdalla, L Seixas, T M Schmidt, R H Miwa, and A Fazzio. Topological insulator Bi2Se3(111) surface doped with transition metals: An *ab initio* investigation. *Phys. Rev. B*, 88(4):045312 EP –, July 2013.

[113] J Navrátil, J Horák, T Plecháček, S Kamba, P Lošt'ák, J S Dyck, W Chen, and C Uher. Conduction band splitting and transport properties of Bi2Se3. *Journal of Solid State Chemistry*, 177(4–5):1704–1712, April 2004.

[114] D West, Y Y Sun, Han Wang, Junhyeok Bang, and S B Zhang. Native defects in second-generation topological insulators: effect of spin-orbit interaction on Bi 2 Se 3. *Phys. Rev. B*, 86(12):121201, 2012.

[115] Lin-Lin Wang, Mianliang Huang, Srinivasa Thimmaiah, Aftab Alam, Sergey L Bud'ko, Adam Kaminski, Thomas A Lograsso, Paul Canfield, and Duane D Johnson. Native defects in tetradymite Bi 2 (Te x Se 3− x) topological insulators. *Phys. Rev. B*, 87(12):125303, 2013.

[116] Liang Fu. Hexagonal warping effects in the surface states of the topological insulator Bi 2 Te 3. *Phys. Rev. Lett.*, 103(26):266801, 2009.

[117] Z-H Zhu, G Levy, B. Ludbrook, C. N. Veenstra, J A Rosen, R Comin, D. Wong, P. Dosanjh, A Ubaldini, P Syers, N P Butch, J Paglione, I S Elfimov, and Andrea Damascelli. Rashba Spin-Splitting Control at the Surface of the Topological Insulator Bi2Se3. *Phys. Rev. Lett.*, 107(18):186405 EP –, October 2011.

[118] P D C King, R C Hatch, M Bianchi, R Ovsyannikov, C Lupulescu, G Landolt, B Slomski, J H Dil, D Guan, J-L Mi, E D L Rienks, J Fink, A Lindblad, S Svensson, S Bao, G Balakrishnan, B B Iversen, J Osterwalder, W Eberhardt, F Baumberger, and Ph Hofmann. Large Tunable Rashba Spin Splitting of a Two-Dimensional Electron Gas in Bi2Se3. *Phys. Rev. Lett.*, 107(9):096802 EP –, August 2011.

[119] M S Bahramy, P D C King, A de la Torre, J Chang, M Shi, L Patthey, G Balakrishnan, Ph Hofmann, R Arita, N Nagaosa, and F Baumberger. Emergent quantum confinement at topological insulator surfaces. *Nat Commun*, 3:1159, October 2012.

[120] H M Benia, A Yaresko, A P Schnyder, J Henk, C T Lin, K Kern, and C R Ast. Origin of Rashba splitting in the quantized subbands at the Bi2Se3 surface. *Phys. Rev. B*, 88(8):081103 EP –, August 2013.

[121] Marco Bianchi, Richard C Hatch, Jianli Mi, Bo Brummerstedt Iversen, and Philip Hofmann. Simultaneous quantization of bulk conduction and valence states through adsorption of nonmagnetic impurities on Bi 2 Se 3. *Phys. Rev. Lett.*, 107(8):086802, 2011.

[122] Hadj M Benia, Chengtian Lin, Klaus Kern, and Christian R Ast. Reactive Chemical Doping of the Bi2Se3 Topological Insulator. *Phys. Rev. Lett.*, 107(17):177602 EP –, October 2011.

[123] S V Eremeev, M G Vergniory, T V Menshchikova, A A Shaposhnikov, and E V Chulkov. The effect of van der Waal's gap expansions on the surface electronic structure of layered topological insulators. *New J. Phys.*, 14(11):113030, November 2012.

[124] M Ye, S V Eremeev, K Kuroda, M Nakatake, S Kim, Y Yamada, E E Krasovskii, E V Chulkov, M Arita, H Miyahara, T Maegawa, K Okamoto, K Miyamoto, T Okuda, K Shimada, H Namatame, M Taniguchi, Y Ueda, and A Kimura. Relocation of the topological surface state of Bi_2Se_3 beneath the surface by Ag intercalation. *arXiv*, December 2011.

[125] Yoshinori Okada, Chetan Dhital, Wenwen Zhou, Erik D. Huemiller, Hsin Lin, S Basak, A Bansil, Y-B Huang, H Ding, Z Wang, Stephen D. Wilson, and V Madhavan. Direct Observation of Broken Time-Reversal Symmetry on the Surface of a Magnetically Doped Topological Insulator. *Phys. Rev. Lett.*, 106(20):206805, May 2011.

[126] Wei-Cheng Lee, Congjun Wu, Daniel P Arovas, and Shou-Cheng Zhang. Quasiparticle interference on the surface of the topological insulator Bi2Te3. *Phys. Rev. B*, 80(24):245439 EP –, December 2009.

[127] C E ViolBarbosa, Chandra Shekhar, Binghai Yan, S Ouardi, G H Fecher, and C Felser. Direct observation of band bending in topological insulator Bi2Se3. *arXiv*, July 2013.

[128] Eduardo Fradkin and Steven A Kivelson. High-temperature superconductivity: Ineluctable complexity. *Nat Phys*, 8(12):864–866, November 2012.

[129] J M Tranquada, B J Sternlieb, J D Axe, Y Nakamura, and S Uchida. Evidence for stripe correlations of spins and holes in copper oxide superconductors. *Nature*, 375(6532):561–563, June 1995.

[130] P. Abbamonte, A. Rusydi, S. Smadici, G D Gu, G A Sawatzky, and D L Feng. Spatially modulated 'Mottness' in La2-xBaxCuO4. *Nat Phys*, 1(3):155–158, December 2005.

[131] G Ghiringhelli, M Le Tacon, M Minola, S Blanco-Canosa, C Mazzoli, N B Brookes, G M De Luca, A Frano, D G Hawthorn, F He, T Loew, M M Sala, D C Peets, M Salluzzo, E Schierle, R Sutarto, G A Sawatzky, E Weschke, B Keimer, and L Braicovich. Long-Range Incommensurate Charge Fluctuations in (Y,Nd)Ba2Cu3O6+x. *Science*, 337(6096):821–825, August 2012.

[132] J Chang, E Blackburn, A T Holmes, N B Christensen, J Larsen, J Mesot, Ruixing Liang, D A Bonn, W N Hardy, A Watenphul, M v Zimmermann, E M Forgan, and S M Hayden. Direct observation of competition between superconductivity and charge density wave order in YBa2Cu3O6.67. *Nat Phys*, 8(12):871–876, October 2012.

[133] Jennifer E Hoffman, Eric W Hudson, K M Lang, V Madhavan, H Eisaki, S Uchida, and J. C. Seamus Davis. A four unit cell periodic pattern of quasi-particte states surrounding vortex cores in Bi2Sr2CaCu2O8+delta. *Science*, 295(5554):466–469, January 2002.

[134] T Hanaguri, C Lupien, Y Kohsaka, D-H Lee, M Azuma, M Takano, H Takagi, and J. C. Seamus Davis. A 'checkerboard' electronic crystal state in lightly hole-doped Ca2-xNaxCuO2Cl2. *Nature*, 430(7003):1001–1005, August 2004.

[135] C Howald, H Eisaki, N Kaneko, and Aharon Kapitulnik. Coexistence of periodic modulation of quasiparticle states and superconductivity in Bi2Sr2CaCu2O8+ . *Proceedings of the National Academy of Sciences*, 100(17):9705–9709, May 2011.

[136] Michael Vershinin, Shashank Misra, S Ono, Y Abe, Yoichi Ando, and Ali Yazdani. Local Ordering in the Pseudogap State of the High-Tc Superconductor Bi2Sr2CaCu2O8+δ. *Science*, 303(5666):1995–1998, March 2004.

[137] W D Wise, M C Boyer, Kamalesh Chatterjee, Takeshi Kondo, T Takeuchi, H Ikuta, Yayu Wang, and Eric W Hudson. Charge-density-wave origin of cuprate checkerboard visualized by scanning tunnelling microscopy. *Nat Phys*, 4(9):696–699, July 2008.

[138] Colin V Parker, Pegor Aynajian, Eduardo H da Silva Neto, Aakash Pushp, Shimpei Ono, Jinsheng Wen, Zhijun Xu, Genda Gu, and Ali Yazdani. Fluctuating stripes at the onset of the pseudogap in the high-Tc superconductor Bi2Sr2CaCu2O8+x. *Nature*, 468(7):677–680, December 2010.

[139] A Maeda, M Hase, I Tsukada, K Noda, S Takebayashi, and K Uchinokura. Physical properties of Bi2Sr2Can-1CunOy (n=1,2,3). *Phys. Rev. B*, 41(10):6418–6434, April 1990.

[140] Yoichi Ando and T Murayama. Nonuniversal power law of the Hall scattering rate in a single-layer cuprate Bi2Sr2-xLaxCuO6. *Phys. Rev. B*, 60(10):R6991–R6994, September 1999.

[141] M C Boyer, W D Wise, Kamalesh Chatterjee, Ming Yi, Takeshi Kondo, T Takeuchi, H Ikuta, and Eric W Hudson. Imaging the two gaps of the high-temperature superconductor Bi2Sr2CuO6+x. *Nat Phys*, 3(11):802–806, September 2007.

[142] W D Wise, Kamalesh Chatterjee, M C Boyer, Takeshi Kondo, T Takeuchi, H Ikuta, Zhijun Xu, Jinsheng Wen, G D Gu, Yayu Wang, and Eric W Hudson. Imaging nanoscale Fermi-surface variations in an inhomogeneous superconductor. *Nat Phys*, 5(3):213–216, January 2009.

[143] Takeshi Kondo, Tsunehiro Takeuchi, Uichiro Mizutani, Takayoshi Yokoya, Syunsuke Tsuda, and Shik Shin. Contribution of electronic structure to thermoelectric power in (Bi,Pb)2(Sr,La)2CuO6+δ. *Phys. Rev. B*, 72(2):024533 EP –, July 2005.

[144] J A Slezak, Jinho Lee, M Wang, K McElroy, K Fujita, B. M. Andersen, P Hirschfeld, H Eisaki, S Uchida, and J. C. Seamus Davis. Imaging the impact on cuprate superconductivity of varying the interatomic distances within individual crystal unit cells. *P Natl Acad Sci Usa*, 105(9):3203–3208, 2008.

[145] K KUDO, Y MIYOSHI, T SASAKI, and N KOBAYASHI. Hole-doping and magnetic-field effects on the pseudogap in Bi1.74Pb0.38Sr1.88CuO6+δ studied by the out-of-plane resistivity. *Physica C: Superconductivity*, 426–431, Part 1(0):251–256, October 2005.

[146] Yoichi Ando, Y Hanaki, S Ono, T Murayama, Kouji Segawa, N Miyamoto, and Seiki Komiya. Carrier concentrations in Bi2Sr2-zLazCuO6+δ single crystals and their relation to the Hall coefficient and thermopower. *Phys. Rev. B*, 61(22):R14956–R14959, June 2000.

[147] J H Ma, Z H Pan, F C Niestemski, M Neupane, Y M Xu, P Richard, K Nakayama, T Sato, T Takahashi, H Q Luo, L Fang, H-H Wen, Ziqiang Wang, H Ding, and V Madhavan. Coexistence of Competing Orders with Two Energy Gaps in Real and Momentum Space in the High Temperature Superconductor Bi2Sr2-xLaxCuO6+δ. *Phys. Rev. Lett.*, 101(20):207002 EP –, November 2008.

[148] L Shan, A Ejov, A Volodin, V V Moshchalkov, H-H Wen, and C T Lin. STM studies of the surface structure in cleaved Bi 2Sr 2CuO 6 + δsingle crystals. *Europhys Lett*, 61(5):681–687, January 2007.

[149] J A Rosen, R Comin, G Levy, D Fournier, Z-H Zhu, B. Ludbrook, C. N. Veenstra, A Nicolaou, D. Wong, P. Dosanjh, Y Yoshida, H Eisaki, G R Blake, F White, T T M Palstra, R Sutarto, F He, A Frano Pereira, Y Lu, B Keimer, G Sawatzky, L. Petaccia, and Andrea Damascelli. Surface-enhanced charge-density-wave instability in underdoped Bi2Sr2-xLaxCuO6+delta. *Nature Communications*, 4, July 2013.

[150] M J Lawler, K Fujita, Jhinhwan Lee, A R Schmidt, Y Kohsaka, Chung Koo Kim, H Eisaki, S Uchida, J. C. Seamus Davis, J P Sethna, and Eun-Ah Kim. Intra-unit-cell electronic nematicity of the high-Tc copper-oxide pseudogap states. *Nature*, 466(7304):347–351, May 2010.

[151] Ilija Zeljkovic, Elizabeth J Main, Tess L Williams, M C Boyer, Kamalesh Chatterjee, W D Wise, Yin Yii, Martin Zech, Adam Pivonka, Takeshi Kondo, T Takeuchi, Hiroshi Ikuta, Jinsheng Wen, Zhijun Xu, G D Gu, Eric W Hudson, and Jennifer E Hoffman. Scanning tunnelling microscopy imaging of symmetry-breaking structural distortion in the bismuth-based cuprate superconductors. *Nature Materials*, 11(7):585–589, May 2012.

[152] Tadashi Machida, Yusuke Kamijo, Keiji Harada, Tetsurou Noguchi, Ryo Saito, Takuya Kato, and Hideaki Sakata. Appearance of New Energy Gap and Periodic Local Density-of-States Modulation in Bi 2Sr 1.6La 0.4CuO 6+δ. *Journal of the Physical Society of Japan*, 75(8):083708, August 2006.

[153] Ilija Zeljkovic, Zhijun Xu, Jinsheng Wen, Genda Gu, Robert S. Markiewicz, and Jennifer E Hoffman. Imaging the Impact of Single Oxygen Atoms on Superconducting Bi2+ySr2–yCaCu2O8+x. *Science*, 337(6092):320–323, January 2012.

[154] G Kinoda, H Mashima, K Shimizu, J Shimoyama, K Kishio, and T Hasegawa. Direct determination of localized impurity levels located in the blocking layers of Bi2Sr2CaCu2Oy using scanning tunneling microscopy/spectroscopy. *Phys. Rev. B*, 71(2):020502, January 2005.

[155] C O Rodriguez, Ruben Weht, Mariana Weissmann, N E Christensen, and M S Methfessel. Surface effects on the electronic structure of Bi2201. *Physica C: Superconductivity*, 258(3–4):360–364, November 1995.

[156] S Hüfner, M A Hossain, Andrea Damascelli, and G A Sawatzky. Two gaps make a high-temperature superconductor? *Reports on Progress in Physics*, 71(6):062501, May 2008.

[157] Jennifer E Hoffman, K McElroy, DH Lee, KM Lang, H Eisaki, S Uchida, and J. C. Seamus Davis. Imaging quasiparticle interference in Bi2Sr2CaCu2O8+delta. *Science*, 297(5584):1148–1151, 2002.

[158] E H da Silva Neto, P Aynajian, A Frano, R Comin, E Schierle, E Weschke, A Gyenis, J Wen, J Schneeloch, Z Xu, S Ono, G Gu, M Le Tacon, and Ali Yazdani. Ubiquitous Interplay Between Charge Ordering and High-Temperature Superconductivity in Cuprates. *Science*, 343(6169):393–396, January 2014.

[159] M Ido, T Yoneyama, Y H Liu, Y Takano, N Momono, and M Oda. STM/STS study on nondispersive checkerboard superstructure in superconducting Bi2212 and La-Bi2201. *Journal of Physics and Chemistry of Solids*, 69(12):3006–3010, December 2008.

[160] T Kato, T Machida, Y Kamijo, R Miyashita, and H Sakata. Spatial correlation between the LDOS modulation and electronic inhomogeneity in Bi 2Sr 2-xLa xCuO 6+δ. *J. Phys.: Conf. Ser.*, 150(5):052101, March 2009.

[161] Kyle M Shen, F Ronning, D H Lu, F Baumberger, N J C Ingle, W S Lee, W Meevasana, Y Kohsaka, M Azuma, M Takano, H Takagi, and Zhi-Xun Shen. Nodal Quasiparticles and Antinodal Charge Ordering in Ca2-xNaxCuO2Cl2. *Science*, 307(5711):901–904, February 2005.

[162] Øystein Fischer, Martin Kugler, Ivan Maggio-Aprile, Christophe Berthod, and Christoph Renner. Scanning tunneling spectroscopy of high-temperature superconductors. *Reviews of Modern Physics*, 79(1):353–419, March 2007.

[163] Andrea Damascelli, Zahid Hussain, and Zhi-Xun Shen. Angle-resolved photoemission studies of the cuprate superconductors. *Reviews of Modern Physics*, 75(2):473–541, April 2003.

[164] K McElroy, D-H Lee, Jennifer E Hoffman, K M Lang, J Lee, Eric W Hudson, H Eisaki, S Uchida, and J. C. Seamus Davis. Coincidence of Checkerboard Charge Order and Antinodal State Decoherence in Strongly Underdoped Superconducting Bi2Sr2CaCu2O8+δ. *Phys. Rev. Lett.*, 94(19):197005 EP –, May 2005.

[165] Shinji Kawasaki, Chengtian Lin, Philip L. Kuhns, Arneil P. Reyes, and Guo-qing Zheng. Carrier-Concentration Dependence of the Pseudogap Ground State of Superconducting Bi(2)Sr2-xLaxCuO6+delta Revealed by Cu-63,Cu-65-Nuclear Magnetic Resonance in Very High Magnetic Fields. *Phys. Rev. Lett.*, 105(13):–, 2010.

[166] Steven A Kivelson, E Fradkin, and V J Emery. Electronic liquid-crystal phases of a doped Mott insulator. *Nature*, 393(6685):550–553, June 1998.

[167] Steven A Kivelson, I P Bindloss, V Oganesyan, J M Tranquada, Aharon Kapitulnik, and C Howald. How to detect fluctuating stripes in the high-temperature superconductors. *Reviews of Modern Physics*, 75(4):1201–1241, October 2003.

[168] A Mesaros, K Fujita, H Eisaki, S Uchida, J. C. Seamus Davis, S Sachdev, J Zaanen, M J Lawler, and Eun-Ah Kim. Topological Defects Coupling Smectic Modulations to Intra–Unit-Cell Nematicity in Cuprates. *Science*, 333(6041):426–430, January 2011.

[169] A. Kaminski, S Rosenkranz, H M Fretwell, J C Campuzano, Z Li, H Raffy, W G Cullen, H You, C G Olson, C M Varma, and H Höchst. Spontaneous breaking of time-reversal symmetry in the pseudogap state of a high-Tc superconductor. *Nature*, 416(6881):610–613, April 2002.

[170] B Fauqué, Y Sidis, V Hinkov, S Pailhès, C T Lin, X Chaud, and P Bourges. Magnetic Order in the Pseudogap Phase of High-TC Superconductors. *Phys. Rev. Lett.*, 96(19):197001 EP –, May 2006.

[171] Y Li, V Balédent, N Barišić, Y Cho, B Fauqué, Y Sidis, G Yu, X Zhao, P Bourges, and M Greven. Unusual magnetic order in the pseudogap region of the superconductor HgBa2CuO4+δ. *Nature*, 455(7211):372–375, September 2008.

[172] Eduardo H da Silva Neto, Pegor Aynajian, Ryan E Baumbach, Eric D Bauer, John Mydosh, Shimpei Ono, and Ali Yazdani. Detection of electronic nematicity using scanning tunneling microscopy. *Phys. Rev. B*, 87(16):161117 EP –, April 2013.

[173] M H Hamidian, I A Firmo, K Fujita, S Mukhopadhyay, J W Orenstein, H Eisaki, S Uchida, M J Lawler, Eun-Ah Kim, and J. C. Seamus Davis. Picometer registration of zinc impurity states in Bi 2Sr 2CaCu 2O 8+ $\delta$for phase determination in intra-unit-cell Fourier transform STM. *New J. Phys.*, 14(5):053017, May 2012.

[174] J Lee, K Fujita, A R Schmidt, C K Kim, H Eisaki, S Uchida, and J. C. Seamus Davis. Spectroscopic Fingerprint of Phase-Incoherent Superconductivity in the Underdoped Bi2Sr2CaCu2O8+ . *Science*, 325(5944):1099–1103, August 2009.

Page intentionally left blank